

ABSTRACT

Title of dissertation: Disordered Ultracold Two-Dimensional
 Bose Gases

 Matthew Charles Beeler
 Doctor of Philosophy, 2011

Dissertation directed by: Dr. Steven Rolston
 Department of Physics

Ultracold bose gas systems can perform quantum simulations of high temperature superconductors in certain parameter regimes. Specifically, 2D bose gases at low temperatures exhibit a superfluid to thermal gas phase transition analogous to the superconductor to insulator transition in certain superconductors. The unbinding of thermally activated vortex pairs drives this phase transition, and disorder is expected to affect vortex motion in this system. In addition, disorder itself can drive phase transitions in superconductors.

We have designed and built a system which produces two 2D ultracold Bose gas systems separated by a few microns. In addition, we have also produced a disordered speckled laser intensity pattern with a grain size of $\sim 1 \mu\text{m}$, small enough to provide a disordered potential for the two systems. We have observed the superfluid phase transition with and without the presence of disorder. The coherence of the system, which is related to superfluidity, is strongly reduced by the presence of disorder, even at small disorder strength, but the effect of the disorder on observed vortices in the system is less clear.

Disordered Ultracold Two-Dimensional Bose Gases

by

Matthew Charles Beeler

Dissertation submitted to the Faculty of the Graduate School of the
University of Maryland, College Park in partial fulfillment
of the requirements for the degree of
Doctor of Philosophy
2011

Advisory Committee:

Dr. Steven Rolston, Chair/Advisor

Dr. Mario Dagenais, Dean's Representative

Dr. Luis Orozco

Dr. James Porto

Dr. Eite Tiesinga

© Copyright by
Matthew Charles Beeler
2011

Dedication

To M.H.D.

Je t'aime

Acknowledgments

This thesis has in no way been a solitary endeavor, and I have a long list of people to thank for making this possible. First, I have to thank my advisor, Dr. Steve Rolston, who let us take a newly renovated empty lab and fill it with expensive and complicated toys to play with, and helped guide us in their intended use. Emily Edwards was my partner on this project for almost my entire time in graduate school, and she played a large role in the direction and construction of the apparatus, including the implementation of the incommensurate lattices which led to our first paper. Kevin Teo and Brendan Wyker helped in the initial construction of the apparatus, back when we were still doing plumbing, ordering shelving, and locking lasers. We have since had two postdocs, Zhaoyuan Ma and Tao Hong, whom have left their mark on the experiment. Ilya Arakelyan and Jenn Johnson have been sharing the apparatus with us while pursuing different science, and I must thank them for their help as well as their willingness to let me use the apparatus far more often than was fair. Matt Reed will be taking over the apparatus after I leave, and it has been fun working with him for the last year or so.

I have also benefited from conversations with the large number of students who have worked for the Rolston group over the years. Scott Fletcher, Xianli Zhang, and now Kevin Twedt have worked on the ultracold plasma experiment across the hall, and have been invaluable sources of technical advice and equipment. Tommy Willis was always interested in what I was doing, and was extremely useful as someone who could provide an educated but outside opinion. Alessandro Zenesini spent

two summers in our lab, shaking his head at our messiness and providing valuable insights.

Dr. Luis Orozco and his students have also been here since the beginning, and they have been assets to my growth as a graduate student. Michael Scholten, David Norris, and Jon Sterk have been willingly listening to me ramble about optical lattices and superconductors for the last few years now, even though it is far afield from their specialty, and I even managed to coerce Michael into machining a few parts for me. The formation of the JQI expanded the number of knowledgeable people around, and the opening of Dr. Chris Monroe's labs down the hall brought an influx of new ideas and equipment. Dr. Trey Porto and Dr. Ian Spielman were extremely helpful when they started spending time at UMD.

My undergraduate advisor at Miami University, Dr. Samir Bali, pushed me onto this path and inspired me to continue doing research on ultracold atoms in graduate school.

On a personal level, I couldn't have done this without my wife, Stephanie, who somehow managed to support me through all of the ups and downs and crazy work hours that grad school entails. Her belief that I could do anything never wavered, and I can't thank her enough for that. I also have to thank my parents for instilling in me a strong belief in the value of education and following your dreams, although I don't know if they thought I would take it this far.

Finally, I would like to thank all of the people that have helped me in one way or another that I have forgotten to mention here. It's been a long journey.

Table of Contents

List of Tables	vii
List of Figures	viii
1 Background	1
1.1 Introduction	1
1.2 Motivation: 2D Ultracold Bose Gases with Disorder	2
1.3 2D Ultracold Gases	12
1.3.1 Non-Interacting Systems	15
1.3.2 Interactions in a Uniform System	16
1.3.3 Interactions in a Harmonic Trap	19
1.3.4 2D Ultracold Bose Gas Experiments	22
1.4 Disordered Ultracold Gases	23
1.5 Disordered 2D Experiments	24
2 Experimental Sequence	26
2.1 Overview	26
2.2 Thermal Source and Zeeman Slower	27
2.3 MOT	32
2.4 Magnetic Trap	33
2.5 RF Evaporation	38
2.6 Optical Trap	40
3 Technical Details of BEC Production	43
3.1 Overview	43
3.2 Vacuum	43
3.2.1 Main Chamber	43
3.2.2 Rubidium Oven	49
3.3 Lasers	53
3.3.1 Frequency Stabilization	54
3.3.2 Intensity Stabilization	57
3.4 Zeeman Slower and MOT	60
3.5 Optical Molasses/Optical Pumping	62
3.6 Magnetic Trap	63
3.7 Power Supplies and Grounding	67
3.8 Optical Trap	69
3.9 Data Collection (Imaging)	78
3.10 Control and Analysis	84
3.10.1 Hardware	84
3.10.2 Software	87

4	Advanced Experimental Setup	98
4.1	Incommensurate Lattices	98
4.2	Speckle Disorder	101
4.3	2D System Creation	109
5	Experimental Methods and Results	117
5.1	2D Systems and Observation of BKT Transition	117
5.1.1	Analysis of Interference Patterns	127
5.1.2	BKT Transition in 2.65 μm Lattice	134
5.2	2D Systems with Disorder	137
5.3	Conclusions	143
A	Digital and Analog Outputs	145
B	1D Gross-Pitaevskii Equation Solution	148
C	1D Gross-Pitaevskii Equation Solver in MATLAB	153
	Bibliography	159

List of Tables

5.1	2D System Parameters	135
A.1	Digital Outputs	145
A.2	Analog Outputs	146

List of Figures

1.1	2D Superconductor Phase Diagram	5
1.2	Experimental Data Showing Superconductor to Insulator Transition	9
1.3	Experimental Evidence for Bose Metal	10
1.4	BKT/BEC Transitions in Trapped and/or Interacting Systems	14
2.1	Rb ⁸⁷ Level Structure	30
2.2	⁸⁷ Rb Zeeman Splitting	31
2.3	MOT Magnetic Field, Polarizations	34
2.4	Schematic of a Mirror MOT	35
2.5	Quadrupole Field Example	38
3.1	Picture of Main Vacuum Chamber	44
3.2	In-Vacuum Structure	45
3.3	Spherical Octagon with Coils and Beams	47
3.4	Picture of Science Chamber	48
3.5	Rb Oven Schematic	50
3.6	Rb Oven Interior Picture	52
3.7	Pound-Drever Locking Electronics	56
3.8	Zeeman Slower Magnetic Field Profile	60
3.9	Wire Traps Picture	61
3.10	Plot of Magnetic Trap Frequencies vs. Pinch Coil Current	65
3.11	Optical Trap Beam Path	69
3.12	Computer Control Schematic	84
3.13	Software Control Overview	88
3.14	Sample Labview Software Interface	89
4.1	Titanium Sapphire Laser Beam Path	99
4.2	Shallow Angle Lattice	100
4.3	Speckle Disorder Setup	102
4.4	Radial Speckle Pattern	104
4.5	Axial Speckle Pattern	104
4.6	2D Autocorrelation Function	106
4.7	Radial Autocorrelation Length Along Axis	107
4.8	Effect of Disorder Potential on 3D BEC	110
4.9	Science Cell with Beams	112
4.10	Curve for Lattice Depth Calibration	116
5.1	Interference Patterns from 5.6 μm Lattice	119
5.2	Fringe Visibility vs. Trap Depth in Wide Lattice	120
5.3	Optical Potential with and without Lattice	122
5.4	In-Situ Images in 5.6 μm Lattice	123
5.5	Examples of Odd Interference Patterns	125
5.6	Castin-Dum Expansion of 2 Planes	126

5.7	Interference Patterns with Smaller Lattice Spacing	128
5.8	Interference Pattern with Fourier Transforms	130
5.9	Visibility vs Temperature in 2.65 μm Lattice	136
5.10	Typical Absorption Images of 2D Systems with Disorder	138
5.11	Number Distribution and Temperature vs. Speckle Depth	139
5.12	Visibility vs. Disorder Strength	140
5.13	Absorption Images with Visibility and Phase Plots	142

Chapter 1

Background

1.1 Introduction

The study of ultracold gases has proven to be a very versatile field. The ability to engineer simple designer Hamiltonians has driven innovation in the types of science that can be done in these systems. Within the last few years, the capability to control and investigate the role of strong interactions between particles in these systems has increased their usefulness in understanding science that cannot be analyzed in other systems [25]. The basic building blocks of these systems are not difficult to understand, but an amazing number of Hamiltonians can be built from these few components. Variable parameters in ultracold systems include dimensionality, temperature, atom number, density, quantum states, and strength of interactions. Great physical intuition about the behavior of these systems can be found in the simple Schroedinger equation, and the rudimentary level of complication added by mean field theory for weak interactions goes even farther in aiding understanding. Still, once strong interactions are added to the system, it becomes more difficult to model these systems, and experiments are necessary to determine the physics governing the behavior of the particles.

In fact, because of their versatility and simplicity, ultracold atom systems are ideal candidates to do quantum simulation. Quantum simulation allows us to under-

stand complicated quantum mechanical systems. Richard Feynman recognized that simple quantum systems can often reveal key properties of more complex material systems [60]. Frequently, even the behavior of these simple systems is still theoretically intractable, so the outcome of experiments on analog systems, i.e. quantum simulators, can provide otherwise unavailable insights. Some important quantum systems, such as high- T_c superconductors, are not easily amenable to direct calculation, and may have many important parameters that are not separately adjustable in experiment. Strong interactions between a large number of particles make these systems complex, and their description using Bose condensation of Cooper pairs makes these systems quantum. Ultracold atom systems, through quantum simulation, may be able to shed light on the behavior of complicated solid systems.

The layout of this chapter is to first provide some motivation for studying 2D ultracold Bose gases with disorder, and show that they can be used as quantum simulators. Then, the work that has already been done in 2D systems will be reviewed in Sec. 1.3. Disorder in ultracold gases will be briefly summarized in Sec. 1.4, followed by the small amount of work done with disorder in 2D bosons in Sec. 1.5.

1.2 Motivation: 2D Ultracold Bose Gases with Disorder

When designing an experiment on ultracold atoms, it is necessary to restrict the available number of parameters to focus on a specific type of science. We are focusing on the physics of disorder. Disorder is ubiquitous in nature, and we wish

to examine its effects in ultracold atom systems. Specifically, this thesis examines the role of disorder in 2D systems.

There are a few reasons for studying 2D systems. Keeping with the theme of quantum simulation, many of the high temperature (high-Tc) superconductors are governed by two-dimensional Bosonic physics [24]. Although it seems odd to model a solid's electronic properties with a gas of neutral atoms, it turns out that many of the models governing type-II superconductivity have a great deal of similarities to a 2D gas of bosons. First, superconductivity is mediated by Cooper pairs - pairs of electrons bound together acting as composite bosons. Superconductivity comes about when these Cooper pairs become phase coherent, and in 2D the pairing temperature and superconducting transition temperature can differ significantly, which is different than in 3D [119]. Bosonic models are applicable in any temperature range when pairing has occurred, and thus the transition to phase coherence can be analogous in ultracold gases. In addition, most of the high-Tc superconductors are stacks of 2D planes weakly coupled together, meaning that much of the physics is 2D. Finally, although electrons interact via the Coulomb interaction, most models of high-Tc superconductivity replicate the fundamental behavior of these materials without including these long-range interaction effects [6].

It is worth noting that there are models of high-Tc superconductivity which do not make these assumptions, and there is no current agreement about which model is correct. The systems are too complicated to calculate exactly, and clean measurements on solids that reveal microscopic physics are difficult to make. Ultracold gas systems can be used to measure cleaner indicators of the microscopic

mechanisms predicted by bosonic models of superconductivity. However, bosonic systems cannot address the many open questions about the pairing mechanisms in superconductors. Our system only simulates the correct physics after the electrons are bound into Cooper pairs. Thus, we can only use a system of 2D bosons to replicate and perhaps constrain bosonic models of high-Tc superconductors.

Predictions about the physics of 2D superconductors with disorder are given by the “dirty boson” model [62, 149]. This model is summarized by the phase diagram given in Fig. 1.1. As a function of temperature, we see that we have the two transitions mentioned earlier. At T_{c0} , we have the bulk 3D pairing temperature, below which the Bosonic description becomes correct. T_c , meanwhile, is the superconducting transition, where the pairs develop partial long-range phase coherence. A good starting point on pairing in superconductors is Ref. [131], and our system cannot simulate this type of physics. Therefore, we will examine the microscopic physics of bosonic 2D systems, which our system can simulate.

2D systems exhibit “marginal” behavior. Peierls argued in 1935 that in an infinite uniform 2D system, there can be no long-range order [115], and it has since been rigorously shown [83, 108, 107]. In a 2D fluid, thermal fluctuations at any non-zero temperature will destroy true Bose-Einstein condensation (BEC) [26, 56, 57, 1], when the multiparticle state of the system has all of the particles in the same single-particle ground energy state. BEC is also indicated by the first order Bosonic correlation function being constant in the limit of infinite distance. In an interacting fluid system, at low enough temperature, a superfluid (flow without friction) can still exist without true BEC. In this case, we can define a local superfluid order

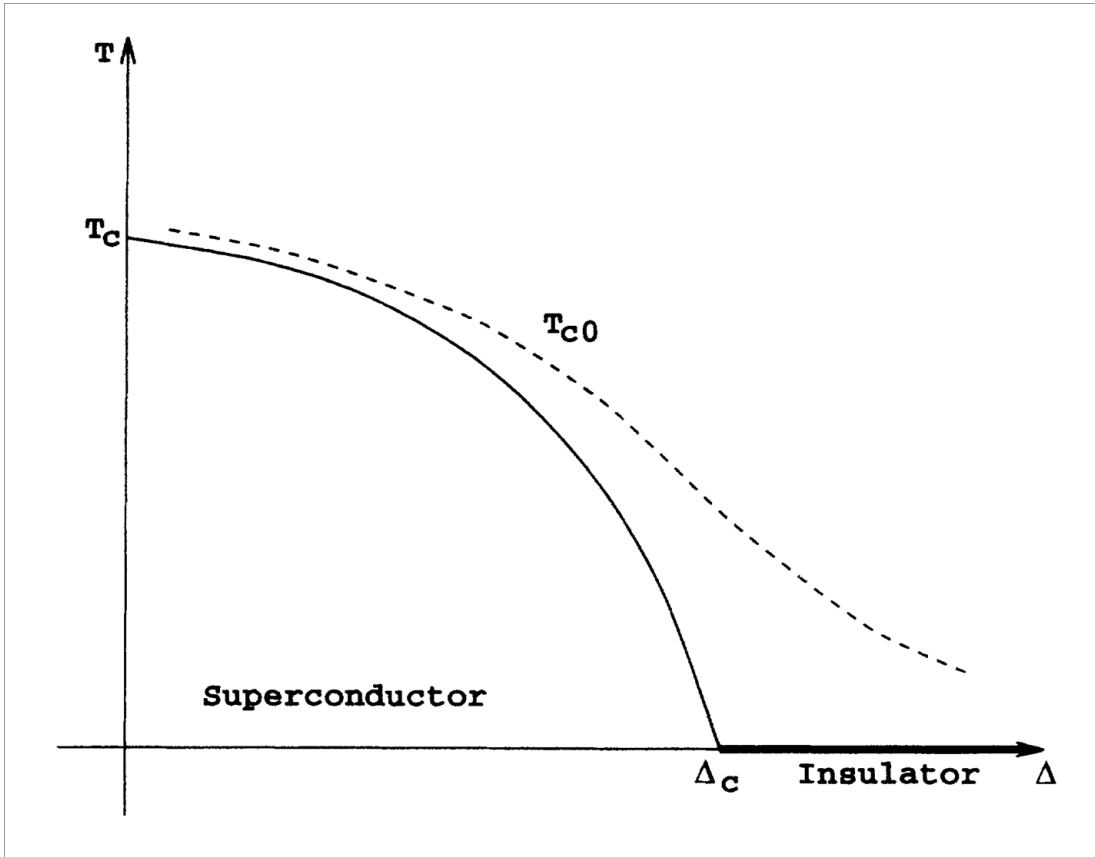


Figure 1.1: Generic phase diagram of a 2D superconductor with disorder strength Δ as a function of temperature T . Δ_c is the critical disorder strength, T_c is the critical temperature for the superconducting transition, and T_{c0} is the pairing temperature for Cooper pairs. Figure from [149].

parameter, and the transport properties of the system exhibit superfluidity, but without all of the particles being in the ground state. In this 2D superfluid, the first order Bosonic correlation function always falls off algebraically, preventing true BEC. This is in contrast to 3D, where BEC and superfluidity happen at the same time. The superfluid transition is often identified with the superconducting phase transition - the Cooper pairs become superfluid.

The mechanism for the transition between this superfluid and a normal fluid is elucidated by the theory of Berezinskii, Kosterlitz, and Thouless (BKT) [95, 94, 16, 17]. This theory says that just above zero temperature, the thermal excitations in the superfluid take two forms - long-wavelength phase fluctuations called phonons and also pairs of bound vortices. A vortex is a spot of zero density in the superfluid with locally circular flow around this spot, and a bound pair of these is two vortices with opposite directions of circulation very close together. Since the derivative of the phase of the superfluid order parameter is the velocity of the fluid, vortices can be thought of as phase defects. If the vortices are closely bound together, they do little to disturb the overall long-range phase coherence of the fluid, since their effects cancel away from the pair. The long-range phase coherence falls off slowly only through phonons. However, as the temperature is raised, the binding of the vortex pairs starts to loosen, and the vortices start to move in the fluid. When the pairs start to unbind and move about the fluid, the phase coherence of the fluid is destroyed, and the superfluid transitions to a normal fluid, or the superconductor becomes an insulator.

BKT theory has been remarkably successful in describing and predicting the

physics of 2D superfluids. It is applicable to many other types of systems as well, including Coulomb gases [110], exciton systems [139, 31], polariton systems [91, 4], and spin-polarized hydrogen [133]. Torsional oscillator experiments in thin films of superfluid ^4He showed excellent agreement with the predicted critical temperature [20, 21]. However, in a finite system, especially an inhomogeneous system, the transitions between the different phases become more difficult to discern. In fact, true BEC becomes possible in 2D in a finite system (Sec. 1.3). Identifying both the macroscopic and microscopic indicators of transitions between the various phases is still of experimental interest [75], especially in ultracold gases.

Now we can look at the effects of disorder in the phase diagram in Fig. 1.1. At low disorder strengths, both transition temperatures are lowered, until at a critical disorder strength Δ_c , the transition temperature for coherence is lowered to zero. Above this critical disorder strength there is no superconducting state, as a quantum phase transition occurs between the superconducting state and an insulating state. This phase transition has received a great deal of attention. There are experimental [98, 80] and theoretical works [34, 68, 62] indicating that the transition happens straight from the superconductor to insulator phase. Some theoretical work has indicated that there is a finite universal conductivity right at the separatrix between the two phases [149, 63, 33, 140]. Stemming from some experiments [88], many theorists now put forth that there should be an intervening metallic phase [48], which could be a phase glass [47, 155, 43]. Two good reviews of this 2D phase transition are given in Refs. [69, 119].

I will briefly summarize some of the controversy from the above papers. Exper-

imentally, one measures the resistance of a sample as a function of temperature for different values of disorder strength, which is often tuned by changing the thickness of the superconducting layer in the sample. Thinner layers allow more disorder to enter the layer from the substrate. In the case where there is no intervening metallic phase, there is a separatrix between the resistivity - it asymptotically approaches either 0 or ∞ as the disorder is tuned through the critical point (Fig. 1.2). However, in some materials, there is a range of disorder strengths over which the resistance seems to level as the temperature is lowered, as in Fig. 1.3. This would indicate a metallic phase, since it is neither insulating nor superconducting.

The idea of a metallic phase for Bosonic Cooper pairs is problematic in 2D. In low dimensions, not even non-interacting electrons can remain metallic at zero temperature in the presence of disorder [119]. So, a metallic phase must have an exotic explanation, such as a phase or vortex glass [155], which could have a finite resistivity. Perhaps the pairing amplitude of the Cooper pairs begins to fluctuate, or long range Coulomb interactions become important in this metallic state. There is no current agreement about the cause or physical mechanism of this metallic state.

There are a few reasons why an investigation into this system using cold gases might serve to answer some of the outstanding questions in 2D superconductors. First, cold atom systems have better control and reproducibility of disorder strength and size. As shown in Sec. 4.2, we can carefully control and calibrate our disorder. Second, there is no “pairing amplitude” to worry about. If there is a quantum phase transition in our system, it is a Bosonic one. Also, our particles interact only through low-energy s-wave scattering, so we can rule out the long-range effects of

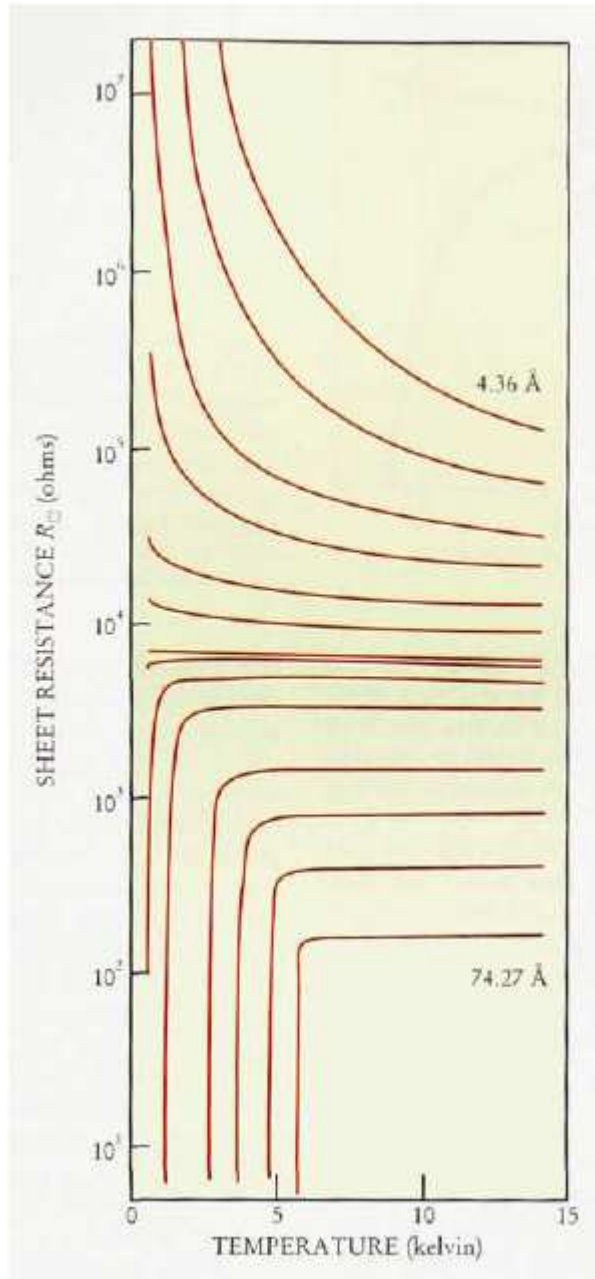


Figure 1.2: Temperature dependence of sheet resistance of Bismuth film as a function of temperature and disorder. More disordered films are thinner. Except for a nearly infinitesimal region, the films are either superconducting or insulating as T approaches 0. Figure from [69].

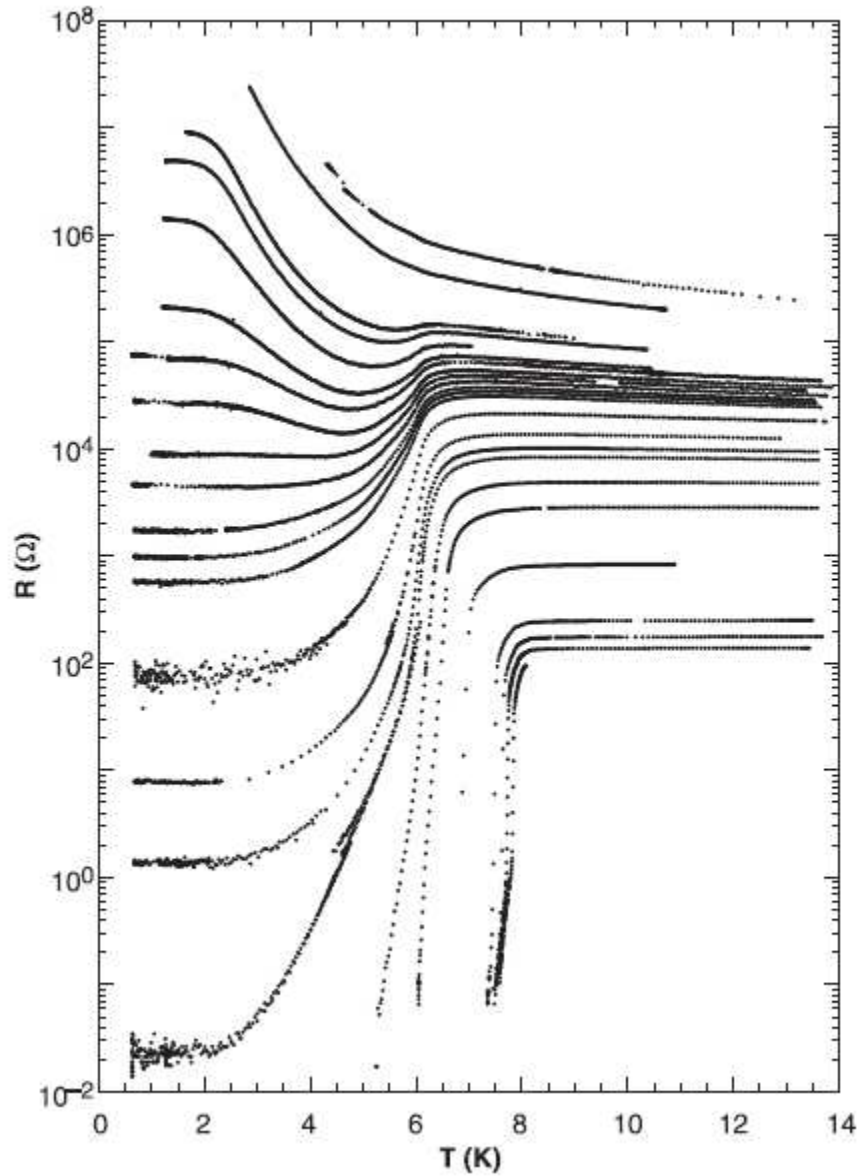


Figure 1.3: Temperature dependence of sheet resistance of Ga films as a function of temperature and disorder. Film thicknesses range from 12.75 to 16.67 Angstroms and increase from top to bottom. More disordered films are thinner. The films exhibit a wide range of disorder strength over which the resistance plateaus as T approaches 0, indicating a metallic phase. Figure from [119].

the Coulomb interaction causing any observed transition. Finally, the measurements which can be made in cold atom systems can directly access the phase of the order parameter, a very difficult feat in superconductors. Our cold atom system spans a smaller, more controllable set of the parameter space than that available to true solid systems, and can thus eliminate or constrain some of these theories.

Finally, for reasons that do not involve quantum phase transitions, it is important to understand the interplay between disorder and vortices, which might be investigated in 2D ultracold gases. Superconductors are known for the Meissner effect, an expulsion of all magnetic fields inside the superconductor. However, most high-Tc superconductors are type II, meaning that above a critical amount of magnetic field, flux penetrates the material in quantized vortices. These vortices are small areas of non-superconducting material, shielded from the rest of the superconductor by the Meissner effect. The magnitude of external field required to penetrate the superconductor is often very small, perhaps μG , meaning that these systems almost always have vortices penetrating the superconductor. These vortices repel one another and form lattices when the flux is large, creating “vortex lattices” [2]. Because the vortices are bundles of magnetic flux, they also move perpendicular to current flow in a superconductor, causing a small amount of resistance as they traverse the material.

In fact, this resistance would make high-Tc superconductors nearly useless if not for the fact that vortices can be pinned by disorder [24]. If vortices are pinned, they don’t move in the presence of current, so there is no resistance caused by their movement. Dissipation-free flow in the superconductor is restored. A great deal of

work is currently focused on maximizing this pinning by changing doping and carrier concentrations, allowing superconductors to work in a wider variety of magnetic field strengths. Thus, it is important to understand the interplay between disorder and vortex transport. If the true microscopic mechanism for the BKT phase transition is the unbinding of vortex pairs, then we expect that adding disorder near this phase transition should help us to understand how a disordered potential interacts with vortices in 2D systems. Because of the fine control and unique measurements possible in cold atom systems, we should be able to explore measurements that cannot be done in other systems.

The long-term motivation for studying disorder in 2D ultracold Bose gases is therefore to answer some interesting questions and gain insight into the mechanisms behind high- T_c superconductivity. With better understanding of these materials, room-temperature superconductivity might become possible, an achievement possibly on par with the discovery of the transistor. Because of their Lego-like building block characteristics, ultracold gases make excellent quantum simulators. However, there are some hurdles to be overcome, mainly due to the finite size, non-uniform density, and interparticle interactions in ultracold gases. These hurdles are discussed in the next section.

1.3 2D Ultracold Gases

This section describes the work that has been done so far with ultracold Bose gases in 2D **without** disorder. There are many interesting questions still unan-

swered. We wish to discern what types of phases and transitions can exist in 2D ultracold Bose gas systems. The four possible phases are the thermal gas, superfluid, BEC, and quasicondensate - BEC with a fluctuating phase. The system considered is a dilute gas of bosons which has very precisely controllable temperature. Experimentally, the external trapping potential confining these systems modifies the density, and interactions between atoms become very important at the high densities and low temperatures required for any transition. This gives us four total cases to consider: with or without an external trapping potential, and with or without interactions. For a uniform system in 2D, there is no possibility of BEC, with or without interactions. However, there can still be a transition to a superfluid at low temperatures if there are interactions. There is a critical temperature at which the system transforms from a superfluid to a regular fluid, mediated by vortices. This is a BKT transition in a superfluid system. In the absence of interactions, there is no phase transition, but the first-order correlation function gradually changes from a Gaussian to exponential function.

Next, consider a harmonically trapped system. For a trapped ideal gas with no interactions, a true BEC is possible [11]. In an ultracold trapped atom system with weak interactions (the regime of most current experiments), a true BEC is expected at near-zero temperature, with a BKT transition to a superfluid at slightly higher temperatures, and finally a transition to a quasicondensate non-superfluid at a higher temperature [138, 38]. So, for the four different cases considered, true BEC is only theoretically possible for a trapped gas, and for a trapped gas with weak interactions, only in the case of near-zero temperature. However, a BKT

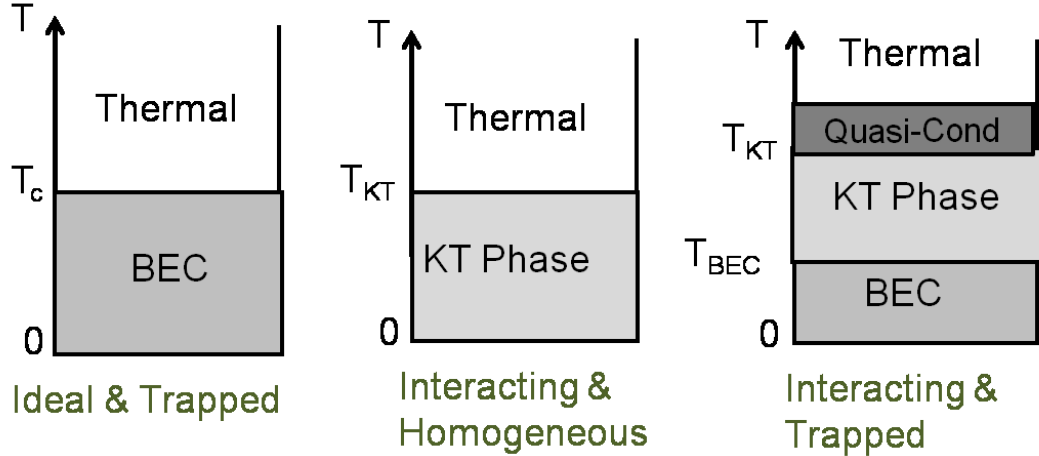


Figure 1.4: In a trapped, non-interacting gas, true BEC occurs at non-zero temperature. In an interacting homogeneous gas, no BEC occurs, but there is a BKT transition to superfluid. In the trapped, interacting case, there can be superfluid BEC, non-BEC superfluid, as well as a fluctuating-phase, non-superfluid quasicondensate [38]. There is no phase transition in a non-interacting homogeneous system (not shown). Figure adapted from [143].

type transition to a superfluid occurs in all cases except the infinite uniform non-interacting fluid. This information is summarized in Fig. 1.4

The phenomena of superfluidity and BEC are closely related, but the connection is very subtle. Superfluidity is the more general phenomenon. Superfluidity is defined by its transport properties, while BEC is a description of the multi-particle quantum state. A non-condensed superfluid in 2D lacks the one-body correlation length coherence of true BEC. A true condensate is phase coherent over its entire area, while a quasi-condensate can still have phase fluctuations, and also be non-superfluid. For a more detailed explanation of the subtle connection between BEC, quasicondensate and superfluid, see the appendix of [25].

1.3.1 Non-Interacting Systems

For the case of no interactions between the particles in our system, there are two different behaviors depending on the presence of a harmonic trapping potential. We are always interested in the behavior of the first order correlation function

$$g_1(r) \equiv \langle \hat{\Psi}^\dagger(r) \hat{\Psi}(0) \rangle, \quad (1.1)$$

where $\hat{\Psi}(r)$ is the annihilation operator for a particle at a position r . The long range behavior of this quantity tells us about the phase of the system. For a BEC, g_1 stays finite as r approaches infinity. In 2D, as has been mentioned, this is an impossibility. Long wavelength phonons always cause g_1 to decay as a function of r by causing positional fluctuations of the phase of the quantum state. However, the functional form of g_1 can differ above and below any phase transition, even if true long range coherence does not exist.

For the case of a uniform non-interacting fluid, there is no phase transition. However, there is still a gradual change in the functional form of g_1 , which goes from Gaussian in the regular phase to exponential when the phase space density gets very large [75]. The length scale of the decay of these correlations is related to the thermal deBroglie wavelength $\lambda = h/\sqrt{2\pi m k_B T}$, with m the mass of the particle and T the temperature. Thus, in the high temperature regime

$$g_1(r) \approx n e^{-\pi r^2/\lambda^2}, \quad (1.2)$$

with n the particle density. Meanwhile, at much lower temperatures,

$$g_1(r) \approx e^{-r/l}, \text{ with } l \approx \frac{\lambda e^{n\lambda^2/2}}{\sqrt{4\pi}}. \quad (1.3)$$

From Eq. 1.3, we see that we can increase the correlation length l by reducing the temperature of the system. This indicates that true BEC might be possible in a finite system, as we could perhaps lower the temperature to the point when l spans the entire system. Indeed, it can be shown that for a non-interacting Bosonic collection of atoms in an isotropic trap $U(r) = U_0(\frac{r}{a})^\eta$, BEC occurs at the critical temperature [11]

$$k_B T_{BEC}^{2D} = \left(\frac{N h^2 U_0^{\frac{2}{\eta}}}{2\pi^2 m a^2 g_2(\eta, 0)} \right)^{\frac{\eta}{2+\eta}}, \quad (1.4)$$

where N is the number of atoms, and

$$g_2(\eta, 0) = \Gamma\left(\frac{2}{\eta} + 1\right) \zeta\left(\frac{2}{\eta} + 1\right), \quad (1.5)$$

with ζ the Reimann Zeta function and Γ the gamma function.

1.3.2 Interactions in a Uniform System

In order to describe how interactions affect 2D physics, we must describe how the particles interact. We would like to describe two-dimensional scattering using a contact interaction $g_2\delta(x)$ in two dimensions, but in general the scattering potential is energy dependent, so this cannot be done. However, for low energy scattering in a situation where the confinement in the third dimension is not too tight, we can get an approximate g_2 which is energy independent. Consider two particles of mass m moving in a two dimensional plane with low energy so that the scattering is isotropic. The scattering state is [3]

$$\psi_{\mathbf{k}}(\mathbf{x}) \approx e^{i\mathbf{k}\cdot\mathbf{x}} - \sqrt{\frac{i}{8\pi}} f(k) \frac{e^{ikr}}{\sqrt{kr}}, \quad (1.6)$$

where \mathbf{k} is the incident wave vector and $f(k)$ the dimensionless scattering amplitude for the relative energy $E = \hbar^2 k^2/m$. At low energy, the scattering amplitude is

$$f(k) = \frac{4}{-\cot \delta_0(k) + i} \rightarrow \frac{4\pi}{2 \ln(1/ka_2) + i\pi}, \quad (1.7)$$

which defines the two dimensional scattering length a_2 .

We are interested then in a value of a_2 . We will assume that we have a system in three dimensions tightly confined in z such that the potential along z , $V(z) = m\omega_z^2 z^2/2$ confines the atoms in the Gaussian ground state. This means that $\mu, k_B T \ll \hbar\omega_z$. The scattering amplitude has been calculated using bound states to be [117, 118, 53]

$$a_2(a) = l_z \sqrt{\frac{\pi}{B}} \exp\left(-\sqrt{\frac{\pi}{2}} \frac{l_z}{a}\right), \quad (1.8)$$

with $B = 0.905$, a the 3D scattering length, and $l_z = [\hbar/(m\omega_z)]^{1/2}$ the relevant confinement length scale in the third dimension. Plugging Eq. (1.8) into Eq. (1.7) yields

$$f(k) = \frac{4\pi}{\sqrt{2\pi} l_z/a + \ln(B/(\pi k^2 l_z^2)) + i\pi}. \quad (1.9)$$

In all 2D experiments performed so far, the confinement length l_z has been much larger than a so that the imaginary term and the logarithm in the scattering amplitude are negligible, meaning that

$$f(k) \approx \sqrt{8\pi} \frac{a}{l_z} \equiv \tilde{g}_2, \quad (1.10)$$

where \tilde{g}_2 is a dimensionless scattering length. We can use \tilde{g}_2 to characterize virtually all of the behavior of the interactions in our 2D system.

In a uniform interacting system, there is one phase transition from a normal fluid to a superfluid via the BKT mechanism. As described in Sec. 1.2, the microscopic mechanism behind this transition is the binding of vortex pairs. A simple argument gives a remarkably satisfying expression for the critical temperature of this phase transition. We would like to calculate the free energy $F = U - TS$ of an unbound vortex, with U the energy of the vortex, T the temperature of the fluid, and S the entropy of the vortex. First, we can assume, without loss of generality, that the system is circular with size R , and say that the size of the vortex core is r_0 . We can calculate the energy of a vortex by assuming that the velocity field is $v = (\hbar)/(mr)$. Then

$$U = \pi \rho m \int v^2(r) r dr = \frac{\pi \rho \hbar^2}{m} \ln \left(\frac{R}{r_0} \right), \quad (1.11)$$

with ρ the *superfluid* density. The entropy is determined by the number of ways that we can place a vortex of size r_0 in a system of size R , giving

$$S = k_B \ln \left(\frac{R^2}{r_0^2} \right), \quad (1.12)$$

which means that

$$F = \frac{\pi \hbar^2 \rho}{m} \ln \left(\frac{R}{r_0} \right) - k_B T \ln \left(\frac{R^2}{r_0^2} \right) = \frac{k_B T}{2} (\rho \lambda^2 - 4) \ln(R/r_0). \quad (1.13)$$

We can immediately see that the free energy changes sign when $\rho \lambda^2 = 4$, with λ again the deBroglie wavelength. Because the system size R is much larger than r_0 , the coefficient of the free energy is large, meaning that this free energy goes from being large and negative to large and positive at the transition. This corresponds

to a free vortex being thermodynamically either very likely or very unlikely, and provides clear evidence of the phase transition.

An important point here is that ρ is the superfluid density of the system, and not the bare system density. These two quantities are not synonymous, and they can be very different, especially in a non-uniform system at finite temperature. Therefore, calculation of the transition temperature for an interacting cold atom gas is complicated. A combination of analytical [61] and numeric [123, 124] efforts have led to the critical phase-space density

$$D_c = (n\lambda^2)_c = \ln\left(\frac{C}{\tilde{g}_2}\right), \quad (1.14)$$

where n is the total system density and $C = 380 \pm 3$ has been calculated by classical field Monte-Carlo technique [123]. In a uniform system, this is expected to be the transition point from normal fluid to superfluid.

1.3.3 Interactions in a Harmonic Trap

Things get more complicated when a harmonic trap is added to this picture. The density is non-uniform, which means that the phases in the trap can become mixed. There are many ways to approach this, with the most intuitive being the use of the local density approximation (LDA). The local density approximation is made by substituting a local chemical potential of the form [75, 116]

$$\mu(r) = \mu - V(r) - \frac{2m\tilde{g}}{\hbar^2}n(r), \quad (1.15)$$

into the equation of state for the number of atoms in the gas. In this equation, μ is the bare chemical potential, $V(r)$ is the external trapping potential, and $n(r)$ is

the density of the atoms. The equation of state for the phase space density D of spinless bosons is

$$D = \int_0^\infty \frac{dx}{\frac{1}{Z}e^x - 1} = -\ln(1 - Z), \quad (1.16)$$

where $Z = e^{\beta\mu}$ is the fugacity. It is interesting to note that using the LDA in the case of no interactions ($\tilde{g} = 0$) yields a prediction for the critical atom number for the BEC transition with no interactions in an isotropic harmonic trap of frequency ω [75]:

$$N_c^{id}(T) \approx \frac{\pi^2}{6} \left(\frac{k_B T}{\hbar\omega} \right)^2. \quad (1.17)$$

This is the same result that can be derived straight from the density of states of spinless non-interacting bosons. However, this result using the LDA corresponds to a diverging spatial density in the center of the trap.

In the presence of interactions, the behavior of the equation of state changes significantly. As one might reasonably guess, the repulsive interactions prevent the divergence of the spatial density at the center of the trap, and thus prevent BEC. Experimental results suggest it is valid to assume that the BKT phase transition happens when the density at the center of the trap using the LDA reaches the density given by Eq. 1.14, the critical density in a uniform system. It can be shown that the critical atom number to reach this central density in the presence of interactions using this mean-field version of the LDA is [85, 84]

$$\frac{N_c^{(mf)}}{N_c^{(id)}} = 1 + \frac{3\tilde{g}}{\pi^3} D_c^2. \quad (1.18)$$

This is a fairly simple and powerful equation for determining the critical atom number. In practice, the most important corrections to Eq. 1.18 come from the

fact that the experiments are “quasi-2D”. There are generally still some atoms in the excited states along the tightly confined z-direction, which modifies the volume assumed to get $N_c^{(id)}$. The excitations along this direction can be accounted for either semiclassically [86] or with quantum Monte Carlo calculations [85], with the result that the critical density has to be ~ 4 -5 times higher than predicted in Eq. 1.18 due to deviation of the density distribution from the strictly 2D case [77]. It was difficult to see this correction experimentally, as at the BKT phase transition, there is no discontinuous jump in any quantity other than the non-observable superfluid density. The critical point was eventually extrapolated from data showing the linear dependence of interference contrast on atom number [96], which does seem to have sharp jump at the transition.

Now that we have developed some intuition for the BKT phase transition, we need to address the two other phases represented in the interacting trapped case in Fig. 1.4. It has been shown using a classical field Monte-Carlo analysis that the atom cloud develops an extended phase coherence over the entire cloud at temperatures 10-20% above the BKT transition temperature [22]. This could be regarded as a non-superfluid condensate; the BKT transition has not happened, so there is no superfluidity, but there is some coherence, with a fluctuating phase [90]. This fluctuating phase prevents true superfluidity. Meanwhile, it is theoretically predicted that at very low temperatures, a true BEC can be obtained, although this has not been observed yet [25]. It should be noted that there has been a great deal of theoretical work on the different phase transitions in an interacting trapped sample beyond what was presented here. I hope to have given the most

straightforward and easily understandable approach to the problem, even if it is not the most involved or the approximation is not accurate. Still, the mean-field LDA does match the experiments discussed in the next section. For more information on other theoretical work, see the reviews available in Refs. [75, 25, 122] and references therein.

1.3.4 2D Ultracold Bose Gas Experiments

A large number of experiments have been performed in 2D ultracold Bose gas systems. The goal of most of these experiments is to identify the different phases of the gas by examining correlation lengths or density/momentum distributions. Some of the earliest investigation was done in the group of Wolfgang Ketterle [71] and Massimo Inguscio [30], and early work with phase defects was done in the group of Jean Dalibard [78, 144, 143]. This was followed by investigations of the BKT transition as a function of temperature [76] and atom number [96, 38, 77]. The most recent experiments have revealed the equilibrium density distribution of a quasi-2D Bose gas [126] and shown universal scale invariance right at the BKT phase transition [87].

Most of the experiments have struggled with the differences between 2D and 3D. In 3D, the ideal gas approximation is surprisingly accurate, while the 2D physics is strongly dependent on the interactions and fluctuations of the atoms near the critical region. In addition, the appearance of a bimodal distribution in momentum, the consequence of Bose-Einstein condensation in a 3d harmonic trap, is a relatively

easy experimental signature of the 3D BEC phase transition. The appearance of a bimodal distribution or even phase coherence, observed by interfering the system with a phase reference, is not enough to show a phase transition in 2D, and so experimental signatures of 2D phase transitions are more difficult. It now seems that the BKT phase transition happens at a phase space density somewhat higher than where the system develops phase coherence or a bimodal distribution. However, this region is still within reach of the experiments, and the theory developed in this section provides strong corroborative evidence of the observation of the BKT superfluid phase transition. There is still no consensus as to whether true BEC is possible in experiments involving trapped interacting atoms, and no evidence has yet been put forth.

1.4 Disordered Ultracold Gases

There are many groups working on experimental implementations of disorder in ultracold gases [59]. Aside from investigation into the basic behavior of atoms in a disordered potential [35, 39, 45, 41, 101], there has been a big push to observe two different types of physics typically associated with condensed matter systems. The first is Anderson localization [5], the lack of diffusion of non-interacting particles in the presence of a disordered potential. This effect has been realized in ultracold gases [19], along with an experimental observation [129] of localization in the closely-related Aubry-André model [10]. The second pursuit is for an experimental observation of a Bose glass phase [64] in an optical lattice. Work in this direction

has been done in Ref. [58], and the corresponding disordered Bose-Hubbard model has also been explored in Refs. [106, 151]. These experiments reveal that the effects of disorder in ultracold gas systems are analogous to the effects in solids, and add credence to the motivation of using ultracold gases in quantum simulation.

For the purposes of the work performed in this thesis, the most useful results from these experiments analyze how a BEC responds to a disordered potential. It turns out that in equilibrium, disorder introduces small density modulations in quasi-1D BEC's [35, 39]. When the atoms are released from the trap, these initially small modulations quickly convert (via mean-field interactions) into phase fluctuations which lead to large density modulations later in the expansion, when the atoms are typically imaged [39]. If the disorder strength is increased to the point that the condensate fractures initially, then the random phases of each of these pieces destroy the modulations during expansion. There has not been much work done on this outside of quasi-1D systems, but the physics should be similar.

1.5 Disordered 2D Experiments

There has been very little work done on Bosonic 2D systems with disorder. One very recent experiment in ultracold atom systems has observed anisotropic diffusion in 2D in the presence of a disordered potential [130], most likely as a precursor to a measurement of Anderson localization. There has also been some experimental work on the BKT transition in disordered thin films of ^4He [99] or CaF_2 [100], along with a theoretical effort to explain the results [12]. These experiments showed that

disorder broadens the sharp jump in superfluidity, but this broadening might be caused by the finite size of the system.

We can use the body of knowledge about 2D ultracold gases to lead our intuition about experiments with disorder in 2D. The results of these experiments can help us to constrain models of superconductivity, determining whether observed phase transitions in superconductor systems are truly bosonic or perhaps whether they involve the Coulomb interaction. The ability to observe vortices and measure correlations in ultracold atom systems should lead to new insights which cannot be gleaned from condensed matter systems. The interactions between disorder and vortices might be better understood through these investigations as well.

It should be emphasized that the difference between the experiments presented here and previous experiments on 2D ultracold gases is the addition of disorder. Until now, there has been no experimental study of the effect of disorder on the properties of the BKT phase transition in ultracold gases, though the phase transition **without** disorder has been investigated (Sec. 1.3.4). Preliminary results in our system indicate that disorder smoothly destroys the integrated visibility of interference patterns that indicate long range phase coherence. It is less clear whether the disorder has any effect on the thermally activated vortices in the system.

The structure of this thesis is to provide a background for the basic experimental apparatus used to create BEC's in Chapter 2, followed by a detailed look at this process in Chapter 3. Chapter 4 details how we confine our 3d BEC to two dimensional dynamics and add a disordered potential. Finally, the measurements and results are presented in Chapter 5.

Chapter 2

Experimental Sequence

2.1 Overview

This section describes the physics behind our basic experimental set-up. I have chosen to separate the theory behind our experimental set-up from the construction. Much of the theory has been well described in the references given in this section. Therefore, this is a very brief introduction to the method that we use to obtain Bose-Einstein condensates. Where possible, I will point out how our set-up differs from the “typical” BEC set-up. Putting the theory first will help motivate the reasons behind the physical construction of the apparatus described in Chapter 3.

The starting point of almost everything that we do is a BEC. In order to form a BEC in a dilute gas, we must trap and cool a source of thermal atoms at 373 Kelvin to temperatures of only a few tens or hundreds of nanoKelvin, nearly ten billion times colder. To date, there are only a few ways of attaining these tremendously cold temperatures in dilute gases [116]. The main method to do the bulk of the cooling is laser cooling, followed by evaporation [92], with confinement in either an optical [72] or magnetic trap [18]. In our experiment, we use both types of confinement. In addition, it is not uncommon to transport atoms to other areas of a set-up, as in [73], which we also do. A typical experimental sequence consists of the following steps:

1. Zeeman slow a thermal beam of atoms
2. Load a Magneto-Optic Trap (MOT)
3. Transfer from the MOT to a magnetic trap
4. Cool using radio-frequency evaporation (can cool to BEC)
5. Load an optical trap
6. Transport the atoms to a science chamber
7. Turn on the second optical trapping beam for additional confinement
8. Optically evaporate to BEC

2.2 Thermal Source and Zeeman Slower

Our source of atoms is a heated pool of rubidium inside our vacuum chamber. It is described in more detail in Section 3.2.2 and in [55]. The atoms are heated to 100 °C, and then sent through a tube so that a beam of atoms enters the region where we do our trapping and cooling. If the tube length is chosen appropriately, then the transverse velocity of the beam can be made small.

The atoms in the beam are moving too fast to be captured by the MOT, so the first stage of cooling is done using a Zeeman slowing technique [120, 14, 109, 49]. This is one of many cooling techniques that makes use of the fact that photons carry momentum. When an atom absorbs a photon, it absorbs the momentum of the photon. At a later time, it will re-emit this photon through spontaneous

emission, getting a momentum kick opposite to the direction of emission. However, because the direction of spontaneous emission is random and symmetric (such as a dipole pattern), the average momentum kick after many emission events is zero. Therefore, if an atom absorbs a large number of photons from a laser, there will be a net momentum transfer in the direction of laser propagation, as the re-emission kicks will average to zero. This momentum transfer can be used to slow the forward velocity of the beam.

Since the atoms only absorb an appreciable number of photons if the laser frequency is within a few linewidths of the atoms' resonant frequency (6 MHz for ^{87}Rb), the only trick to this technique is keeping the laser on resonance with the atoms. The atoms have a changing effective resonance frequency as they slow due to their changing Doppler shift. This is compensated by a changing magnetic field as the beam propagates.

We use a $\sigma^+ - \sigma^-$ hybrid slower design, as in Ref. [15, 154]. Since different atomic hyperfine levels shift differently in a magnetic field, the laser will only be on resonance between two hyperfine levels. Therefore, optical pumping to different sublevels should be kept to a minimum. In original slower designs, this was implemented by picking either σ^+ or σ^- for the polarization of the slower beam. With this polarization the atom only makes transitions between two states. For example, for σ^+ polarization, with the laser on resonance for the $F = 2$ to $F' = 3$ D_2 transition hyperfine state (Fig. 2.1), the $F = 2, m_F = 2$ ground state magnetic sublevel can only make a transition to the $F' = 3, m_F = 3$ excited state, even in zero magnetic field, and the only allowed decay is back to the $m_F = 2$ ground state, creating an

effectively two-level “stretched state” system. If the laser was π polarized, the atom could be pumped and decay among different magnetic sublevels, possibly shifting the atom completely off resonance if a magnetic field is present.

The two different polarizations require two different magnetic field profiles to keep the atoms on resonance, as shown in Fig. 2.2. For σ^- polarization, the energy levels get closer together in higher field, while for σ^+ polarization, the energy levels get farther apart in higher field. Since the Doppler shift pushes the excited state to lower energy, σ_+ slowing requires a *decreasing* magnetic field as a function of position, with the laser frequency above the bare (no field or Doppler shift) resonance, while σ^- slowing requires the opposite. A hybrid slower starts in a high field as a σ^+ slower, but the field crosses zero at some position, switches sign, increases in magnitude again, and becomes a σ^- slower. Only one laser is needed for this. At the zero crossing, the atoms must be moving fast enough to diabatically change their spin from the “+” stretched state to the “-” stretched state. Because the direction of the field has changed, the polarization of the incoming beam changes, now becoming σ^- light for the new switched magnetic field axis.

This approach has advantages over each of the non-hybrid designs. The σ^+ slower design has the disadvantage that because the magnetic field must be small at the exit of the slower, the slowing laser must be close to resonance. Since the atoms are supposed to be captured in a MOT after slowing, the slower beam always passes through the MOT, making it undesirable for the slower beam to be near resonance. The σ^- slower solves this problem, since the magnetic field will be large at the exit of the slower. The advantage of the hybrid slower over the σ^- design is that the

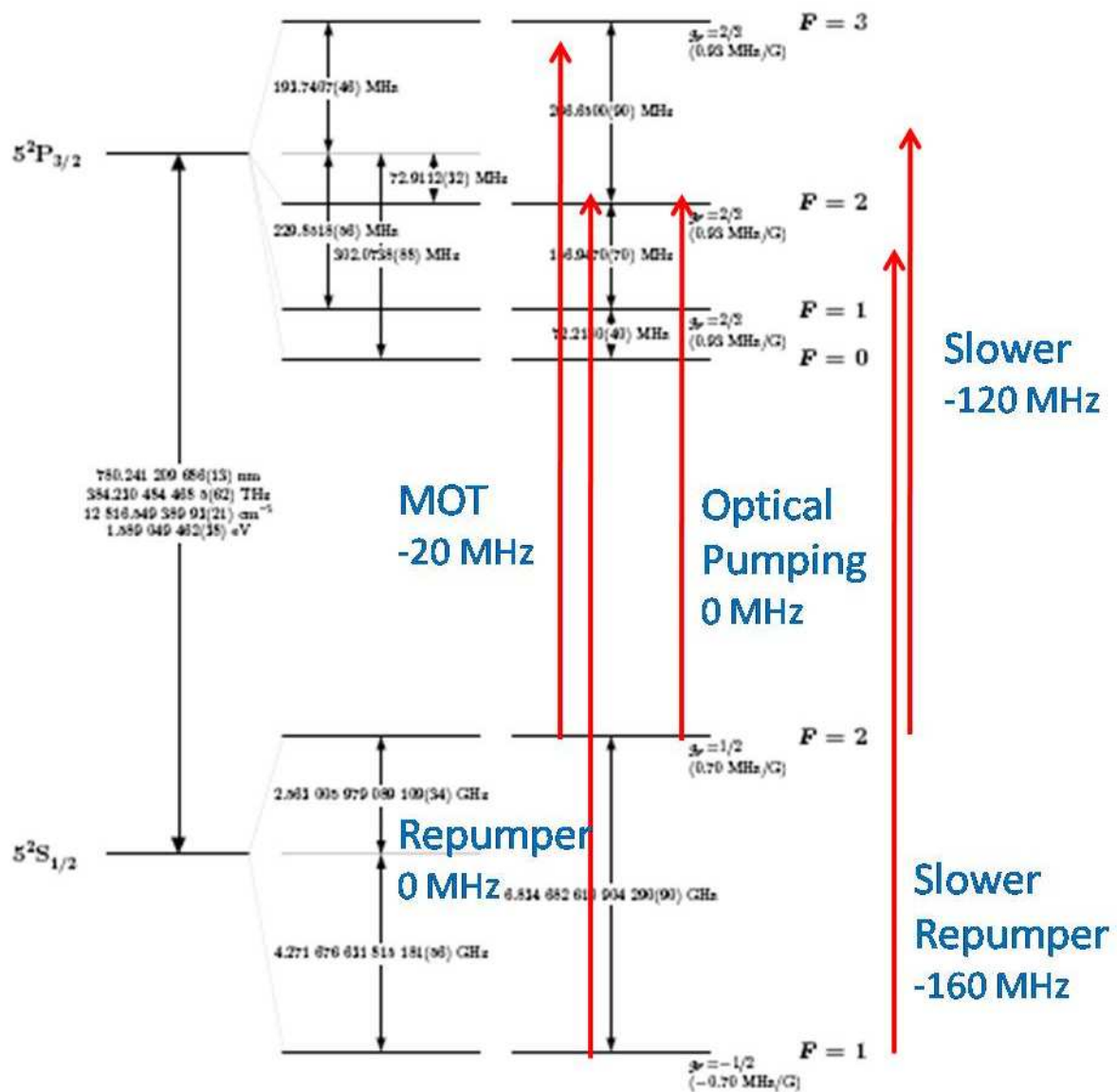


Figure 2.1: ^{87}Rb level structure, with arrows indicating transitions used in the experiment. Frequencies are detunings from nearest indicated transition.

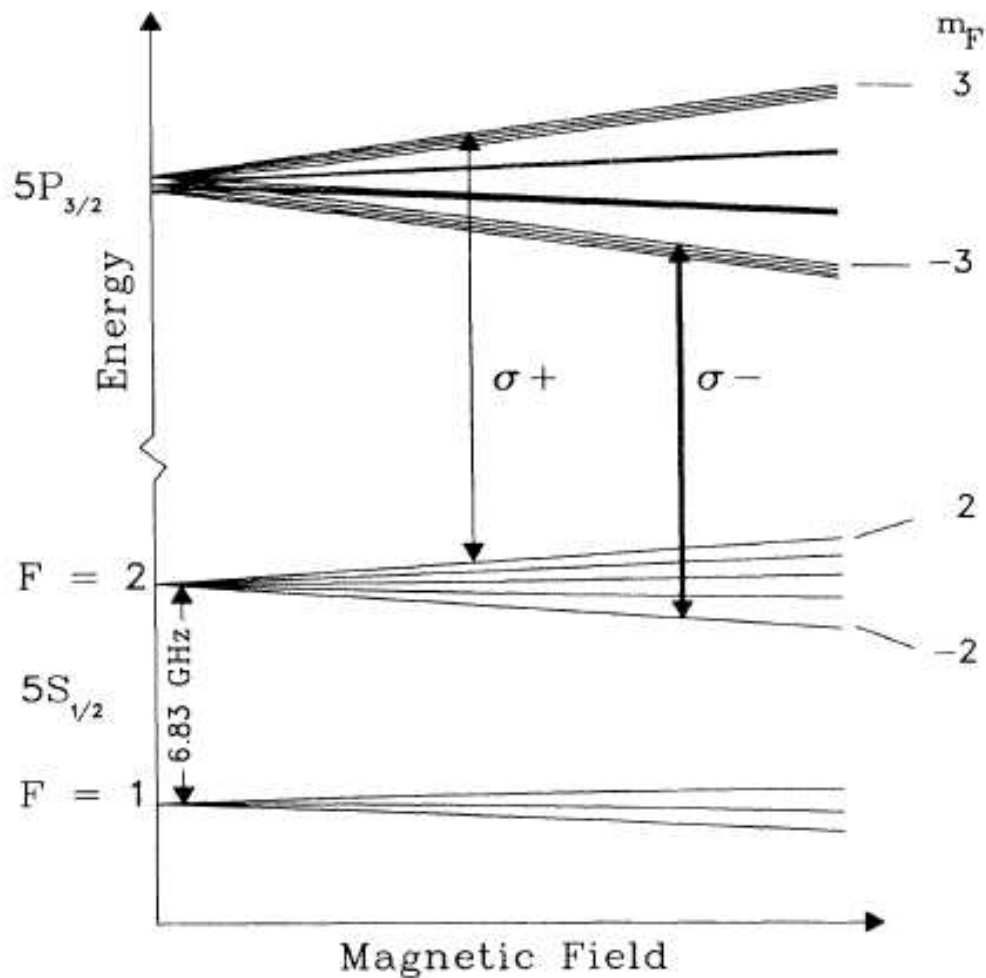


Figure 2.2: ^{87}Rb Zeeman splitting, D_2 excited state and ground state. Allowed level transitions for given polarizations are indicated. Figure from [14].

total amount of required current is less. The total amount of slowing is proportional to the total difference in magnitude of the field. Because the field in the hybrid design crosses 0, the total magnitude *difference* can be large without either of the individual maximums being large. This results in a lower overall amount of current in the coil, less required power and cooling, and less stray field at the end of the slower.

2.3 MOT

The MOT is perhaps the most important tool in cold-atom physics [125, 109]. It combines the momentum transfer technique used in the Zeeman slower with a position-dependent force supplied by a magnetic field gradient. This traps the atoms in a volume on the order of mm^3 at temperatures on the order of 100's of μK .

To get an idea of how a MOT works, it is easiest to consider a 1D example. Imagine that an atom is sitting at the intersection of two counter-propagating beams, each detuned slightly below the atomic resonance of the atom. If the atom starts to move, its Doppler shift will make the beam propagating opposite to its velocity seem closer to resonance. This makes it more likely to absorb photons which will slow its velocity, supplying a velocity-dependent force. However, this force does not confine the atoms, since there is no position dependence to the light force. A magnetic field gradient is then applied to add position dependence to the light force, as in Fig. 2.3. Imagine that the atom has only one ground state with zero spin, and the excited state has three spin states. If the light carries the correct polarization, then the atom will be more likely to absorb a photon and transition to the level that is shifted closer to resonance. For example, in Fig. 2.3, if the atom is to the right of the center, the $m_e = -1$ level is closer to resonance, and the light propagating to the left has σ^- polarization. This makes absorbing a photon from that beam more likely. The reverse is true if the atom is to the left of the center of the trap. Thus, the combination of light polarization and magnetic field gradient supplies a position-dependent force to the atoms. A MOT then supplies both cooling, due

to the velocity-dependent absorption, and trapping, due to the position-dependent absorption. Generalization to 3D requires six beams, two from each direction, and a quadrupole field, creating the correct magnetic field gradients in each direction.

It should be noted that real atoms have more complicated level structure than shown in Fig. 2.3. In particular, in ^{87}Rb , there is another ground state lower in energy ($F = 1$). The atom can make off-resonant transitions to $F' = 2$ and then decay to the $F = 1$ ground state (see Fig. 2.1). This requires repumper lasers in both the slower and the MOT to put the atoms back into the cycling transitions. If this is not done, it only takes a few milliseconds for all of the atoms to end up in the wrong ground state.

There are many different ways to create the required combinations of lasers and magnetic fields for a MOT. Our MOT magnetic field is created by a U-shaped wire sitting a few mm away from the atoms, plus a constant bias field, similar to [74, 135, 153]. This field geometry restricts optical access, so we have a “mirror MOT” (Fig. 2.4). Instead of sending six beams at the atoms, there are four large beams. Two of the beams are reflected off of a mirror sitting in between the atoms and the U-shaped wire. Since the beams are large, these two beams hit the atoms both before and after reflection. For more details, see Section 3.4.

2.4 Magnetic Trap

The momentum transfer of the laser-atom interaction is useful to cool the atoms to a certain point, but the energy gain from each absorbed photon will set a

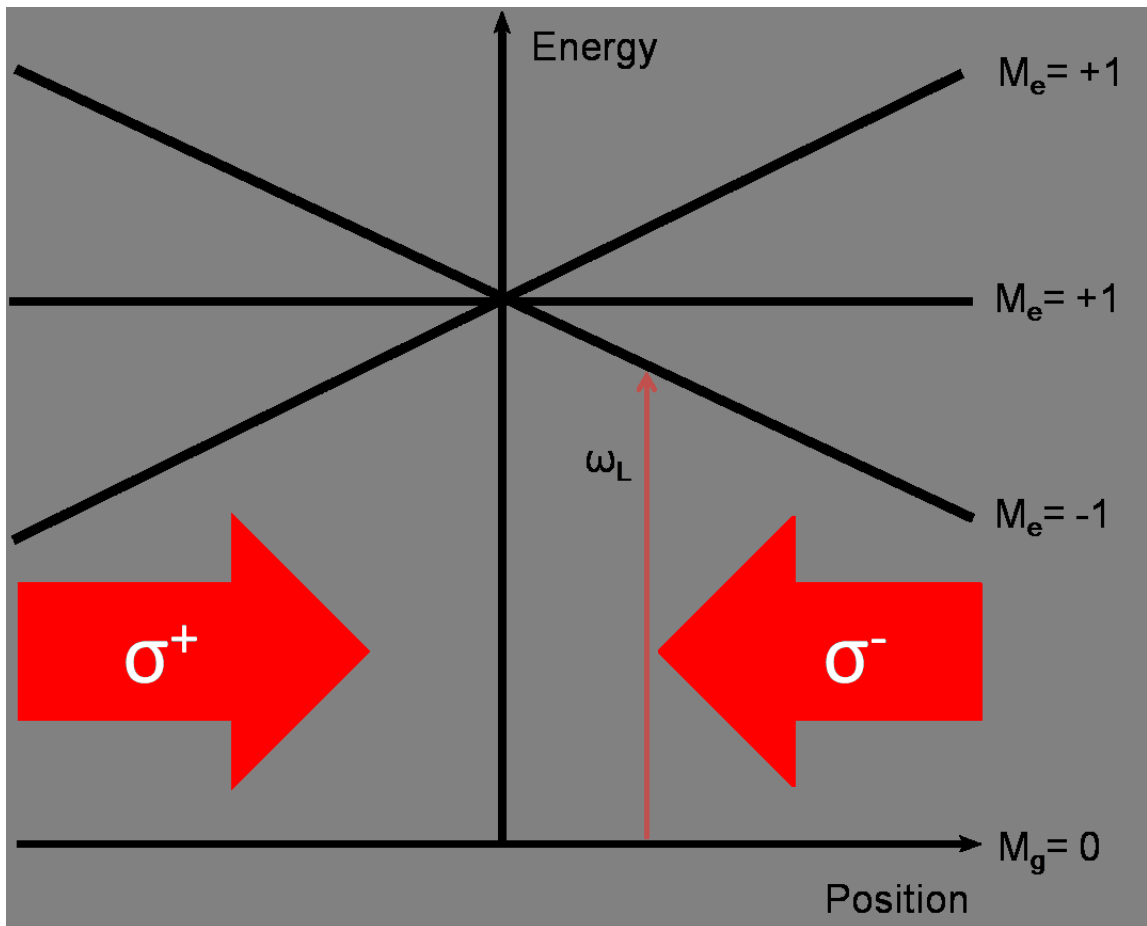


Figure 2.3: Simplified schematic of a MOT. The laser frequency ω_L is detuned lower than resonance to compensate the Doppler shift. A magnetic field gradient shifts the excited states so that on one side of the zero field, the $m_F=+1$ level is closer to resonance, with the opposite true on the other side of zero field. The laser polarizations must be as shown to make the transition to the correct spin state.

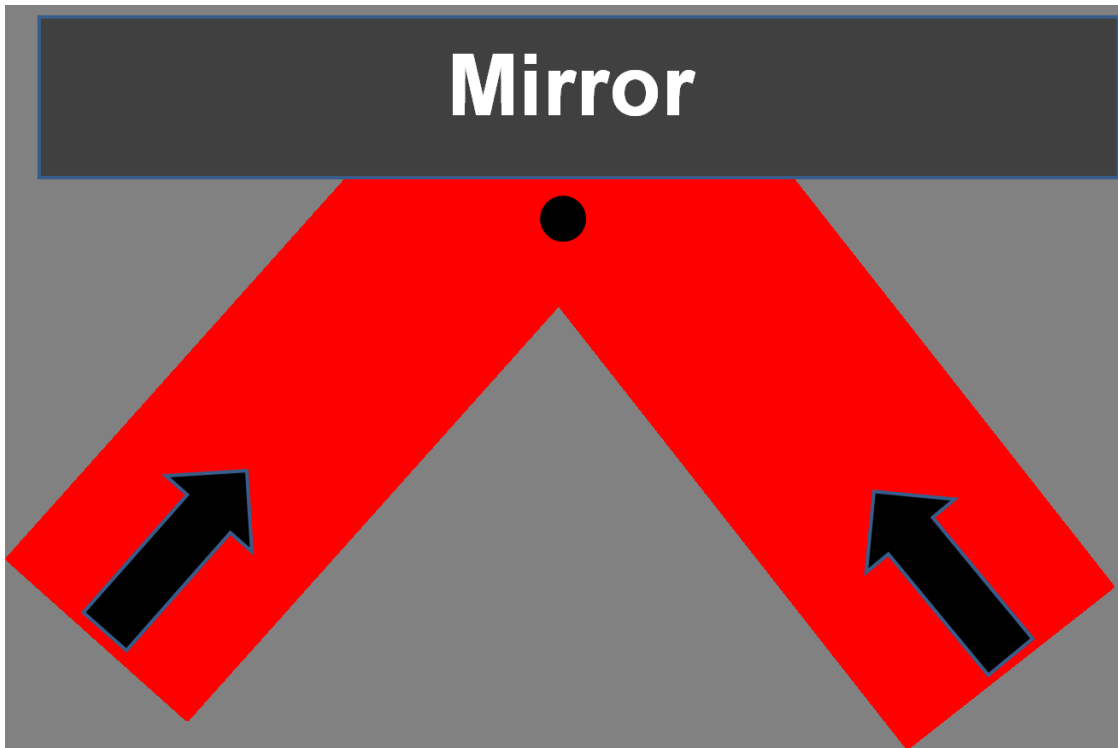


Figure 2.4: Schematic of “Mirror MOT” operation. Each beam hits the atoms (black circle) before and after bouncing off of the mirror, imitating perpendicular sets of counter-propagating beams.

lower limit on attainable temperatures in a MOT. Therefore, we transfer from the MOT to pure magnetic trapping.

Before transferring to the magnetic trap, we have a stage of additional cooling known as “optical molasses”. Optical molasses has attainable temperatures on the order of a few μK . Temperatures in a MOT are limited by the high atom density through “radiation trapping”. Photons emitted by one atom have a good chance of being reabsorbed by another atom in the MOT, creating an outward radiation pressure at typical MOT densities. This effect can be mitigated by decreasing the density of the MOT, which we achieve by momentarily turning off the magnetic field gradient and detuning the MOT beams farther from resonance, which decreases re-absorption. Because the magnetic field gradient is off, there is no longer confinement for the atoms, but there is cooling due to the beams. The temperature quickly drops, and then the atoms start to leave the original trapping area. We confine them in a magnetic trap before the size of the cloud grows too large.

Referring to Fig. 2.1, we see that there are two different ground states, $F = 1$ and $F = 2$. In addition, as seen in Fig. 2.2, these two levels are each split into different spin states which have different energies in non-zero magnetic fields. We choose to trap the $F = 2, m_F = 2$ spin state, which is at its lowest potential energy at the minimum of a magnitude field. An optical pumping pulse is applied just before turning on the magnetic trap to ensure that most of the atoms are in the correct state (Section 3.5).

Magnetic trapping works on the principle that the potential energy of an atom

with a magnetic moment

$$\mu_F = g_F \cdot m_F \cdot \mu_B \quad (2.1)$$

with g_F the Landé g-factor and μ_B the Bohr magneton, is given by

$$V(\vec{r}) = -\vec{\mu}_F \cdot \vec{B}(\vec{r}) \quad (2.2)$$

If you make the assumption that the atom is cold enough that its spin adiabatically follows the direction of the magnetic field, then only the magnitude of the magnetic field matters. Then, the sign of μ_F determines whether the atom is high-field seeking or low-field seeking. Because Maxwell's equations forbid a 3D magnetic field maximum in free space, magnetically trappable states are generally low-field seeking. In ^{87}Rb , these states are the $F = 2$, $m_F = 1$ and $m_F = 2$ states or the $F = 1$, $m_F = -1$ state (due to the change of sign of g_F between the two different F levels).

The type of trap we use is an Ioffe-Pritchard trap [109, 18]. Imagine four infinitely long current-carrying wires situated equidistant from each other. Each wire runs current in the opposite direction as its nearest neighbors. By symmetry, the magnetic field for these wires is constant along the axis of the wires. For any given plane along the wires, the magnetic field will be 0 at the center, and then increasing in any direction away from the center, as in Fig. 2.5. This configuration provides trapping for low-field seeking atoms in the plane. “Pinch coils” running current so the field from each coil points in the same direction are used to confine the atoms in the third direction. It is worth noting that the pinch coils run current in the same direction to prevent Majorana spin flips [28, 145]. The magnetic field magnitude would be zero at the center of the trap if the currents in the pinch coils

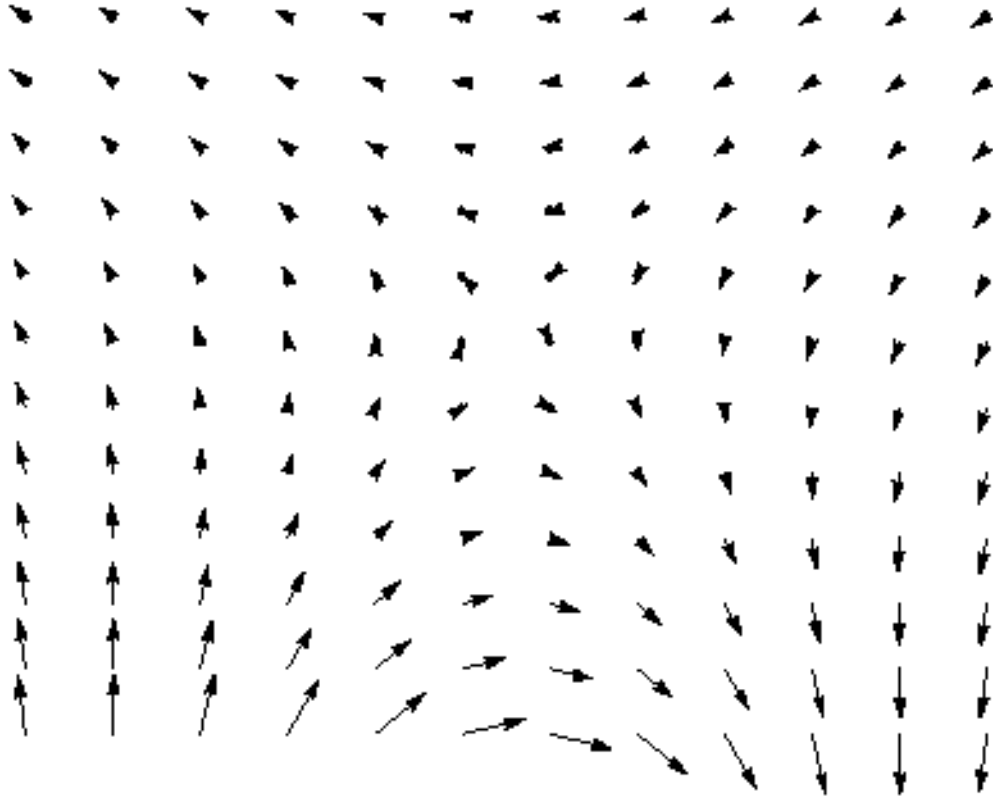


Figure 2.5: Vector field profile of 2D quadrupole. Direction of arrow indicates field direction, length of arrow indicates magnitude of field.

are opposite. If the atoms see a zero field, their spins cannot be defined, since there is no preferred axis in space. Then, if the atoms move away from the center of the trap, they might have flipped their spin with respect to the direction of the field they enter, causing them to become untrapped. Our trap uses a field profile very similar to this, but created in a very different way (Section 3.6).

2.5 RF Evaporation

RF evaporation in a magnetic trap is used to increase the phase space density of the gas by many orders of magnitude [82, 92]. It works by the same principle as

regular evaporation. In a trapped gas sample, the atoms have a Maxwell-Boltzmann distribution of energy. Our trap has a finite depth, and the atoms most likely to be found near the top of this trap have the most energy. If we lower the depth of the trap slightly, some of the atoms with the most energy will leave the trap. The atoms that are left will then rethermalize via collisions [102]. When they do, the average energy of the gas will be lower, indicating a lower temperature. This process can be repeated until the number of atoms gets too low to rethermalize efficiently. The efficiency of the process and lowest attainable temperature depend crucially on the collisional properties of the gas.

The RF photons lower the depth of the trap by causing transitions from trapped spin states to untrapped spin states. As seen in Fig. 2.2, the magnitude of the magnetic field changes the relative energy spacing between different spin states in a given F hyperfine manifold. This energy corresponds to radio frequencies, and the energy between states is greater in a larger magnetic field. The magnetic field magnitude gets larger farther from the center of the trap, and atoms with more energy will sample the regions of higher magnetic field. If the RF frequency is set to resonantly drive transitions between spin states for a magnetic field that only the highest energy atoms will sample, then the depth of the trap is effectively made smaller. The RF photons do not drive transitions for any atoms whose trajectories do not have enough energy to take them through the resonant magnetic field. If the RF power is set correctly, the process of ejecting atoms from the trap can be made nearly 100 percent efficient. By varying the frequency of the RF radiation, the trap depth can be modified to be nearly any value. Any atom with enough energy to

have a trajectory that samples the resonant magnetic field value will be ejected from the trap.

2.6 Optical Trap

Though RF cooling can be used to cool the sample below the BEC transition temperature, we often want to move the atoms to the “science chamber”, a small glass chamber with better optical access than the region used for magnetic trapping. We use an “optical tweezers” technique [73], loading the atoms into a focused-beam trap and then translating the focus to move the atoms.

Atoms interact with off-resonant light through the induced electric dipole moment. It can be shown that potential felt by a two-level atom in the presence of off-resonant light is given by [72]

$$U(\vec{r}) = \frac{3\pi c^2}{2\omega_0^3} \frac{\Gamma}{\Delta} I(\vec{r}), \quad (2.3)$$

with c the speed of light, ω_0 the natural resonant frequency of the atom, Δ the detuning of the laser from atomic resonance, Γ the decay rate of the excited state, and $I(\vec{r})$ the intensity of the laser. Equation 2.3 shows that the atom feels a potential which is linearly proportional to the intensity of an incident laser. In addition, the sign of the detuning determines whether the atom is attracted or repelled from regions of high intensity. We detune our laser below the atomic transition frequency, meaning that the atoms are attracted to the focus of the beam. Since the optical potential is not very deep, it is necessary to pre-cool using RF evaporation before loading atoms into the optical potential.

Once the atoms are loaded into the optical trap, the focus of the beam is translated and the atoms follow, moving a distance of approximately 30 cm. With the atoms in the science chamber, an additional beam is used to increase the confinement of the atoms. More cooling will be required once the atoms are moved, as the collision rate in the optical tweezer is insufficient.

Optical evaporation proceeds based on the same principles as RF evaporation. In this case, the depth of the trap is lowered by simply decreasing the intensity of the beam. However, the oscillation frequencies of the optical trap in the radial (ω_r) and axial (ω_z) directions are [72]:

$$\omega_r = \sqrt{\frac{4U(0)}{m\omega_0^2}} \quad (2.4a)$$

$$\omega_z = \sqrt{\frac{2U(0)}{mz_R^2}}, \quad (2.4b)$$

with U defined in Eq. 2.3, ω_0 the resonance frequency of the atom, m the mass of the atom, and $z_R = \pi\omega_0^2/\lambda$ the Rayleigh range of the laser with wavelength λ . Therefore, the oscillation frequencies, and hence the collision rate, also depend on the intensity of the beam [112]. Optical evaporation must follow a different trajectory of trap depth vs. time as the oscillation frequencies change during evaporation. Despite this, optical evaporation can still be very efficient, as the initial confinement is typically very tight, allowing a high collision rate. Our optical evaporation produces BEC's after about 10 seconds of evaporation.

The above experimental sequence producing BEC's in either the magnetic or optical trap is the starting point for most of the experiments that we do. A more detailed look at the technical details of the above sequence follows below, and the

design and implementation of lattices and disorder is described in chapter 4.

Chapter 3

Technical Details of BEC Production

3.1 Overview

This chapter details the experimental apparatus used to create BEC's. The intended audience is people that will be working in this lab in the future, or people that are building a BEC apparatus. Many of the topics covered here are also discussed in Ref. [55], including many of the part numbers for the equipment.

3.2 Vacuum

3.2.1 Main Chamber

In order to achieve Bose-Einstein condensation, we must be able to confine our gas of atoms with lasers and magnetic fields for about 30 seconds. This requires an ultra-high vacuum environment, on the order of 10^{-11} Torr, as collisions with background gases limit the amount of time we can hold atoms in a trap. In order to get and maintain this type of vacuum, all vacuum connections on the chamber are conflat-type, sealing with a stainless steel knife edge digging into a both sides of a copper gasket. There are two sections to the chamber, maintained at different pressures. The main UHV chamber is on the order of 10^{-11} Torr, while the Rubidium oven is at 10^{-9} Torr. Originally, the chamber was designed without an oven, using

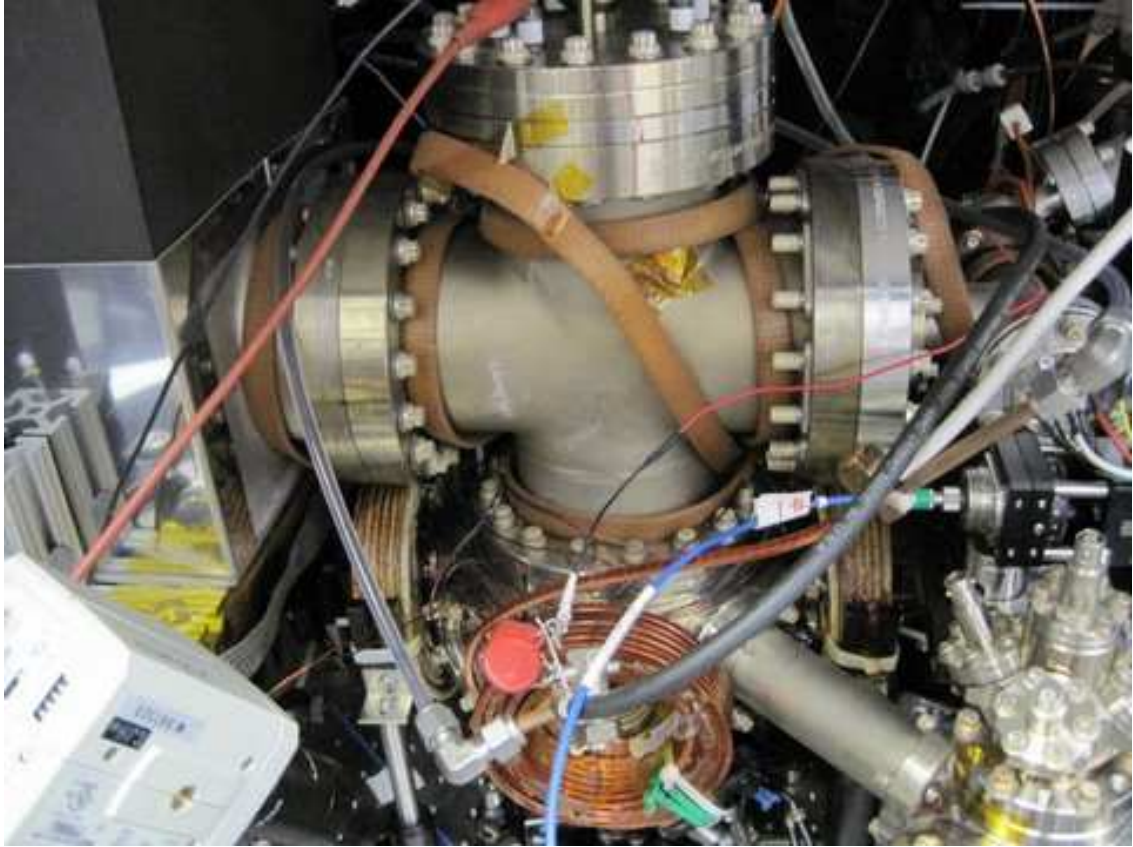


Figure 3.1: Picture of the outside of the main vacuum chamber. The 4 way cross is visible, as are 3 of the 4 coils attached to the spherical octagon. The ion pump is attached to the left side of the 4-way cross.

Rb getters instead [55].

The main UHV chamber is pictured in Fig. 3.1. The bottom is a spherical octagon, with 8 2-3/4" Conflat connections. This is connected on the top by 4-way 6" conflat cross. Attached at the top of the cross and hanging down into the spherical octagon is the structure shown in Fig. 3.2, used to create the magnetic fields for our MOT and magnetic trap (see Secs. 3.4, 3.6). One side of the cross is an ion pump with a titanium sublimation pump. The other side of the cross is reduced to 2-3/4" conflat and attached to a 2-3/4" T in order to put in a nude ion

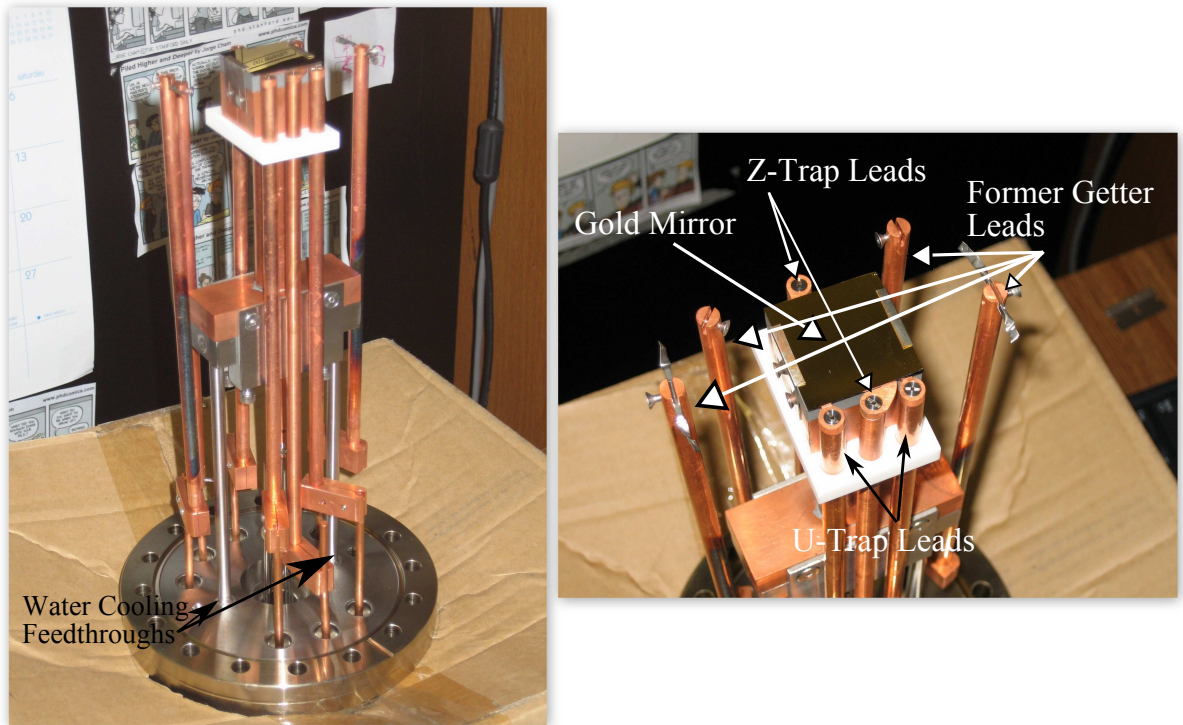


Figure 3.2: Structure to hold and cool the U and Z shaped wires used for the MOT and magnetic trap. The whole structure is mounted upside down from this picture inside the vacuum chamber.

gauge to measure the pressure in the chamber.

The spherical octagon has 5 of its 8 ports attached to vacuum windows, and a large 6" window on the bottom. Three of the windows are anti-reflection (AR) coated for 780 nm normal-incident light (MOT), while 2 of them are AR coated for normal-incident light at 1550 nm (optical trapping) (Fig. 3.3). The large window on the bottom is coated for 45°-incident 780 nm light. The other three ports on the octagon are used for the Zeeman slower, an extension for a microchannel plate (for studies on Rydberg atoms), and a science cell. The chamber for the microchannel plate is a 2-3/4" cube attached to a 2-3/4" nipple. The cube's 5 other sides have 2 blanks and 3 windows. The window on the microchannel plate chamber which looks in on the main chamber is coated for 1550 nm light, while the other two windows are coated for 780 nm.

The science cell is a quartz fluorometer cell available from Starna cells, part number 3/Q/20. It is 12.5 x 22.5 x 45 mm. We have this cell attached to a quartz-to-metal seal connected to a conflat flange by a company called Bomco. Interestingly, Bomco claims that the quartz to metal seal is insensitive to temporal temperature gradients. They said that just after making the seal at high temperatures, they dip the seal in liquid nitrogen to cool it. We have the optics shop and glass blower at NIST attach the fluorometer cell to the quartz to metal seal. A disc that is the same size as the cylinder attached to the flange is fritz-sealed to the cell, and then the glassblower attaches the disc to the cylinder (Fig. 3.4).

The structure inside the vacuum chamber has 2 leads for the U-shaped wire to create the MOT magnetic field, 2 leads for the Z-shaped wire used to create the

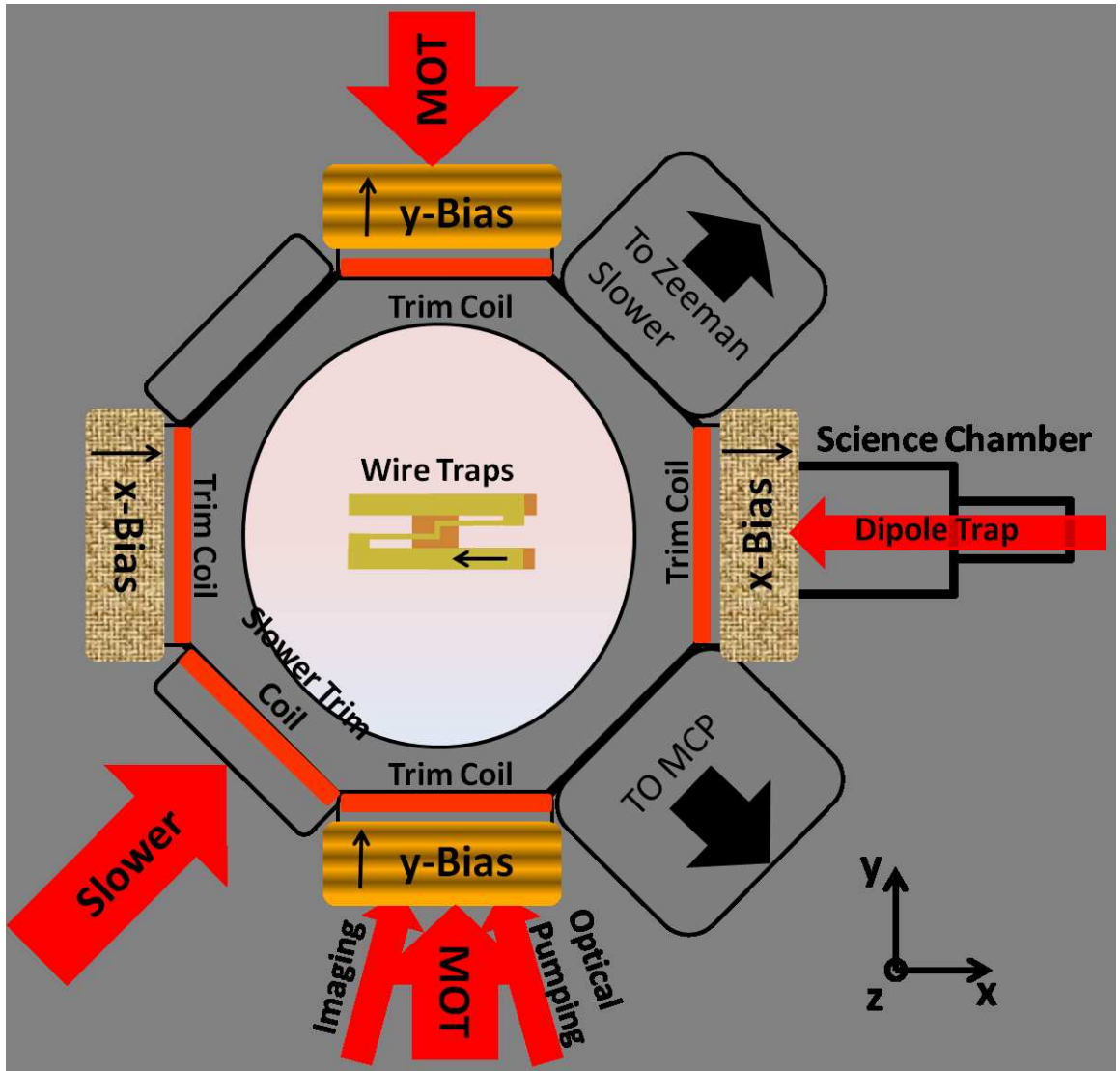


Figure 3.3: Top view of spherical octagon forming the bottom part of the main vacuum chamber. Beams entering each window are shown, along with externally mounted coils. Arrows indicate field direction on exterior coils, and current flow in the U and Z-shaped wires. Windows are anti-reflection (AR) coated at 90° incidence for 780 nm (slower axis, y-axis) or 1550 nm (MCP axis, x-axis). The science cell is not AR coated. Not shown in this picture are the coil wound around the bottom flange used for the MOT or the MOT beams entering from the bottom of the chamber at 60° in the x-z plane.

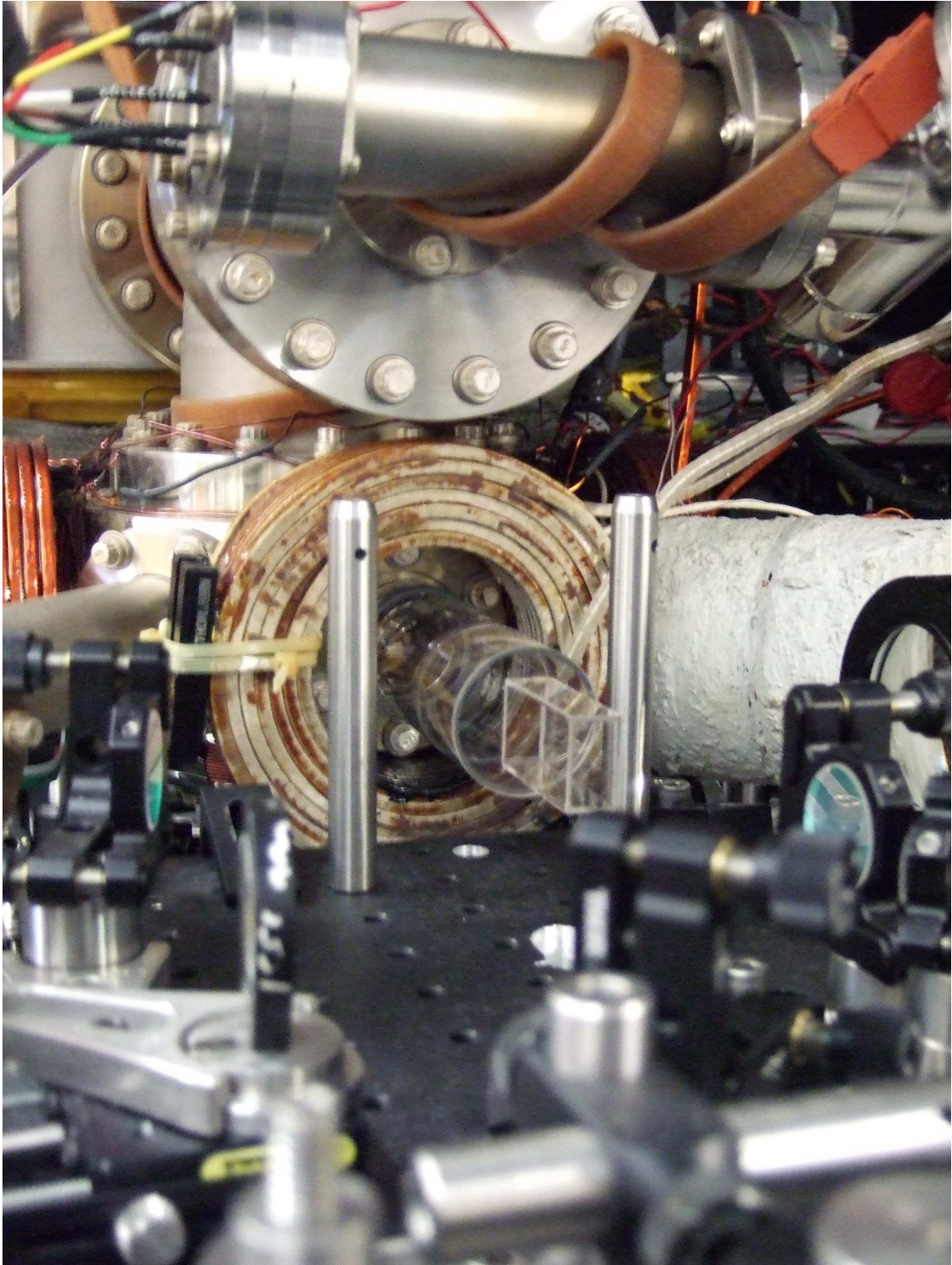


Figure 3.4: Photo of science chamber attached to the main vacuum chamber.

magnetic trap, and 4 leads which were previously used to run current for Rubidium dispensers [55], but which now serve as electrodes used in experiments with Rydberg atoms. In addition, there are two water feedthroughs which feed a stainless steel can attached to a copper block, in turn connected to a piece of aluminum-nitride in which sit the U and Z-shaped wires. Aluminum-nitride was chosen for this purpose because although it is an electrical insulator, it is a good thermal conductor. On top of the wires sits a gold mirror used to reflect MOT beams, held in place by metal clips screwed to the copper block behind the aluminum-nitride. The gold mirror is a silicon wafer coated with gold by the Fab Lab at the University of Maryland and then broken into a 3 cm square.

3.2.2 Rubidium Oven

A schematic of the inside of the Rb oven is shown in Fig. 3.5 and in [55]. An additional picture showing the cold plate, ball valve, and end of the collimator is shown in Fig. 3.6. The Rb sits in a 1-1/3" inch bellows which we use to crush the ampoule that contains the Rb. This hangs from a 1-1/3" "tee" which is connected to a spherical square chamber on one side and blanked off on the other side. The spherical square chamber (2-3/4" on sides, 4-1/2" on the top and bottom) is connected to the tube for the Zeeman slower on the side opposite. The connection on the bottom has both a 3/4" copper feedthrough and a rotary feedthrough; one side is an all-metal valve, one side is a window, and the top is connected to an extender tube and then to a 30 L/s ion pump. The all-metal valve is used to rough out the

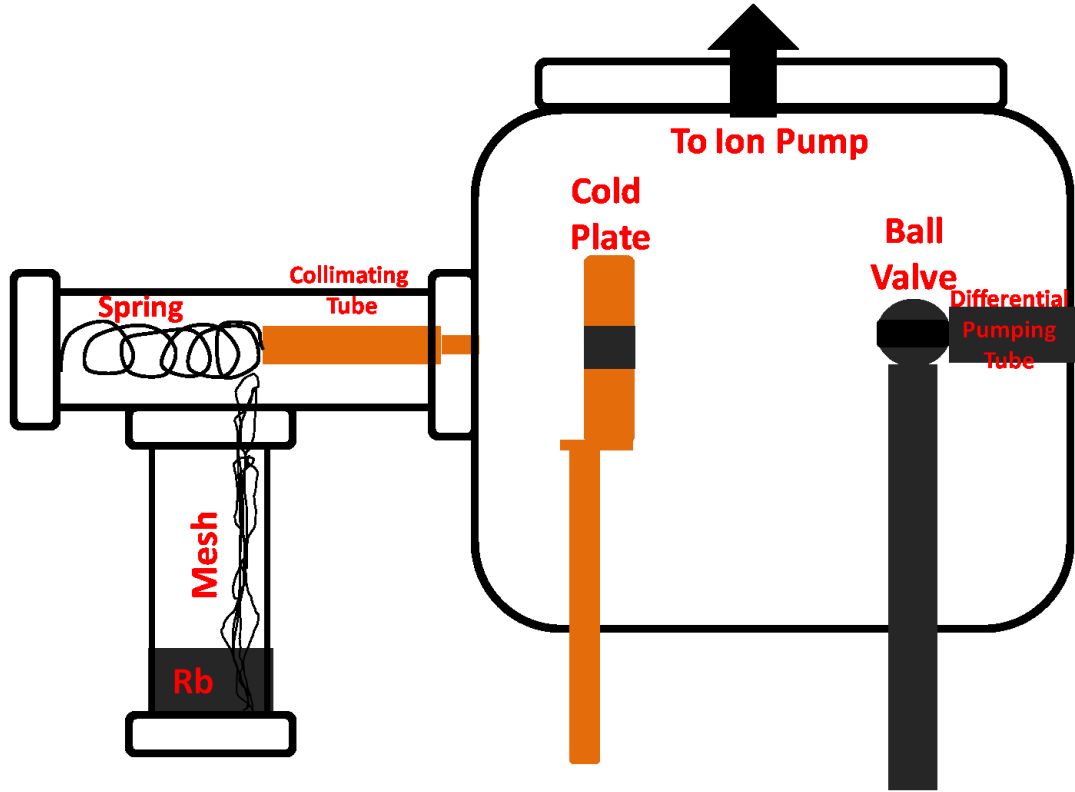


Figure 3.5: Cut-away side view schematic of the Rb oven.

system before turning on the ion pump, and the extender tube is needed to decrease the effect of the fringing magnetic fields from the ion pump.

Inside the bellows, next to the ampoule, we put a gold mesh (gold evaporated on a stainless steel mesh). This is an attempt to mimic the “candlestick source” [148, 79]. Once the ampoule is broken and the bellows is heated, the Rb should turn into a liquid, and the mesh should stick into this liquid and then up out of the bellows into the tee. However, it is unclear whether our mesh serves as a source of atoms from the top of the mesh or recycles atoms back into the pool of Rb. The original candlestick source has two different meshes for each of these purposes. If the mesh is at a higher temperature at the top, then capillary action drives the Rb

up to the top, and the heat at the top drives the atoms off of the mesh, so the top of the mesh acts as a source of hot atoms. However, if the mesh is cooler at the top, atoms can collect there, and then gravity and capillary action can carry them back down the mesh into the pool of Rubidium. According to [79], the reason gold-plated stainless steel is used is that Rb will only wet to stainless steel if the stainless steel is very clean. The process of gold plating seems to electropolish the surface of the stainless steel, making it very clean. The Rb forms an alloy with the gold, effectively removing it, and then wets to the stainless steel. In our case, the oven seems to work with the mesh, so we continue to use it.

Inside the tee sits a tube to collimate the beam of atoms. This is a copper tube, approximately 2 inches long and tapered to two different diameters. The larger diameter, closer to the bellows, serves to sit just interior to the tee to help hold the tube in place. The smaller diameter closer to the chamber serves as the actual collimator. The smaller diameter is about 2 mm inner diameter. The tube is held in place by a spring which pushes from the blank on the back side of the tee. Additionally, the smaller part fits snugly into the gasket holding the tee to the reducer which connects it to the spherical square chamber. The gasket is a copper disc which was drilled out with a 3/8" hole to hold the collimating tube.

Closer to the main chamber, sitting about 2" from the the end of the collimating tube, in the spherical square chamber, is a 3" diameter copper plate with a hole drilled in it. This plate is attached to the copper feedthrough, and we cool the feedthrough to approximately -10° C with a large copper block attached to a thermoelectric cooler (TEC). The back of the TEC is cooled with a Thermaltake

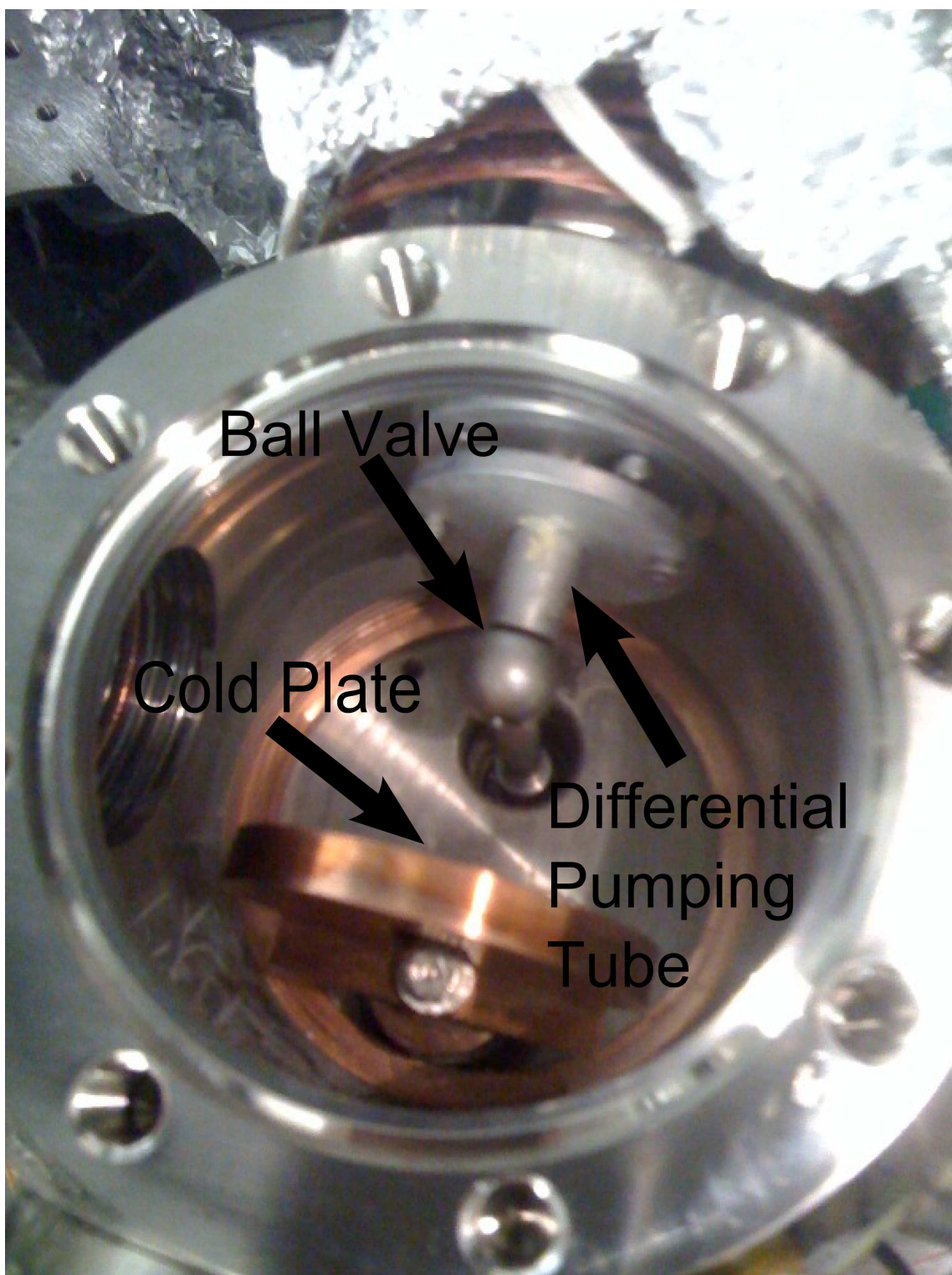


Figure 3.6: View looking down into spherical square chamber just in front of the Rb source.

closed-loop water cooler intended to cool computer processors for overclocking. The plate provides additional collimation for the atomic beam and also catches the Rb which sprays outside the confines of the beam. This is important, as Rb will ruin the ion pump on the source side.

Next, closer to the main chamber and Zeeman slower, is a sphere of 1" diameter with a large hole drilled through the center. This sits just in front of the tube used to maintain the pressure differential between the main chamber and the oven chamber. It is connected to the rotary feedthrough, and it is used to reduce the conductance to the main chamber when we are not actively loading the MOT. The ball rotates so that during the MOT load atoms are free to move through the large opening, but that opening is perpendicular to the pressure differential tube at all other times. The tube to maintain the pressure differential between the oven and the main chamber is the last object between the oven and main chamber. This tube serves to maintain a pressure differential of 2-3 orders of magnitude. Based on the pressure reading in the main chamber, we expect that the pressure in the oven is maintained at a few 10^{-9} Torr.

3.3 Lasers

There are four lasers currently used in the experiment. Two are diode lasers, a Toptica DLX-110 and a Sacher Lynx laser. We also have a Titanium-Sapphire (Tekhnoscan TIS-SF-07) laser pumped by a 10 W 532 nm Coherent Verdi V-10. Finally, we have a 15 W fiber laser (IPG photonics ELR-1567-LP-SF). Both diode

lasers are 780 nm diodes. The Sacher is 100 mW and used for repumping on the MOT and Zeeman slower beams. The Toptica is 500 mW and used for the MOT beams, slower beam, optical pumping, and probe lasers. The Toptica actually has a 1 W diode installed, but because it was refurbished, it still has a low power optical isolator which restricts the output to 500 mW. The Titanium-Sapphire (Ti-Saph) laser is tunable between 750 and 850 nm, outputs approximately 1 Watt of power when fully tuned near its peak wavelength, and is used for optical lattices and the creation of speckle disorder. The fiber laser outputs 15 W at 1563.8 nm and is used for the optical trap. Beam path diagrams for the diode lasers are in Ref. [55], while the fiber laser beam path diagram is in section 3.8, and the Ti-Saph diagram is in chapter 4.

3.3.1 Frequency Stabilization

The two diode lasers have to be frequency stabilized to drive atomic transitions. The frequency width of the laser should be less than the linewidth of the transition that the laser is driving. For ^{87}Rb , the linewidth of the D_2 transition is about 6 MHz [142]. For the trapping laser, the requirement is actually more stringent than that, since measurements are made using absorption of this light by the atomic sample. If the frequency width of the laser is too wide, the absorption will be inconsistent, even with repeated measurements of the same sample. Therefore, this frequency is stabilized to 500 kHz. The requirements on the repumper are less stringent, so a less complicated lock set-up is required.

In order to lock the frequency of a laser, we must generate a voltage signal proportional to the frequency of the laser which switches sign at the frequency at which we want to lock. The output of a feedback circuit can then be used to “push” the frequency back to the desired value by applying a voltage to either the piezo controlling the grating feedback to the laser, or to the diode current, or both. For the Toptica (trapping) laser we feed back to the current, while we apply feedback to the piezo of the Sacher (repumper) laser.

The error signal input to the lock is generated from the trapping laser using a technique similar to Pound-Drever-Hall [23]. An electro-optic modulator (EOM) phase modulates the beam at 14 MHz. This generates frequency sidebands at the driving frequency which are 180° out of phase with one another. When the laser frequency is sitting exactly at the peak of an absorption feature, both sidebands are absorbed equally by symmetric absorption on either side of the peak. However, if the center frequency is changed to the side of the absorption feature, one of the sidebands will be absorbed more than the other, giving an intensity modulation at the sideband frequency. The phase of this modulation will depend on which side of the resonance the center frequency is. This can then be mixed with the driving sideband frequency to give an appropriate locking signal, using the set-up shown in Fig. 3.7. When the phase of the modulation switches, the mixed output voltage switches sign. Electronically, the bias-T directly after the photodiode prevents any DC voltage from going to the sensitive RF amplifier used to amplify the 14 MHz signal. Because there are many higher frequency sidebands generated, the output of the mixer must be filtered to obtain the low-frequency lock signal. This laser is

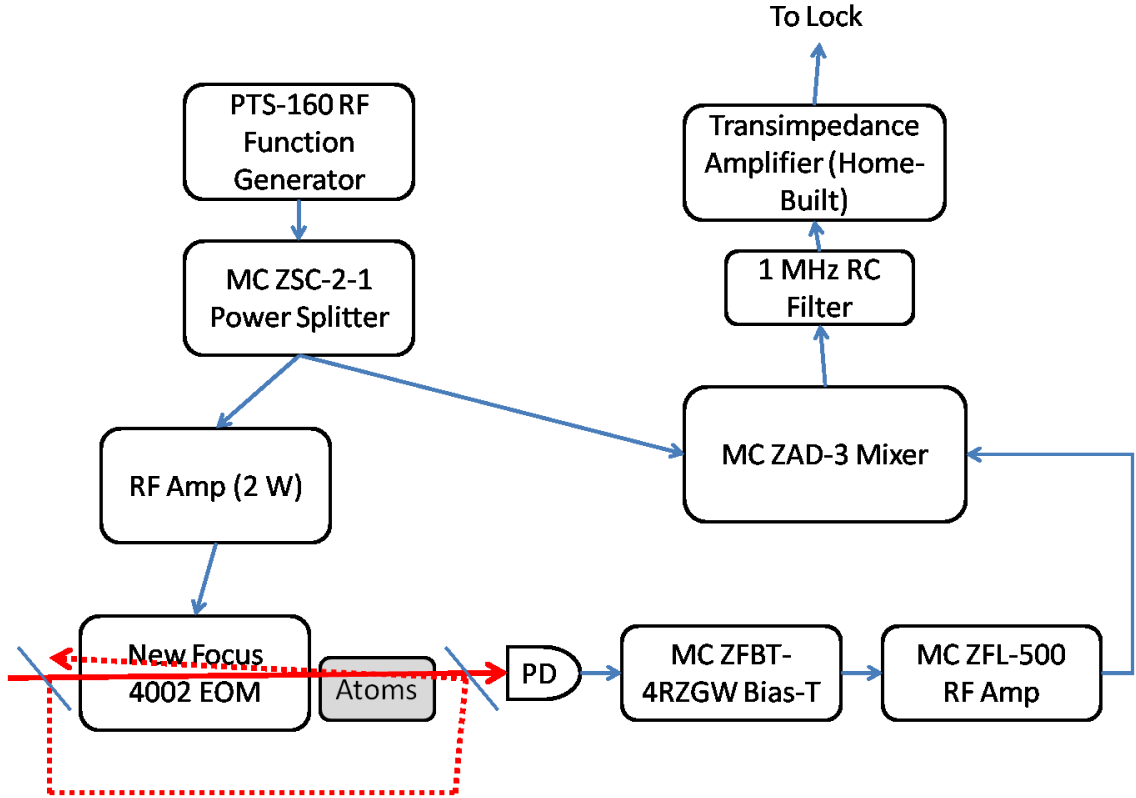


Figure 3.7: Electronics setup to generate error signal used to lock trapping laser. “MC” indicates a Mini-Circuits part. The dotted line is the pump beam used to generate the Doppler-free spectrum of the atomic resonance.

locked with a commercial feedback circuit, the Precision Photonics LB1005 (now sold by Newport). The Doppler-free absorption feature is generated using a saturated absorption technique [103, 50, 51], illustrated by the crossing of the additional strong pump beam (dotted) in Fig. 3.7.

The repumper laser is locked using a DAVLL method [42]. Due to the energy level shift in a magnetic field shown in Fig. 2.2, the resonant frequency for σ^+ polarized light is shifted from that of σ^- in a non-zero magnetic field, since each type of light drives a different transition. A beam with a mixture of the two polarizations is sent through a Rb vapor cell with magnets alongside it. The beam is

subsequently split into its constituent polarizations with a polarizing beam-splitter and then the absorption profile of the two is directed onto two separate photodiodes and electronically subtracted. This gives a zero right in the middle of the absorption feature, where each polarization is absorbed equally, and then an opposite voltage on each side of the feature. Since the absorption spectrum is not Doppler-free in this case, the feature is much wider than the locking signal used on the other laser. In addition, the magnetic field from the magnets used to form the magnetic field in the cell is very sensitive to temperature changes. Therefore, we put the magnets and vapor cell inside a box and stabilize the temperature. We have an additional Doppler-free saturated absorption signal which we use as a frequency reference to adjust the lock point.

Since the other two lasers used in the experiment are far off resonance for the atoms, they do not need to be frequency stabilized. The IPG fiber laser for the optical trap has a linewidth of 5.5 MHz (FWHM). The Ti-Saph comes with an electronic control box which can be used to lock the frequency by dithering a piezo on the thick etalon and feeding back, but we rarely use it.

3.3.2 Intensity Stabilization

The requirements on the intensities of the different lasers are reversed from their frequency requirements. The two diode lasers' intensities do not matter much, while the Ti-Saph and fiber lasers must have their intensities stabilized. For the fiber laser, this is because the depth of the optical trap is directly proportional to the

intensity. When we evaporate in the optical trap, we must be able to precisely control this depth. For the Ti-Saph, many of our measurements require a precise knowledge of the depth of the optical lattices formed by the laser, which are proportional to intensity.

The two different lasers share the same basic lock set-up. A small amount of light from the beam is sampled after either an EOM or an acousto-optic modulator (AOM). This light is used as the input error signal for the lock, and the feedback goes to the AOM or EOM.

There is an EOM in the beam path for the fiber laser which can be used to control the intensity of the light. A voltage across the crystal will change the polarization of the light traveling through the EOM, and a beam cube converts this polarization change to an intensity change. A Thorlabs photodiode is placed behind the mirror directly after this EOM. The leakage light through the mirror is enough to lock the laser, since the photodiodes we use (Thorlabs DET10C) are very sensitive at 1550 nm. The signal from the photodiode goes to a home-built transimpedance amplifier and is used as one input to a Precision Photonics LB1005. The other input to the LB1005 is an analog voltage from the computer control. The output of the lock will feedback to adjust the intensity on the photodiode so that the photodiode output voltage matches the computer control voltage. There is a low-pass RC filter between the computer control and the lockbox. This helps a great deal in preventing noise on the computer control signal from being written onto the intensity of the laser. However, it greatly restricts how fast we can change the intensity of the laser. Meanwhile, the overall bandwidth of the lock is limited to about 200 kHz by the

EOM high voltage controller.

Due to the comparatively lower power involved in the beams from the Ti-Saph (<250 mW per beam), there are fibers used to direct the beams to the experiment. The AOM's used to control the intensity of these beams are placed before the inputs of the fibers, with the first order diffracted beam used as the fiber input. Then, the beam is sampled using either a glass slide or a Thorlabs beam pick-off (BSF10-B). A short focal-length lens is used to focus the sampled beam onto the photodiode (Thorlabs PDA36A). If the beam is small at the pick-off, then the reflections from the front and back surfaces can be separated and a razor blade can be used to block one of the reflections to prevent interference on the photodiode. Feedback from an electronic lockbox adjusts the RF power (with a voltage controlled attenuator, Mini-circuits ZX73-2500+) to the AOM to maintain a constant optical power in the beam after the fiber. One disadvantage to this set-up is the strong thermal beam steering of the AOM. We must be careful to keep the RF power incident on the AOM's constant so that when we want the beam on, it is aligned into the fiber. Otherwise, when the AOM has cooled down, the injection into the fiber will be poor, leading to a low maximum output until the AOM is fully warm. A shutter is in place so that the RF power to the AOM's only has to be off for the time required to open the shutter, on the order of tens of milliseconds.

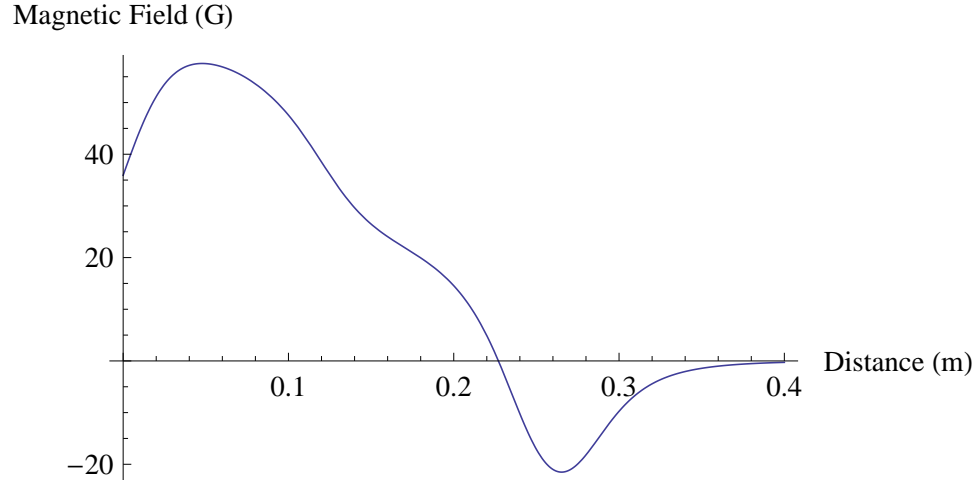


Figure 3.8: Calculated magnetic field profile of the Zeeman slower. The source is at distance zero.

3.4 Zeeman Slower and MOT

The Zeeman slower is designed with 7 separate coils wound on an aluminum tube of 3" diameter. Each coil is 2" wide, and the coils are all wound on the tube butted up against the next coil in line. The first four coils (starting from the source) are two layers of 25 turns of 14 AWG rectangular wire, while coils 5 and 7 are four layers, and coil 6 is six layers. The field at the center of each coil is 27 G/A for each layer on the coil. A calculated field profile for the slower is shown in Fig. 3.8. To drive currents to the coils, a single linear supply is used in conjunction with 7 transistors [55] to divide the current to the separate coils.

The MOT quadrupole field is created by the U-shaped wire shown in Fig. 3.9 with the addition of an external bias field opposing the field from the flat middle section of the U [74, 135, 153]. The fields from the leads cancel each other at the minimum, so that no field is felt from the leads by the atoms. The bias field for the

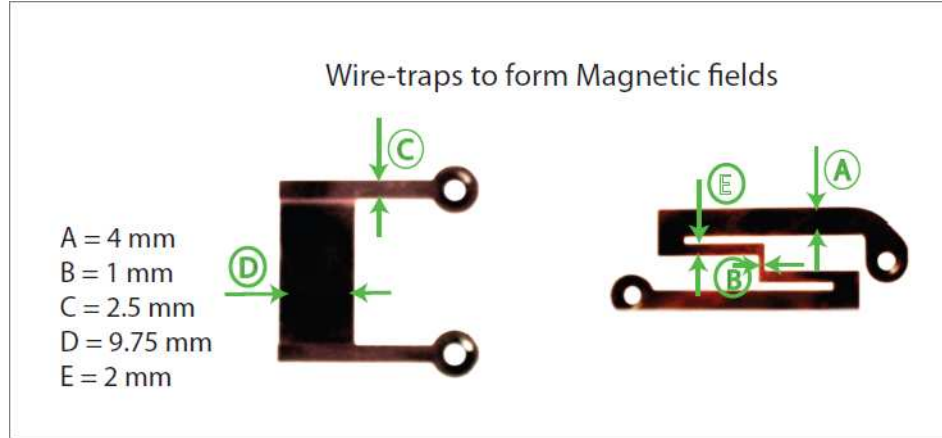


Figure 3.9: Pictures of the wire traps used to form the MOT and magnetic trap (from Ref. [55]).

U-shaped wire is created by two coils external to the chamber wound in Helmholtz-type configuration (“x-bias” in Fig. 3.3). These coils are square shaped hollow wire which create a field of magnitude 0.75 G/A , and we cool them by running water through them [55]. In order to run the water through the coils, short (1”) sections of round copper tubing are soldered (with a blowtorch) to the ends of the wire, and then swagelock connections are made from the copper to plastic tubing. In addition to this bias field, there is also a coil wound directly around the large bottom window of the chamber. This “tilts” the MOT field and facilitates loading of the MOT. The widening of the central bar of the U has a similar purpose.

The U-wire is attached to the vacuum chamber with the structure shown in Fig. 3.2, and on top of it is the gold mirror used for two of the four MOT beams, as shown in Fig. 2.4. These beams enter the vacuum chamber through the large window on the bottom at an angle of approximately 60° from vertical. Because a MOT requires laser light from 6 perpendicular directions, the beams which hit the

mirror have diameters of approximately 1.5", and they hit the atoms both before and after reflecting off of the mirror, providing a mirror MOT [128, 97]. This provides four of the six beams, with the other two coming in perpendicular to the plane of the mirror in two of the windows of the octagon. All four MOT beams come from the four outputs of a fiber splitter, which has four inputs as well. Two of the inputs of the splitter are coupled to all four outputs, while two of the inputs are coupled to only two of the outputs. The repumper light for the MOT is combined onto the two beams incident on the gold mirror using one of the "two-output" ports of the fiber splitter. We typically load for approximately 8-10 seconds, collecting on the order of 10^9 atoms in the MOT.

3.5 Optical Molasses/Optical Pumping

Our optical molasses step occurs just after the MOT step in the experimental sequence. The fields from the coils are extinguished quickly using insulated gate bipolar transistors (IGBT) [55], while the MOT beams are detuned almost five linewidths further from resonance (~ 28 MHz). During this time, it is important to have no magnetic field where the atoms are sitting, as magnetic field causes a drift in $\sigma^+ - \sigma^-$ cooling. In order to zero the field, we have trim coils wound in Helmholtz configuration glued directly to the flanges on the vacuum chamber, including the bottom and top of the chamber. We also have a single coil glued opposite the slower to compensate any stray fields from the slower (Fig. 3.3). This molasses step lasts for about 5 ms, a time long enough to cool the atoms to $40 \mu\text{K}$ while only about

5% of the atoms leave the trapping area.

Just after the optical molasses, we apply an optical pumping pulse to spin-polarize the ensemble. After the MOT and molasses, the spin distribution of the atoms is unknown, although probably close to isotropic. We trap the $F = 2$, $m_F = 2$ spin state, so the light for the optical pumping is tuned from the $F = 2$ ground state to the $F' = 2$ excited state, and the light is σ_+ polarized. Using this combination of frequency and polarization assures us that once an atom is in the desired ground state, it no longer makes resonant transitions. The allowed transition would be to the $F' = 2$, $m_F = 3$ state, which does not exist. This limits heating during the optical pumping pulse. We use a pulse time of 350 - 500 μs with a power of 250 - 350 μW in a beam of 1 cm diameter.

3.6 Magnetic Trap

The magnetic trap that we use is an Ioffe-Pritchard trap (Sec. 2.4) [74, 135, 153]. It is created by the Z-shaped wire shown in Fig. 3.9, which sits on top of the U-wire on the structure in Fig. 3.2, electrically insulated by a sheet of Kapton. As the field from the center wire falls off linearly inversely with the distance from the wire, a uniform bias field cancels the field at a distance r_0 from the wire. The field increases in magnitude radially around r_0 in the plane perpendicular to the center bar of the Z-wire. The same exterior coils used in the MOT form the bias used to define r_0 . The leads of the Z do not compensate one another, unlike for the U, so these leads play the role of the “pinch coils” in a regular Ioffe-Pritchard type trap.

In addition, we have another set of Helmholtz type coils outside the vacuum (0.4 G/A) which enhance the field from the leads and significantly compress the trap.

Because the atoms are not far away from the Z-trap compared to the size of the wire, a calculation of the magnetic field at the atoms must go beyond the thin wire approximation. In order to calculate the trapping frequencies of the magnetic trap, we first find a closed form solution for the magnetic field of a finite length infinitely thin wire. Then, this solution is numerically integrated over the plane of the actual spatial distribution of the entire Z-shaped wire by parameterizing each section's current flow. In order to model the current density in the sharp corners of the wire, the solution is found for all of the current flowing into each corner, and then all of the current flowing out of each corner, and then averaged. Once the field from the wire is calculated, the uniform bias field from the exterior coils is added to the calculation, and a 1D minimum is found as a function of distance from the Z-wire. Typical magnetic traps have a minimum approximately 2-3 mm from the wire. Once the minimum is found, the potential is assumed to be harmonic about the minimum, and the second derivative is calculated in all three dimensions to get trap frequencies. A more advanced solution would use finite element analysis to model the actual current density in the wire, but we get fairly good agreement with experimentally measured trap frequencies using this method. A plot of magnetic trap frequencies versus current in the "pinch" bias coil is given in Fig. 3.10, with the other bias and Z-wire current at 75 Amps.

We load approximately 2×10^8 atoms in a large volume, weakly confining trap for approximately 10 ms, and then immediately compress the trap for 250 ms to its

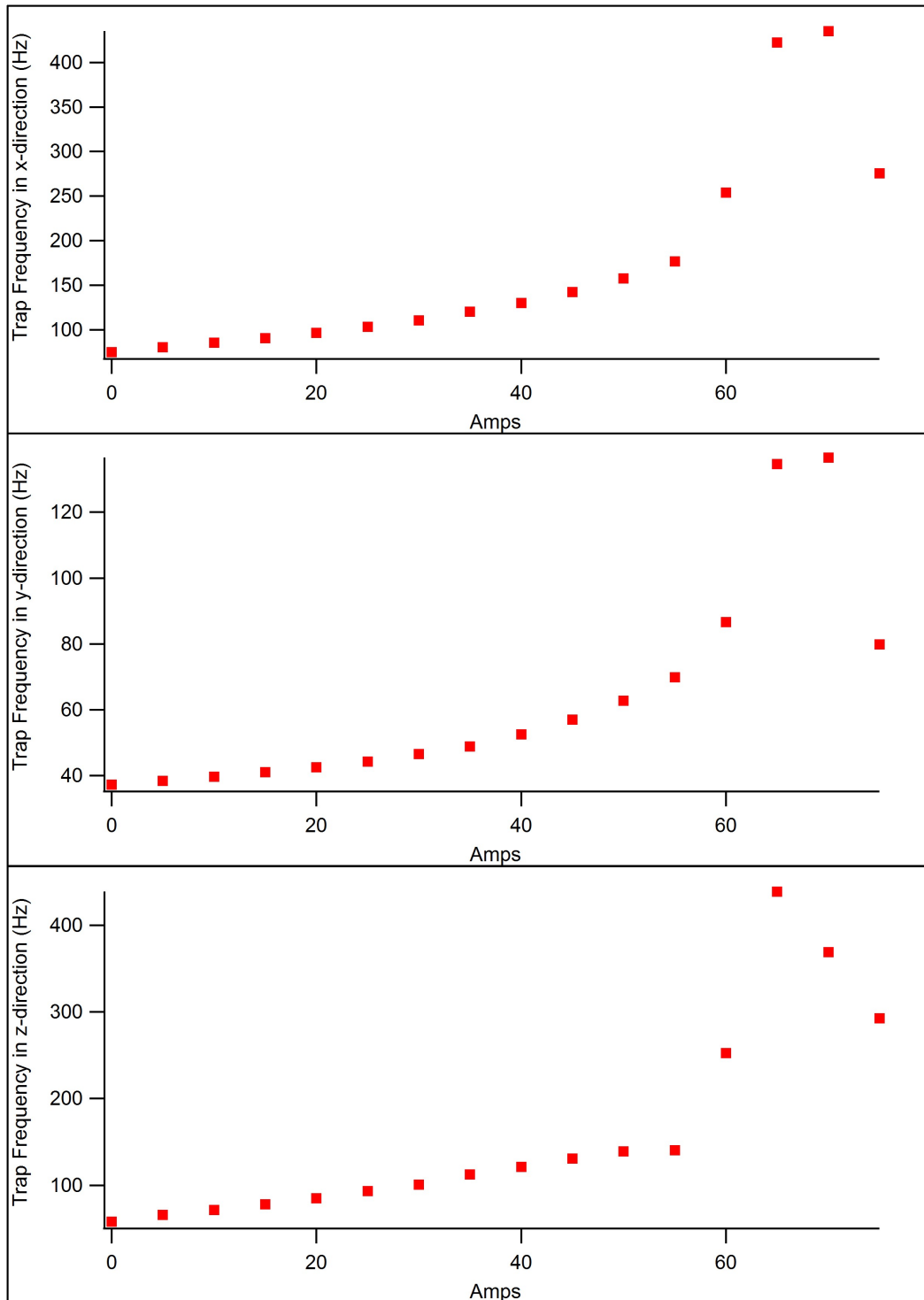


Figure 3.10: Magnetic trap frequencies as a function of “pinch” bias current with other two coils running 75 A.

final value. Because the depth of the trap is set by the bias field opposing the center bar of the Z-wire, the compression, which increases this bias field, serves to deepen the trap as well as tighten it. We typically have trapping frequencies between 100 and 400 Hz in the tight directions of the trap (the plane perpendicular to the center bar of the Z), and 30 to 100 Hz in the loose direction. The highest frequencies correspond to currents of 75 A in the z-wire, 75 A in the bias coils opposing the field from the center bar, and 65 A in the coils supplying bias fields in the same direction of the leads of the z-wire. The temperature of the atoms after compression to this trap is around $500 \mu\text{K}$.

Once the atoms are loaded into the magnetic trap, we can cool them using RF evaporation all the way to BEC, or stop the process at some point in order to load them into an optical trap (Sec. 3.8). The RF coil is approximately 3 turns of wire wound in an oval shape of 4" x 2" . This is placed nearly against the large bottom window of the vacuum chamber, aligned so that the minor axis of the coil sits in between the entering beams for the MOT. The RF function generator controlling the RF sweep is connected to a 4 Watt RF amplifier, and then a BNC cable. The center lead of the BNC cable is then soldered to the wire forming the antenna, and the other side of the antenna is soldered to another BNC cable connected to a 50Ω terminator. The ground braids of the two BNC cables on either side of the antenna are soldered together to close the circuit. The RF frequency sweep goes from about 40 MHz down to frequencies of 1 to 8 MHz, depending on the trapping currents.

Typically, in order to load the atoms into the optical trap, the evaporation in the magnetic trap is stopped and the atoms are decompressed to a trap with

frequencies of 115×65 Hz in a 250 ms linear ramp of the currents to 55 A (z-wire), 75 A (center bar bias), and 40 A (z-wire lead bias).

3.7 Power Supplies and Grounding

The supplies which run the MOT and magnetic trap are Sorenson DLM-600 model supplies. The bottom coil for the MOT is run by a Sorenson XLT-60 supply, and the trim coils used in the optical molasses are run by Kepco ATE15-3 supplies. There is an interlock circuit to keep the water-cooled coils (including the U and Z wire) from being run without the water cooling, and IGBTs are used to turn off the coils quickly for expansion measurements of the atoms [55].

The initial ramp of the power supplies is also critical to capturing atoms in the magnetic trap. Since the IGBT's are not part of the servo loop which controls the current output of the supplies, it is possible to get transients when switching the supplies on. If the supplies are being commanded to drive any amount of current while the IGBT's are preventing current from running, the supplies will then rail at their maximum voltage as they try to drive current to the open loop. As soon as the circuit closes, this voltage will cause a spike in current before the supply can effectively feed back to manage the current. In fact, even if the supply has been commanded to a value of 0 or less than 0, there will be a delay before the feedback starts once the supply is commanded to switch to some positive voltage. Therefore, to get a linear ramp of current when the supplies turn on, the timing control of the analog voltage to the supplies running current during the magnetic trap must

be such that the commanded current is less than zero during the MOT, and then driven positive for a time on the order of 10's of ms before the ramp is to start. This ensures a linear turn-on of the magnetic fields for the magnetic trap.

Ground loops are a large problem for any magnetic trap. If there is any resistance between the grounds of supplies, there can be a beating due to the phase difference of the 60 Hz power input to the DC power supply. This beating gives us current noise on our supplies at 60 Hz, a frequency slow enough for the atoms to respond to, especially if any of the trapping frequencies are near 60 Hz or a harmonic of 60 Hz. To mitigate this, we tie all of the grounds of our Sorenson supplies to the optical table using AWG 6 wire. The optical table, in turn, is connected to both the ground of one of the wall circuits via a grounding braid and also tied to a large pipe running across the ceiling of the lab. The wire running to the pipe is AWG 1/0, and another wire of this type is run to the 19" rack which we use to break out all of our computer control (Sec. 3.10.1).

In addition, to prevent 60 Hz noise on the analog inputs which control the current output of the supplies, we use a USB to optical converter which breaks the ground connection to the computer control (Icron USB 2.0 Ranger 442) for our USB DAQ card (NI USB-6229). One further step to eliminate 60 Hz noise is that digitally triggerable low pass filters are placed between the USB DAQ card and the power supplies. These can be turned on once the magnetic trap cycle has started. If they are turned on too early, they limit the bandwidth of the control signals to the power supplies. Despite all of these precautions, there is still a trap frequency dependent heating rate (~ 100 nK) which we attribute to magnetic field noise, although it did

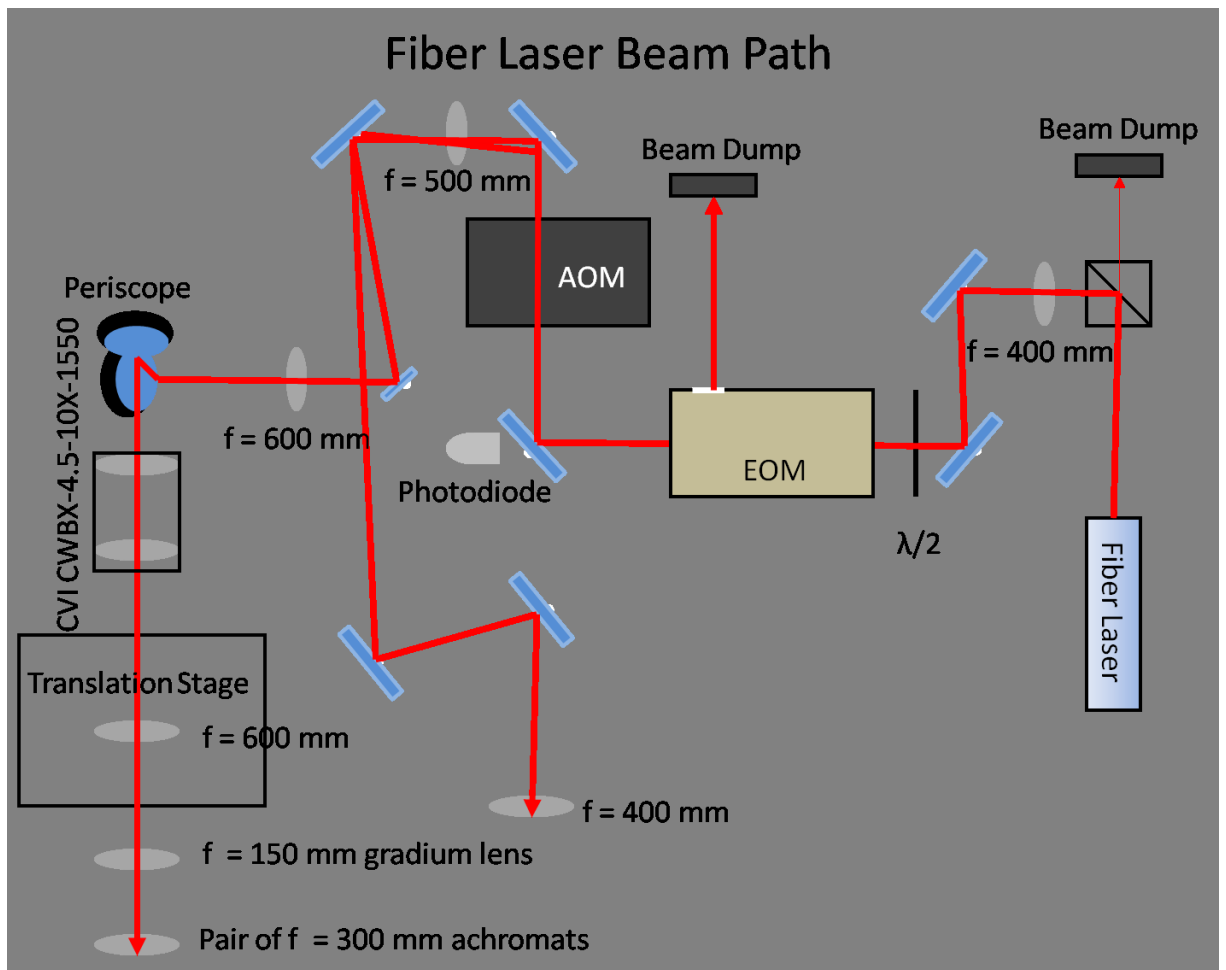


Figure 3.11: Optics and optical path for control and shaping of the 1550 nm optical dipole trap.

seem to be lessened by these changes when we made them.

3.8 Optical Trap

The beam path for the optical trap is shown in Fig. 3.11. A beam cube is used to purify the polarization of the beam before it goes through the EOM used to lock the intensity, and an AOM is used to split the beam power to be used for a crossed dipole trap in the cell. The main beam used for the optical tweezer passes through

a telescope which expands the beam, and then through an $f = 600$ mm focusing lens on a translation stage. The beam is then relay imaged to the atoms in the chamber. Meanwhile, the cross beam passes through a lens to expand it, and then through a focusing lens of $f = 20$ cm, set on a translation stage, before crossing the tweezer beam in the science chamber.

For most optical traps, it is beneficial to have a small beam waist. This increases the trapping frequencies, giving a large collision rate and tight confinement. For our setup, there is approximately 30 cm between the end of the quartz cell science chamber and the position of the atoms during the initial transfer to the optical trap. Since the beam must travel through the end of the cell before hitting the atoms, it must be smaller than the smallest dimension of the cell face (1 cm) in order to pass into the chamber with a minimum amount of diffraction. A Gaussian beam waist $w(z)$ expands along its axis z as

$$w(z) = w_0 \sqrt{1 + \left(\frac{z}{z_R}\right)^2}, \quad (3.1)$$

with $z_R = \frac{\pi w_0^2}{\lambda}$ the Raleigh range, and w_0 the waist of the beam at its smallest point. This equation shows that a more tightly focused beam diverges faster, which sets a minimum waist size of $40 \mu\text{m}$ for our tweezer beam.

In addition, when we initially set up the optical trap, diffraction was a problem all along the beam path. We were not careful to follow the general rule that the diameter of any aperture for a beam should be four times the beam waist to prevent diffraction [81]. When a beam diffracts from a circular aperture, the size of the

waist of the beam doesn't change much, but power is redistributed to the wings of the intensity distribution. We spent a good deal of time measuring beam waists using a razor blade on a translation stage, always coming up with waists which were pretty close to what we expected. However, the measured trapping frequencies of our optical trap (dependent only on intensity and wavelength) were much lower than we expected. Characterization of the beam profile is hampered by the fact that CCD cameras (and Silicon photodiodes) are not sensitive at 1550 nm. So, it turns out that the razor blade and translation stage method for measuring beam waists that we were using did not have the spatial resolution to see the deformation of the beam due to diffraction. We finally discovered the problem after modeling the system in Oslo optical design software, and then measuring the intensity profile using a 2 μm pinhole translated with a New Focus Picomotor.

The first problem with diffraction is that the aperture diameter on the EOM is only 2.7 mm. However, the damage threshold for the crystal is 500 W/cm^2 . In order to avoid diffraction, we focus the beam through the EOM, and the intensity is 3000 W/cm^2 - well above the damage threshold for the crystal. A discussion with Con-Optics revealed that the damage threshold is very conservative, and that as long as there were no fast temporal changes in beam power, causing large thermal gradients, the crystal would probably not crack. After that problem was solved, the focusing lens for the optical trap was changed from 1" diameter to 2" diameter. The relay optics were also an issue, as the beam waist at each lens changes as the stage moves. The beam waist is much larger at the second relay optic, meaning that this optic has to be larger than the first one. The final solution uses a Gadium

lens (Lightpath GPX40-150) for the first optic and a pair of $f = 300$ mm, $D = 50.4$ mm achromat lenses for the second relay optic. The first optic cannot be a typical achromat because the waist of the beam gets very small when the stage is near its back position. Typical achromats are held together with glue, so they are damaged by high-intensity beams. The second relay optic never sees a high intensity. Paired achromats are used for the second relay optic because achromat lenses are designed to focus a collimated beam to a point. Pairing two $f = 300$ mm lenses allows us to image the focus of the beam while still using each lens to focus a collimated beam. The system was modeled in Oslo with the exception of the Gadium lens, which did not have an Oslo-compatible lens file. The company uses Zeemax for optical modeling, and Oslo was unable to open the Zeemax files.

The main goal of the optical trap is to produce a BEC in the science chamber. Intuitively, the easiest way to accomplish this would be to transfer a BEC from the magnetic trap into the optical trap and then transport it to the science chamber. In practice, there is large amount of heating ($6-8 \mu\text{K}$) in the transfer from the magnetic trap to the optical trap, making this scheme an impossibility. Instead, after some RF evaporation, a $22 \mu\text{K}$ thermal sample of 2.5×10^7 atoms is transferred from the magnetic trap to the optical tweezers, with 25% transfer efficiency, giving 5×10^6 atoms at $10 \mu\text{K}$ in the optical trap.

The efficiency of the transfer is optimized with slow changes in the two traps. After evaporation in a relatively tight magnetic trap ($400 \text{ Hz} \times 110 \text{ Hz}$), the magnetic trap is decompressed to a trap with frequencies $115 \times 65 \text{ Hz}$. This serves to both move the magnetic trap farther from the surface of the gold mirror used to form

the MOT and also to adiabatically cool the atoms. Since the limiting factor in the transfer between the two traps is the depth of the optical trap, the transfer can be made more efficient with this adiabatic cooling prior to transfer to the optical trap. The optical trap is linearly ramped up to half power in 250 ms after the magnetic trap decompression, and then ramped to full power while the magnetic trap currents are linearly ramped to zero in 1.5 seconds.

The oscillation frequencies in the tweezer beam are 1000 Hz and 6.5 Hz in the radial and axial directions, respectively. These were measured with observation of dipole (axial) and quadrupole (radial) mode oscillations [46, 89]. To excite the dipole mode along the axis of the optical trap, the waist of the trapping beam is offset 2.5 mm from the position of the magnetic trap. After the atoms are transferred from the magnetic trap, their position will oscillate about the waist of the optical trap. This oscillation occurs at the frequency of the trap in that dimension. To measure the radial trapping frequency, a quadrupole mode (breathing) oscillation is excited by snapping off the optical trapping potential for 500 μ s and then turning it back on. After a variable hold time, the cloud is imaged after 5 ms of time-of-flight expansion, and the radial size oscillates at twice the trapping frequency.

A calculation for the trapping frequencies of the tweezer beam as function of power and waist for our wavelength (1567 nm) including the effect of gravity and the counter-rotating term yields [72]

$$\omega_r = 2.98 * 10^{-6} \sqrt{\frac{8P}{\pi w^4}} \quad (3.2a)$$

$$\omega_z = 2.98 * 10^{-6} \sqrt{\frac{3.17 * 10^{-13} P}{w^6}}, \quad (3.2b)$$

where ω_r is the radial trapping frequency, ω_z is the axial trapping frequency, P is the power in the beam, and w is the Gaussian waist of the beam, with all quantities in SI units. It is evident from these equations that an estimate for the waist of the beam is given by

$$w = \frac{\omega_r}{\omega_z} * 3.53 * 10^{-7} \quad (3.3)$$

This is an easy way to find the waist of the beam once the trapping frequencies are measured.

With the crossing beam on (described later), the trapping frequencies become a function of the powers and waists of both beams, as well as the crossing angle between them in the $x - z$ plane. Taking the second derivative of the total trapping potential at the potential minimum for each of the original axes of the tweezer trap gives an indication of the trapping frequencies. Once the cross beam is added, the eigenaxes of the trap rotate, but a rough estimation of the trapping frequencies can still be obtained by considering the old eigenaxes. These frequencies are given by

$$\omega_x = 1.13 * 10^{-18} \sqrt{\frac{8P_1}{\pi w_1^4} + \frac{8P_2 \text{Cos}(\theta)^2}{\pi w_2^4} + \frac{3.17 * 10^{-13} P_2 \text{Sin}(\theta)^2}{w_2^6}} \quad (3.4a)$$

$$\omega_y = 2.98 * 10^{-6} \sqrt{\frac{8P_1}{\pi w_1^4} + \frac{8P_2}{\pi w_2^4}} \quad (3.4b)$$

$$\omega_z = 2.98 * 10^{-6} \sqrt{\frac{3.17 * 10^{-13} P_1}{w_1^6} + \frac{3.17 * 10^{-13} P_2 \text{Cos}(\theta)^2}{w_2^6} + \frac{8P_2 \text{Sin}(\theta)^2}{\pi w_2^4}}, \quad (3.4c)$$

with ω_y the frequency in the direction of gravity, ω_z the frequency along the original axial direction of the tweezer beam, and ω_x the frequency in the direction orthogonal

to the other two directions. The subscripts 1 and 2 refer to each of the two beams, and θ is the crossing angle between the two beams, and again all units are SI.

The $1/e$ lifetime of the atoms in the optical trap is estimated to be 10 seconds, based on holding in the trap after loading. This is not exactly the lifetime. Trap heating also causes atom loss, as the initial temperature of the atoms corresponds to an energy near to the maximum confineable energy. However, 10 seconds is also the lifetime measured after evaporation in the cross-beam optical trap. This lifetime is shorter than the lifetime of the magnetic trap, indicating that it is not vacuum-limited [134]. For a period of time, we found that the lifetime of the atoms in the optical trap was 3 seconds when the atoms were in the science cell. This was caused by diffuse scattered near-resonant light, which we remedied by enclosing all of the trapping and cooling lasers in black boxes, with shutters to keep all scattered light inside the boxes. This scattered light was enough to effect the atoms despite the fact that there were no beams visible near the chamber even while looking through an IR viewer with all of the room lights off.

Once the atoms are loaded into the optical trap, an air-bearing translation stage (Aerotek ABL20040-10-LT40AS-NC) is used to translate an $f = 600$ mm focusing lens to translate the waist of the beam. For an appropriate velocity profile (Sec. 3.10.2), the atoms will follow the focus of the beam a distance of 30 cm to the quartz science cell chamber. The entire movement can be done with 90% transfer efficiency in as little as 1.5 seconds. We typically use a time of approximately two seconds. The stage only checks for a trigger signal every 100 ms, and so the timing of the movement is synchronized with the rest of the experimental cycle only to 100

ms. Since the experimental cycle is 30 seconds, this is a small perturbation which can be handled by allowing a little bit of extra time in the timing step controlling the movement.

With the atoms in the science cell, we need to perform further evaporation to reach quantum degeneracy. Since the collision rate in the single beam alone is insufficient to evaporatively cool the atoms efficiently, a second crossing beam is used to increase the collision rate by greatly increasing the trapping frequency (originally 6.5 Hz) along the axis of the original beam. The naive approach to increasing this frequency is to overlap the other beam at a perpendicular crossing angle, overlapping the strongest confining direction of each beam with the weakest confinement of the other beam. However, for the power we have available, the volume and depth of the crossed trap is insufficient to load a significant number of the atoms into the overlap region. This is probably due to the large spatial extent (3 mm) of the atoms along the axis of the first beam when the cross beam is turned on. A simple classical calculation of the dynamics of the cross loading reveals that the maximum temperature of an atom captured in the cross-beam trap can be greatly increased by decreasing the crossing angle between the two beams. We currently use an angle of 16.9° between the beams, bringing the cross beam in through the edge of the same face of the science cell as the tweezer beam. At full power, the cross-beam trap has frequencies of 950 X 950 X 200 Hz.

Finally, we have to be very careful to turn off the optical trap cleanly. Ideally, we would like all of the trapping potentials to turn off in a time short compared to the atoms' movement, which means we would like to turn off the beams in about

10 μs . There are multiple hurdles to overcome in our system. First, the intensity stabilization has a 60 Hz filter on the input control, meaning that the light intensity cannot be changed faster than about 16 ms with the analog control from the computer. In addition, the EOM only has an extinction ratio of 100:1, which means that there is still an appreciable amount of light incident on the atoms even when the EOM is turning the beam “off”. The cross beam can be turned off very fast independently of the tweezer beam by simply turning off the AOM, but we do not want to kick the atoms by deforming the potential before it is turned off. A shutter can be used to fully extinguish the beams, but shutters are typically slow, on the order of 100’s of μs .

We use a combination of EOM, AOM, and a shutter to entirely extinguish the optical trap. A digital multiplexer (Analog Devices ADG201HSJNZ) is placed at the output of the intensity stabilization feedback to the EOM high-voltage controller. This can be used to quickly switch the EOM voltage to its minimum output value. A shutter is placed at an intermediate focus of the tweezer beam between the two relay optics. Because the beam is small there, and for a set shutter speed a smaller beam is turned off faster, it can be extinguished in 125 μs . The EOM is switched off in less than 10 μs just before the shutter enters the beam, and then the AOM is switched off (dumping all of the power into the shutter) midway during the closing of the shutter. The shutter is a 0.5” mirror glued to the arm of a disassembled laptop hard drive [104, 136]. The mirror directs the beam to a beam dump.

3.9 Data Collection (Imaging)

Acquisition of data in this experiment is always done through absorption imaging, usually after a significant amount of free expansion of the atoms. Absorption imaging works on the principle of Beer's law for the amount light absorbed by the sample:

$$I(x, y) = I_0(x, y)e^{-\sigma_A \int n(x, y, z) dz}. \quad (3.5)$$

Here, $I(x, y)$ is the observed intensity of the light after the sample, $I_0(x, y)$ is the light intensity incident on the sample, σ_A is the absorption coefficient of the atoms, $n(x, y, z)$ is the density of the sample, and the probe beam illuminating the atoms is presumed to travel along the z-axis. By taking two images, one with the atoms and one without the atoms, and then dividing the two images and taking the log of the result, the optical depth (*O.D.*) can be recovered:

$$O.D.(x, y) = \sigma_A \int n(x, y, z) dz. \quad (3.6)$$

Obviously, determination of the correct optical depth requires knowledge of the absorption coefficient σ_A for a two level atom:

$$\sigma_A = \left(\frac{3}{2}\right) \left(\frac{\lambda^2}{2\pi(1 + \frac{I}{I_{sat}} + 4\Delta)}\right), \quad (3.7)$$

where λ is the wavelength of the probe light, I is the intensity of the probe, I_{sat} is the saturation intensity of the atoms (3.58 mW/cm² for isotropically polarized light on the D₂ transition in ⁸⁷Rb), and Δ is the detuning of the atoms from atomic resonance. The factor of $\frac{3}{2}$ in front of the expression changes depending on the polarization of the light illuminating the sample, and is used to adapt the expression

to a multi-level atom. Assuming linearly polarized light and doing an approximate optical pumping calculation for the atoms yields a factor of $\frac{3}{2}$, while circularly polarized light gives a factor of 3 [65]. Most of the time, we work in the limit of low saturation intensity and on resonance, which makes the denominator in Eq. 3.7 particularly simple, and has the additional advantage of eliminating any positional dependence of σ_A from the calculation of optical depth in Eq. 3.6. The resulting signal used in all of our analysis (Sec. 3.10.2) allows us to determine the 2D density of the atoms after integration over the direction of probe beam propagation.

One technical detail which is very important in the above analysis involves the determination of $I_0(x, y)$. We desire to know the intensity of the probe beam exactly as seen by the atoms. The way this is typically done is to get rid of the atoms and then take another picture of the probe beam alone, under the assumption that the condition of the probe beam will be exactly the same during this second picture as it was for the first picture. However, invariably, there are fringes and distortions in the probe beam intensity, and if any of the optics move or the intensity of the beam drifts slightly between the two pictures, these features are written onto the optical depth, causing noise in the image. The most effective method to eliminate this noise is to make sure that the two images are taken very close together in time. The limiting factor here is almost always the camera frame rate, although there are certain cameras which have modes allowing multiple images to be taken with small delays.

One promising method to help eliminate this type of noise is called “principal component analysis” (PCA) [137, 105]. I first heard about this technique from Dr.

Ian Spielman. Basically, the idea is that if we were to take a large number of images of the probe beam, we would see all of the different permutations of the possible fringe patterns that could come about. Then, we can think of each image as a set of pixels which we could easily arrange into a vector. The set of all of these background “vectors” can then be diagonalized. Since the original vectors were most likely degenerate, a much smaller subset of these new basis vectors represents most of the information from the entire set. So, if we now take an image with atoms, we can project that image (minus the small area occupied by the atoms) onto this basis set. This projected image becomes the new “background” image used in the division to obtain the $O.D.$ If the basis set truly contains the information available from all of the background images, this can make for much cleaner looking data. One caveat is that the number of images it is necessary to keep in the basis set to obtain all of the information is not precisely defined, so it is difficult to quantify errors from the truncation of the basis set.

Once these issues are minimized, characterization of a general imaging system is complicated by the choice of metrics to use in the characterization, and an imaging system for absorption imaging is perhaps even worse. Typically, we can look at the modulation transfer function or point spread function as an indication of how good an imaging system is. These are still considerations in absorption imaging. We would like to form an image of the density distribution, and the resolution we have in that image is limited by camera pixel size ($\sim 5 \mu\text{m}$) and the numerical aperture of the imaging system. The fact that the atoms are in vacuum means that the window of the vacuum system is also part of the imaging system, so the window must be

considered when attempting to image with high resolution. However, we must also consider the finite depth of the object, which limits the imaging resolution to $\sim 7 \mu\text{m}$ for a BEC of $50 \mu\text{m}$ extent along the axis of the beam [29].

In addition, the imaging system in absorption imaging must take into account the rays from the probe beam which are unaffected by the atoms, as well as those rays which propagate through the atoms. An easily-understandable approach to the process of absorption imaging (taken roughly from Ref. [146]) is that we have a plane wave represented as parallel rays impinging on the atoms. As these rays pass through the atoms, pure absorption does not deflect them unless the density starts to vary on wavelength-size scales. Therefore, after passing through the object, each ray is undeflected, but has been absorbed differently depending on where it went through the cloud. Each of these rays starts to diffract after the object, and we can now propagate them using the Helmholtz wave equation in free space, starting with the initial condition of the wavefront having an amplitude inversely proportional to the density of the atoms. However, we must pay attention to make sure that the rays passing on either side of the atoms do not end up on our detector in the position of the atoms, a situation which can easily occur while recreating the object using a combination of lenses.

Our solution here is to use a “4f” imaging system. We place the object at the focus f_1 of the first lens, then place a second lens at the sum of the two focal lengths $f_1 + f_2$ of the lens, followed by a camera at the back focus f_2 of the second lens. This set-up has the advantage that it images both a plane wave and the object, thus preventing the problem of the probe light getting imaged onto the wrong place on the

camera. The magnification M of the system is simply given by the ratio f_2/f_1 . In our system, the imaging set-ups on the magnetic trap and the horizontal imaging in the science cell use $f_1 = f_2 = 100$ mm to give $M = 1$, while the vertical imaging in the cell uses $f_1 = 50$ mm and $f_2 = 100$ mm to give $M = 2$. In order to calibrate the magnification of the horizontal imaging systems, we plot the position of the freely falling atoms after release from the trap, which should be a parabola determined by gravity. To calibrate the value of M in the vertical direction, we compare the size of the cloud on that camera to the size of the cloud on the horizontal camera.

Finally, we must be careful to calibrate the optical depth of the atoms, total counts, and actual intensity of the probe beam at the atoms. If the optical depth of the atoms gets too high, then the probe beam can be fully absorbed, giving large fluctuations in $O.D.$ with only a few counts of noise on a pixel. The greatest $O.D.$ which can be measured is thus limited by the dynamic range of the camera, which is $2^{12} = 4096$ counts in our case. We can always increase this dynamic range to that limit by either increasing the length of the probe pulse or increasing the intensity of the probe beam. However, we would like find a good regime where the pulse time is not too long that the atoms move during the pulse ($< 250 \mu\text{s}$), the intensity is still much less than I_{sat} , but we get a large number of counts on each pixel without saturating it. In our case, a pulse time of $150 \mu\text{s}$ with a $\sim 150 \mu\text{W}$ beam of a few mm waist fulfills these conditions. Still, in most cases of BEC, the $O.D.$ of the cloud should be kept < 2 , which can be done with free expansion of the cloud or detuning of the probe. However, detuning of the probe can introduce refraction in the cloud, which makes analysis more difficult.

There are also a few alternatives to using absorption imaging. All of these methods rely on the fact that the atoms phase-shift light if the probe is not exactly on resonance, and they work in the limit of very low absorption. By making some assumptions, we can recreate the initial density of the object by either interfering it with a phase reference or computationally determining what the diffraction pattern means. Examples of these methods include phase contrast imaging [7], polarization contrast imaging [27], or defocus-contrast imaging (DCI) [146, 147]. These techniques have two advantages. First, because the absorption is small, there is no need to worry if the density of the cloud is too high. Second, the techniques are somewhat non-destructive, since the probe light is far off resonance. This allows for multiple pictures of the same sample, an impossibility with absorption imaging. The major disadvantage of these techniques is that they are more difficult to implement and use.

We have implemented the software to do DCI in our experiment, but have not really tested it yet (Sec. 3.10.2). This technique is actually fairly easy to setup, as it only requires defocussing the imaging system and detuning the probe beam from resonance. The basic idea is that with these changes, we take two images just like in absorption imaging. However, the image of the atoms in this case will look like a diffraction pattern. If we know exactly how detuned we are and how far the camera is defocused, an algorithm can be implemented to recover the original 2D density of the atoms, similar to absorption imaging. The disadvantage to using this type of imaging is that it is strongly dependent on the distance of the camera from true focus, which is a free parameter in the algorithm, so it is difficult to quantify errors.

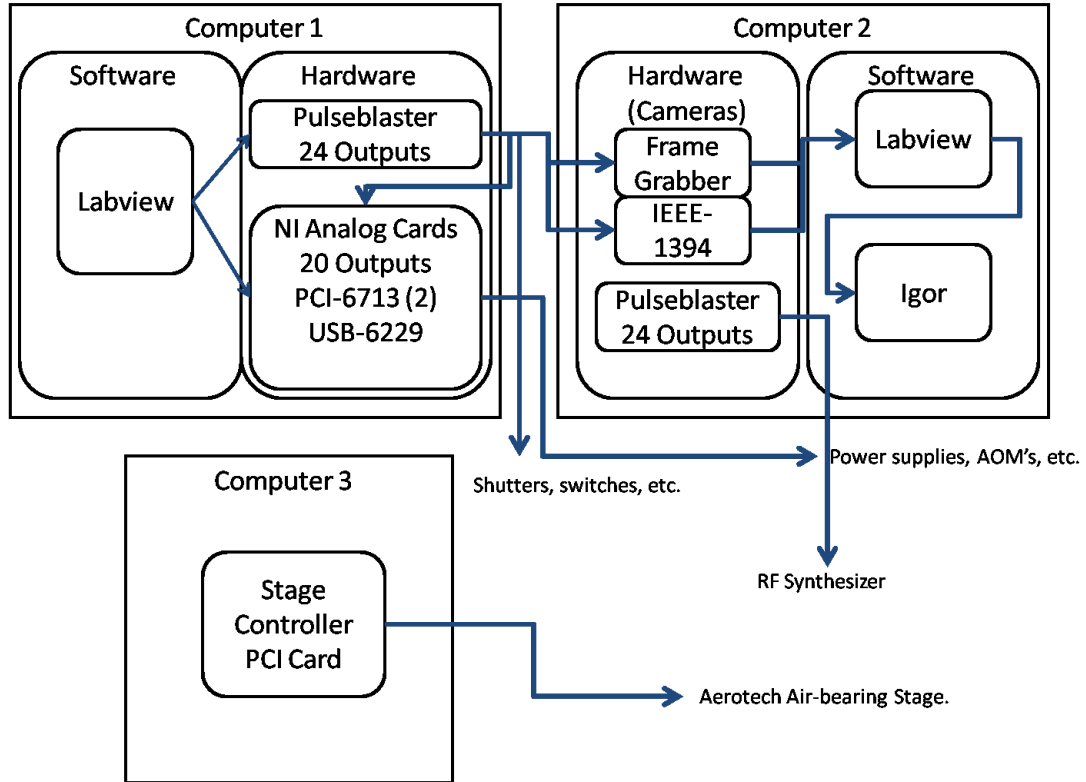


Figure 3.12: Diagram showing the hardware and software control setup for the experiment.

3.10 Control and Analysis

3.10.1 Hardware

A schematic of the computer hardware and software control system is shown in Fig. 3.12. Three computers are used for this purpose, although “computer #3” is dedicated solely to controlling the translation stage used to transport the atoms to the science cell. “Computer #1” is dedicated to hardware control, containing almost all of the digital and analog output channels used to control the equipment, while “computer #2” is used mainly for data acquisition and analysis, except that it also controls the RF evaporation.

The main experimental timing is controlled by a Pulseblaster PB24-100-PCI-512 in computer #1. The Pulseblaster is a digital output card with 24 channels which has a 100 MHz clock with a resolution of 10 ns and a minimum pulse time of 50 ns (5 clock cycles), as well as an on-board memory of 512 lines. The timing of everything in the experiment is synchronized to this card (Table A.1).

One digital line from the pulseblaster is used to trigger the analog output cards in order to generate analog control signals to different pieces of equipment (Table A.2). The digital lines control anything that only takes on two different states during the cycle (such as a shutter), while the analog outputs control any piece of equipment which needs to take on a continuous range of states (e.g., coils producing magnetic fields). Two 19" rack panel BNC boards break out all of the digital and analog outputs (except the four channels from the USB card), and BNC cables are run to the equipment in the apparatus.

There are three different analog output cards. Two are NI PCI-6713 analog output cards, and one is a NI USB-6229. The two PCI cards are in computer #1, and the USB card is connected to computer #1 through an optical link, as described in Section 3.7. This gives a total of twenty analog outputs - each of the PCI cards has eight, while the USB card has four. We use the four from the USB card to control the most noise-sensitive pieces of equipment in the experiment - the magnetic trap coils and the intensity of the optical dipole trap. Because the analog channels do not have enough output current to drive a 50Ω load, each channel is first run through a current buffer (Analog Devices BUF634P) before the 19" rack panel board.

Computer #2 controls both the RF evaporation cycle and the cameras. A

second Pulseblaster (PB24-50-PCI-32K-SP2) occupies a PCI slot in this computer. It is different from the pulseblaster card in computer #1 in that it has a slower clock (50 MHz) and more on board memory, up to 32000 steps. In addition, the wiring of the internal header pin outputs are different, and the windows drivers are different (indicated by the SP2 designation). This card is used to drive a frequency synthesizer (PTS-160) that controls the RF evaporation sequence in the magnetic trap. The function driver takes four digital bits per digit of frequency resolution, with the binary value of the four bits controlling which value that digit has. The binary value has to be between 0 and 9. The only exception is the “ten MHz” digit, which can go to 10 to represent 100 MHz. The RF frequency scan is preloaded into the Pulseblaster (which can take up to 20 seconds) so that a digital trigger from computer #1 can simply trigger the scan at the appropriate time in the experimental cycle. A glitch in the particular Pulseblaster card running the RF synthesizer requires that a second digital signal be sent to the “hardware reset” bit on this Pulseblaster just before the signal to trigger the sequence. With 24 digital bits from the Pulseblaster, we can have 6 digits of resolution, corresponding to 100 Hz in frequency resolution. A typical frequency sweep starts at 40 MHz and ends between 2 and 10 MHz at BEC.

There are three cameras currently in use in the experiment. The camera imaging in the main chamber is a Pixelfly QE made by Cooke Corporation, while the two on the science chamber are a Flea2 and Flea2G from Point Grey Research, Inc. All three cameras have pixels that are approximately $4.5 \mu\text{m}$ square. In addition, each camera outputs 12 bits of data, but the S/N is better on the Pixelfly, and

the Flea2G has a much better sensitivity at 780 nm, the wavelength that we use for imaging. Both Flea cameras have an IEEE-1394 (Firewire) interface with the computer, which has a Firewire card occupying one of its PCI slots. The Pixelfly interfaces with a Framegrabber card, also in a PCI slot in the computer. The trigger inputs for the Flea cameras are available from a connector at the camera, while triggering of the Pixelfly takes place at the framegrabber. For more information on the imaging systems, see Sec. 3.9.

The third computer only controls the Aerotech air-bearing stage used to transport the atoms in the optical tweezers, which comes with its own PCI card that controls a brushless servo motor to drive the stage. The stage requires air at 80 PSI, and we use both a dryer and a filter to clean the air before it gets to the stage.

3.10.2 Software

There are three different software programs in use to control the equipment. The bulk of the interface and control is done with NI Labview, while the majority of the analysis is done with Igor Pro from Wavemetrics. The airstage has its own control software as well. The original software in Labview and Igor was written by Dr. Trey Porto and then modified by Dr. Ian Spielman before I configured it for use in our experiment. An overview of how the two main control programs work is given in Fig. 3.13. There is a set of master global variables shared by the two programs “CycleX.vi” and “SetList.vi”. Operation typically runs in a loop, with CycleX looping a set of timed commands (defined in the global variables) to each

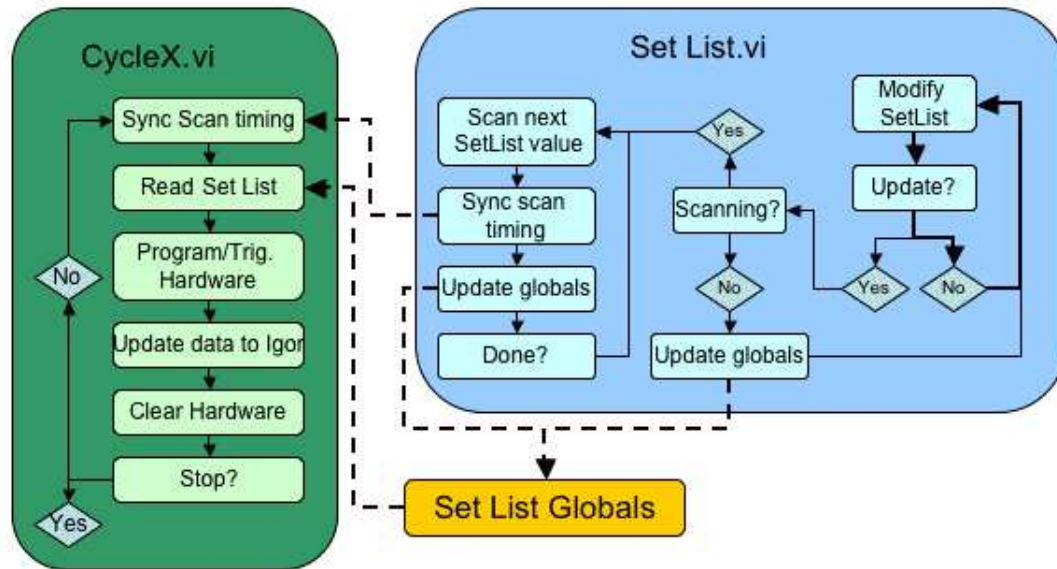


Figure 3.13: Diagram showing the control software used in the experiment. A set of global variables is shared between two programs, with SetList primarily interacting with the user, while CycleX primarily interacts with the hardware.

piece of equipment and then restarting the loop unless stopped by the user. The Setlist VI has a graphical user interface (GUI) to accept input and write it to the set of global variables, while CycleX reads these global variables, loads the hardware, and triggers the experimental cycle.

An example of the main interface of the setlist is shown in Fig. 3.14. Time runs in the vertical direction. Each green circle represents a digital output from the pulseblaster, while the analog outputs are in the columns on the right. The value of the “delay” column is how long each set of outputs is held before switching to the next row of outputs. In addition, linear ramps from one analog output to the next can be implemented in the “option” column on the left-hand side. This implements a linear ramp for any analog output values which are changed on the “ramp” step.



Figure 3.14: Graphical user interface for the software controlling the apparatus. Green circles represent digital outputs, while red numbers are analog outputs. Each set of outputs is held for the amount of time in the “delay” column.

In addition, the setlist can run automated scans of analog values or delays, stepping through a set of defined variable values, scanning multiple values at once if required. The timing is controlled so that each experimental cycle deterministically moves on to the next value in the scan. This timing control is implemented by allowing only one of CycleX or Setlist to have access to the global variables at one time. CycleX allows Setlist access once per cycle, and if in scan mode, the Setlist updates the variables every time it has access. The name of the scanned variables can be input as well, and communicated to Igor using DDE, a communication protocol between programs and computers.

Digital line #23 is used to trigger the analog channels. Basically, the set of all analog values including ramps is loaded onto the analog cards sequentially during

the “load hardware” phase of CycleX sequence. Since all the timing is controlled by the Pulseblaster, the analog cards store the entire list of analog values and switch to the next value with every trigger from the Pulseblaster. All of the analog channels can be scaled and named in NI Measurement and Automation Explorer (MAX). The scaling maps a value defined with arbitrary units to the actual voltage required to output that value. For instance, if a 1 Volt output sets a function generator to 80 MHz, then the scaling can be changed so that the user inputs 80 MHz to the GUI, and the software automatically outputs 1 V to the function generator. Meanwhile, every time a channel is renamed, the name must be correspondingly changed in the list of channels programmed by CycleX during the load hardware phase.

The Pulseblaster accepts instructions as an 80-bit “word”. Twenty-four bits control the state of each of the 24 outputs, 4 bits define an “op code”, allowing the pulseblaster to do loops and accept external triggers, 20 bits define a data field corresponding to the op code, and 32 bits define the delay time to hold that particular command. The data field means something different for each op code, specifying things such as the number of loops to perform during a “loop” command. One example of the use of a “loop” op code is implemented for the analog voltage ramps. Each time a ramp is requested, the analog voltage values for the ramp are loaded onto the analog cards. Then, the digital outputs for the pulseblaster on the ramp step are duplicated into two steps with the exception of the trigger to the analog card, which is changed from low to high on the second step, while setting the delay time equal to the total time of the ramp divided by twice the number of ramp steps. Looping these two pulseblaster commands will keep all of the digital output

commands the same and trigger the analog cards to go their next saved value. In this way, only two command steps are stored in the Pulseblaster memory, while the analog voltage can be ramped from its start to end value in as many steps as the user wants.

In computer #2, a second Pulseblaster is programmed in a similar way in order to control the RF synthesizer which sweeps the radiation used for evaporation in the magnetic trap. In this case, there is a Labview VI which accepts an arbitrary number of linear frequency ramps with an arbitrary number of steps up to the 32000-step memory of the Pulseblaster. Each user-specified ramp is divided into time and frequency steps in Labview, and then the appropriate combination of digital outputs is loaded into the pulseblaster memory. A trigger from the first Pulseblaster sends this series of commands to the function generator, with an analog voltage controlling the amplitude of the RF output signal from the function generator.

The third control software program runs the airstage in order to move the atoms out to the science cell in the optical tweezer beam. In Ref. [36], it is found that a trapezoidal acceleration profile is appropriate for the movement of the stage in order to minimize heating and loss during the movement of the atoms. A constant value for the jerk results during each part of the movement. This profile is very close to having a sinusoidal position as a function of time, which can be programmed fairly simply in the stage software. First, we calculate the velocity and position profile that we want and determine what the maximum velocity is during this movement. Then, setting a ramp command to be half of the value of the total time required for the move and commanding the distance with this same maximum velocity generates

an appropriate profile. In this case, the stage must be set to not smooth the velocity profile (command “g9”) during the move to give the correct result. In the past, we divided the required movement into a series of discrete time steps and fed them to the stage, but this requires significant processing power from the computer running the stage, and does not seem to be advantageous compared to the current scheme. The software driving the stage is similar to the “C” programming language, but it has its own set of functions and commands.

The pictures are all acquired in Labview on computer #2 using National Instruments drivers for the cameras. The Pixelfly camera has its own drivers, while the Flea cameras use generic Firewire camera drivers. For some reason, the Pixelfly images are straightforward to obtain and analyze using Labview driver VIs, but there are some tricks for the Flea cameras. The IMAQdx drivers for these cameras are not part of a standard Labview installation, and are only available in the “Vision” Labview add-on. In addition, the settings for the cameras must be adjusted in NI-MAX. Each camera sends 16 bits of data, but 4 bits are set to be always 0, so MAX must be set to ignore the appropriate bits in each pixel. The correct settings for this in MAX are:

Actual Bit Depth	12 bits
Bit Alignment	MSB
Byte Order	Little Endian

In addition, the speed of the cameras was limited by windows XP service pack updates, so patches from Point Grey Research had to be applied to use the full frame rate of these two cameras - 15 fps for the Flea2 and 30 fps for the Flea2G.

Finally, the Flea2G has an unresolved triggering issue, which seems to trigger it at the wrong point in the experimental cycle occasionally, despite the fact that we use the same trigger signal for all of the cameras.

One recent modification allows the Labview VI which acquires pictures from the Flea2 cameras to take and save scope traces from a Tektronix TDS2014B oscilloscope. These traces can be sent to Igor along with the pictures, as well as saved to the hard drive. We typically use these traces to monitor the intensity locks of lattice or speckle beams.

Finally, all of the analysis on the absorption images is done in a program called Igor Pro. Igor receives two images via DDE - one of the atoms and one of the probe beam without atoms, with the background image already subtracted from each of them. By dividing these two images we can calculate quantities such as temperature, phase space density, chemical potential, and density. The software is advanced enough that most of these quantities can be calculated in real-time as the images come in, since the creation of our sample typically takes about 30 seconds.

As each image comes in, the density profile is fit with either a Gaussian function, Thomas-Fermi function ([46, 32]), or a combination of both. From the Gaussian width and amplitude plus the user-supplied values of the expansion time and trap frequencies, the number and temperature of the thermal atoms can be calculated. The Gaussian width σ of an initially Gaussian atom sample of width σ_0 with individual atomic masses m and temperature T after an expansion time t in 1D is given

by (see appendix A of Ref. [150]):

$$\sigma^2 = \sigma_0^2 + \frac{k_B T t^2}{m}, \quad (3.8)$$

with k_B Boltzmann's constant.

Since the total energy for a particle traveling between $\pm x_0$ in a harmonic trap with frequency ω is $\frac{1}{2}m\omega^2 x_0^2$, we can equate x_0 with σ_0 and use the equipartition theorem for a harmonic oscillator to find

$$\frac{1}{2}k_B T = \frac{1}{2}m\omega^2 \sigma_0^2. \quad (3.9)$$

Substituting this into Eq. 3.8 yields an expression for the original size of the cloud that depends only on the initial trap frequency, expansion time, and size after expansion. These two relationships are used in the software to calculate both the temperature and the original size of the cloud. In order to get the number of atoms in the cloud we can assume that the image we see is the optical density as a function of two spatial coordinates and then assume that the cloud is Gaussian in the third dimension and that the absorption image has integrated over that dimension. The optical depth is related to the atomic density via Beer's law (Sec. 3.9), and so integration of the Gaussian optical depth yields an expression for the total number N based on the widths of the cloud σ_x and σ_y , the amplitude A of the absorption and the absorption coefficient σ_A :

$$N = \frac{A\pi\sigma_x\sigma_y}{\sigma_A}. \quad (3.10)$$

With the number and temperature now determined, the phase space density of the atoms in the trap $\rho_{PSD} = \frac{N}{V}\lambda_{dB}^3$ can be calculated. In this expression, V is

the volume of the trap and λ_{dB} is the deBroglie wavelength of the atoms in the trap. For particles in a harmonic trap, the volume of the trap can be calculated similarly to above by relating the temperature of the atoms to the endpoints of the motion. This yields:

$$\rho_{PSD} = \frac{N\omega_x\omega_y\omega_z\hbar^3\pi^{\frac{3}{2}}}{8k_B^3T^3}, \quad (3.11)$$

where ω_i is the trap frequency in each direction.

Once the atoms are cold enough that they condense into a BEC, they can be fit with a Thomas-Fermi function, which is a truncated upside-down parabola. This fit assumes that there enough atoms in the condensate that the Thomas-Fermi approximation holds, which is the usual situation in most BEC experiments. The fits yield an amplitude A and a width of the distribution given by the Thomas-Fermi radius R_{TF_i} , the x or y-value of the fit when the z-value goes to zero. The number of atoms in the condensate can be calculated in a similar way as in the Gaussian case, by assuming a 3D Thomas-Fermi density distribution and then integrating that distribution over all space to determine the relationship between the number of atoms in the BEC N_{BEC} and the fit parameters A , R_{TF_x} , and R_{TF_y} , as well as the absorption coefficient σ_A :

$$N_{BEC} = \frac{2\pi AR_{TF_x}R_{TF_y}}{5\sigma_A}. \quad (3.12)$$

In addition, because of the relationship between between chemical potential and total atom number, there is a relationship between the trap frequencies, Thomas-Fermi radii, and atom number, eliminating the amplitude of the fit from the calculation,

but adding in dependence on the trap frequencies:

$$N = \frac{a_{HO}}{15\sigma_A} \left(\frac{(R_{TF_x} R_{TF_y} R_{TF_z})^{1/3}}{a_{HO}} \right)^5. \quad (3.13)$$

Here, $a_{HO} = \sqrt{\frac{\hbar}{m\omega_{HO}}}$, and $\omega_{HO} = (\omega_x\omega_y\omega_z)^{1/3}$. Once the total number of atoms has been determined, the chemical potential μ of the BEC is simply given by

$$\mu = \frac{\hbar\omega_{HO}}{2} \left(\frac{15Na}{a_{HO}} \right), \quad (3.14)$$

where a is the scattering length of the atoms. If the sample contains thermal atoms and condensed atoms, the software can use a combination Gaussian and Thomas-Fermi fit to fit the distribution, calculating parameters in a similar way to that given above, yielding separate attributes for each part of the bimodal distribution.

The experimental parameters such as coil currents for the magnetic trap or beam powers for the optical trap are passed to Igor using DDE. Thus, the user inputs these values in the Setlist.vi GUI, and then Igor uses these values to calculate trap frequencies using the methods described in Secs. 3.6 and 3.8. The numerically calculated magnetic trap frequencies as a function of coil currents are preloaded into the Igor software and used as a lookup table, while the optical trap frequencies are calculated each time from the simple algebraic relations given in Sec. 3.8.

In addition, there are two sets of functions implemented in the software that have not really been utilized yet, but have been tested and seem to work. One set of functions allows for defocus contrast imaging [146, 147], while the other set of functions can build and use a PCA basis (Sec. 3.9)[137]. The defocus contrast imaging functions allow the user to select (in the Labview imaging software) the type of imaging being done and specify a distance defocused. The software then

applies the defocus contrast imaging algorithms to the input images in order to generate the optical depth. In order to build a PCA basis, a function can be called in IGOR which will take a set of images and use the second picture (probe beam background) from each of the images to generate a basis set. Then, a checkbox in the Igor front panel allows the user to divide by the projection of the absorption image onto the PCA basis rather than the incoming background image to get the optical depth. This may result in cleaner images.

Chapter 4

Advanced Experimental Setup

Now that I have detailed the how the apparatus creates Bose-Einstein condensates, I will use this chapter to detail how we interact with the condensate to perform experiments. In general, we use off-resonant light to manipulate the sample, forming either a periodic or disordered potential, or a combination of both. This light is produced by the Ti-Sapphire laser, and its beam path diagram is shown in Fig. 4.1.

4.1 Incommensurate Lattices

The first experiments performed on this apparatus were done in the magnetic trap [54], and the disorder in this case was provided by incommensurate lattices - two or three superposed optical lattices of incommensurate period. An optical lattice is a periodic potential created by a standing wave of light, which provides a periodic spatial intensity pattern, and therefore a periodic potential (Eq. 2.3). The easiest way to create this standing wave is to reflect a beam back on itself, providing a sinusoidal intensity at a period of half of the wavelength λ . However, this could just as easily be two independent beams with the same frequency and polarization (Fig. 4.2). In this case, we can also intersect the beams at an angle θ less than 180° ,

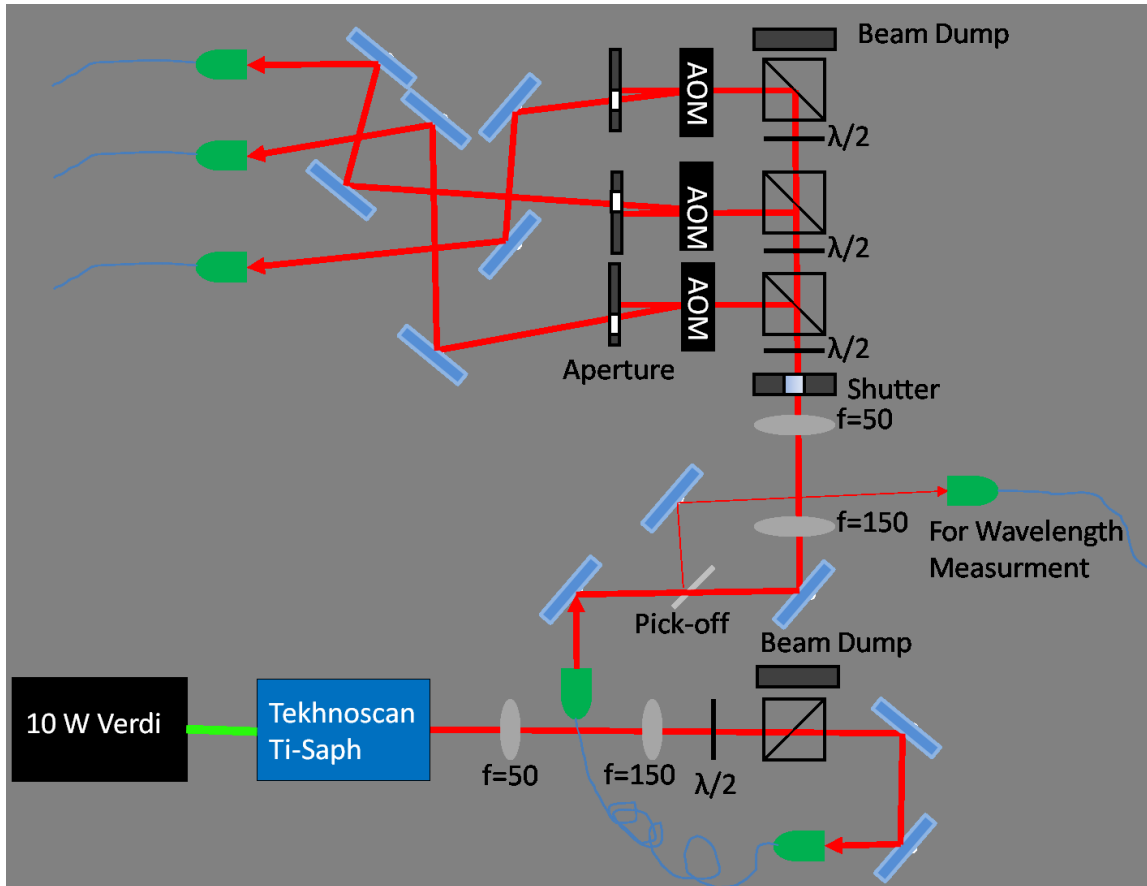


Figure 4.1: Beam path for Ti-Saph laser used to create lattices and disorder. Feed-back to the AOM stabilizes beam intensities at the outputs of the fibers on the top left.

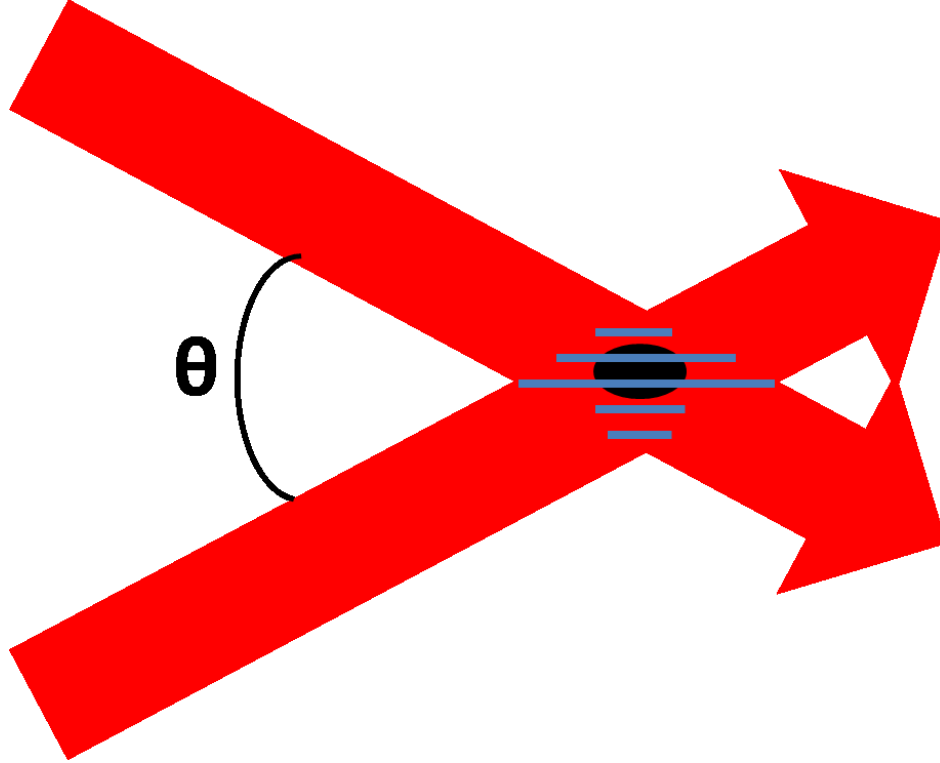


Figure 4.2: Intersecting two lattice beams at an angle θ changes the period of the lattice (Eq. 4.1).

which changes the period d of the lattice as

$$d = \frac{\lambda}{2\text{Sin}(\frac{\theta}{2})}. \quad (4.1)$$

We use this property to change the period of our lattices in the chamber. The specifics are detailed in [55, 54], but the basic idea is that we use the in-vacuum mirror to reflect our lattice beams. If the beam is incident normal to the mirror, then the period of the lattice is $\lambda/2$, which gives a period of ~ 400 nm for our lattice. However, if the beam is incident on the mirror at an angle, and the beam is large enough to hit the atoms both before and after reflection, then the angle of intersection between the incident and reflected beams will no longer be 180° , and the period of the lattice will be longer. We could put as many as three beams in at

once, each creating a lattice with a different spacing, with ratios of $d_1/d_2 \approx 0.806$ and $d_1/d_3 \approx 0.919$, where $d_1 = \lambda_1/2$ is the beam at normal incidence. The gold mirror provides a convenient node in all three standing waves, allowing the lattices to be effortlessly phase-locked, normally a difficult task.

4.2 Speckle Disorder

In the science chamber, our disorder is provided by a speckle intensity pattern, similar to [45, 152, 151, 35, 101, 40, 41]. The field of optical speckle is very broad, and there has been significant investigation into its properties [70]. Basically, if laser light incident on a rough surface is subsequently focused, there will be a disordered intensity pattern at the focus, with a smaller average feature size for a larger numerical aperture of the focusing lens.

Our speckle disorder is created with a collimated Gaussian beam hitting a phase diffuser made by Luminit, model #L.5P1-2. This phase diffuser is a surface relief structure replicated from a holographically recorded master. It acts as a series of micro-lenslets, and diverges the incoming light by a specified angle, 0.5° in our case. The result can be thought of as randomizing the phase of the wavefront. We focus this randomly phased wavefront onto our sample using a Gradium lens made by Lightpath Technologies, model #GPX10-10. Gradium lenses use a varying index of refraction along the lens to allow lower f-numbers at larger working distances. This lens has a 1 cm back focal length and a diameter of 1 cm, with $f/\#$ 1.1.

Physically, because we also want to send a probe beam along the path of the

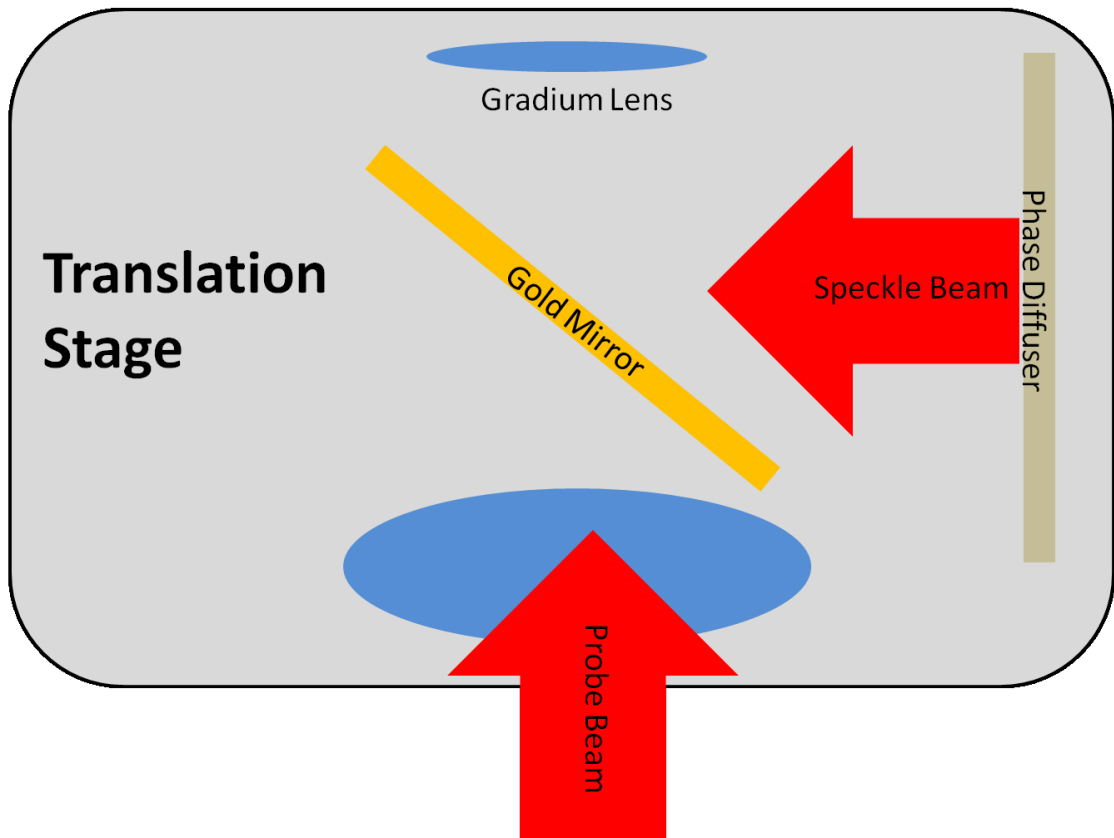


Figure 4.3: Implementation to create speckle potential. The gold mirror has a hole in the middle to allow the focused probe light to pass through to the gradium lens and onto the atoms. The large speckle beam is reflected by the gold mirror through the gradium lens.

speckle, the optics are arranged as shown in Fig. 4.3. The entire setup is on a translation stage in order to allow fine alignment of the speckle potential on the atoms. The two beams are combined with a 1" square gold mirror which has a ~ 1 -2 mm hole in the center, fabricated at the Fab Lab at UMD by plating gold on an optical flat. The probe beam is tightly focused through this hole, goes through the gradium lens, and ends up roughly collimated at the atoms. The speckle beam is large and collimated when it hits the gold mirror, and so it is focused at the atoms. The small hole in the mirror does not seem to have a large effect on the speckle pattern, as aberrations do not affect the random pattern.

To characterize the disordered potential, we need to know two things: the size of the features and the average strength of the potential. The first of these can be simply characterized by taking the speckle system offline and measuring the autocorrelation length of the intensity. The autocorrelation function $C(\vec{r})$ of an intensity $I(\vec{r})$ is defined as

$$C(\vec{r}) = \int I(\vec{r})I(\vec{r} - \vec{r}')d\vec{r}', \quad (4.2)$$

and the width of the peak around zero represents a measure of the average feature size of the speckle pattern, known as the correlation length [41, 152]. We need this feature size to be much less than the size of our condensate in order to make a disordered potential, and so we would like a peak width on the order of 1 μm .

We observed the speckle pattern on a CCD camera by imaging with microscope objective to get the necessary spatial resolution. A sample speckle image is shown in Fig. 4.4. In addition, by translating the entire imaging system by small

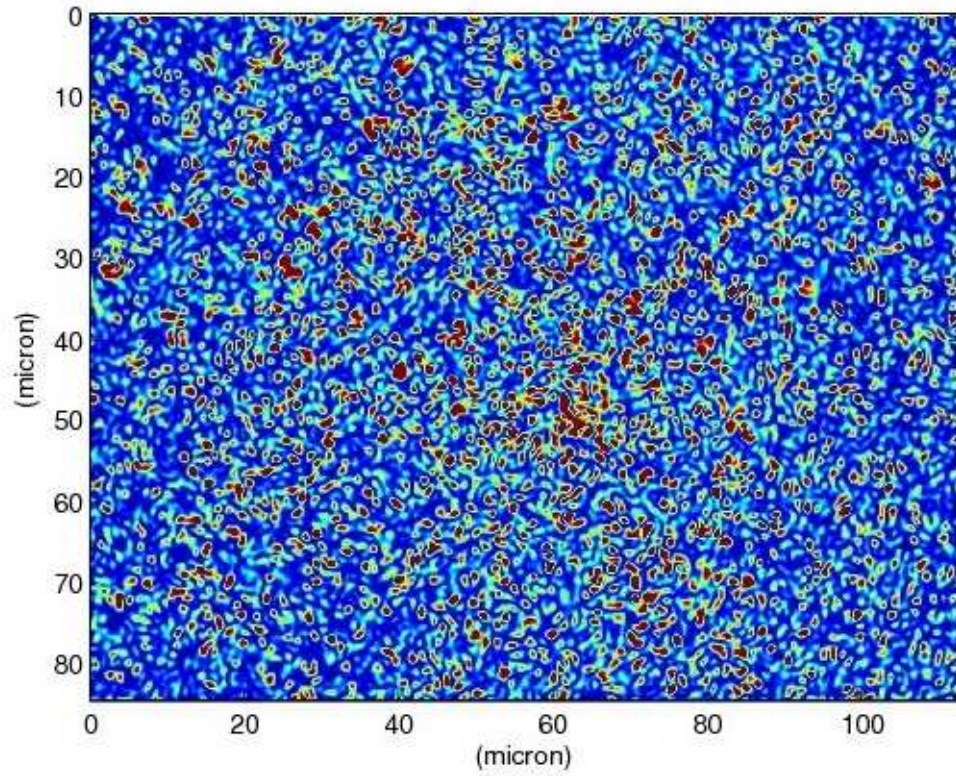


Figure 4.4: Example of radial speckle intensity pattern used for random potential.

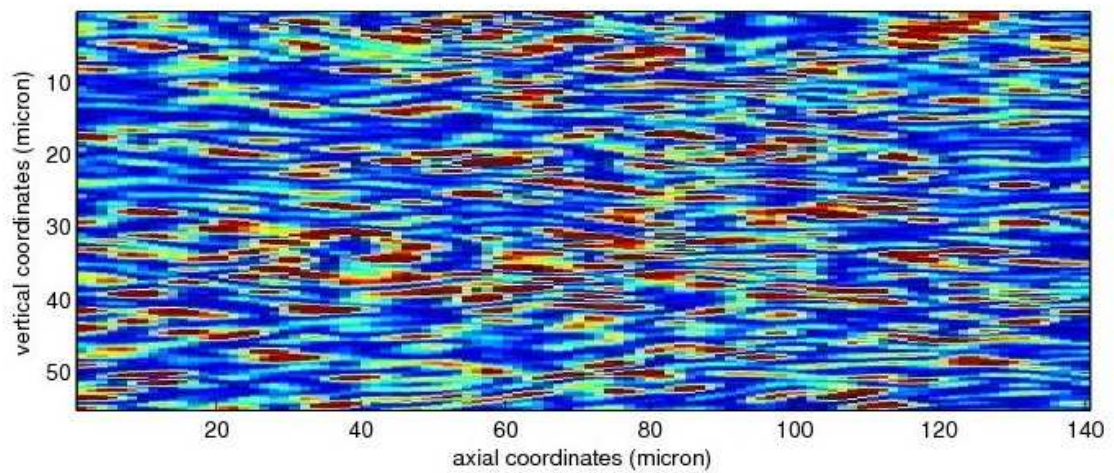


Figure 4.5: Example of a cut along the axis of a speckle intensity pattern used for random potential.

amounts, we can map out the speckle pattern as a function of axial distance along the beam by piecing together separate pictures at ~ 30 nm separation. The images are then corrected for small camera jitter by computationally translating each image to minimize the radial correlation function between it and the previous image. A cut along the center of such an analysis is shown in Fig. 4.5. It is clear that the feature size along the axis of the beam is much larger than the feature size radially.

A plot of the 2D autocorrelation function for both the radial and axial intensity is shown in Fig. 4.6. An exponential fit can be used to define an autocorrelation length [59], and the fit yields widths of the peaks of ~ 700 nm radially and ~ 6 μm axially. However, these images are taken with a Helium-Neon laser, which has a wavelength of 633 nm, and we use a wavelength of 800 nm in the experiment, which increases the correlation length by the ratio of the wavelengths. We thus expect correlation lengths of ~ 885 nm radially and ~ 7.5 μm axially. The radial size of the speckle is still much smaller than the size of our BEC. Finally, because the speckle is smallest at the focus of the beam, we would like to know how sensitive the radial correlation function is as a function of axial distance from the focus. This will tell us how sensitive the alignment of the beam is. A plot of the transverse correlation function peak height between consecutive images after correction for camera jitter is shown in Fig. 4.7. It shows that the transverse correlation length does not change much over 100 μm , since the correlation function peak height does not change much over this distance. We also simulated the wall of the vacuum chamber in the beam, finding that it did not make any difference in the speckle size, as expected for random speckle. Most of the above characterization and analysis was performed by

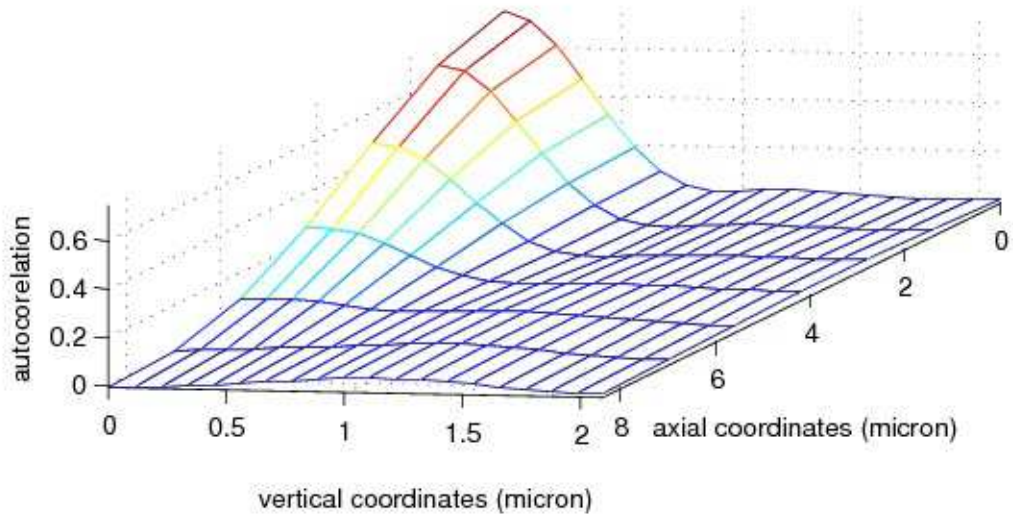


Figure 4.6: 2D autocorrelation function along the axis of the speckle beam and in one transverse direction. The origin is at the focus of the beam.

our postdoc, Dr. Tao Hong.

Now that we have characterized the size of the features in the disorder, we need to have some way to characterize the overall average strength of the potential. Since the potential depth is equal to the light shift that the atoms experience, we could measure the light shift directly [41]. Another possible way to measure this strength is to displace the beam slightly from being centered on the atoms, which should apply a force that displaces them [152]. We decided to use the effect of a short pulse of light on a thermal ensemble of atoms to measure the strength of the potential. For a short pulse of light, each atom should receive an impulse which is proportional to the derivative of the intensity at that point. The result is that the shape of the momentum distribution of the atoms stays the same, but the width of the distribution (the effective temperature) becomes larger. We can measure

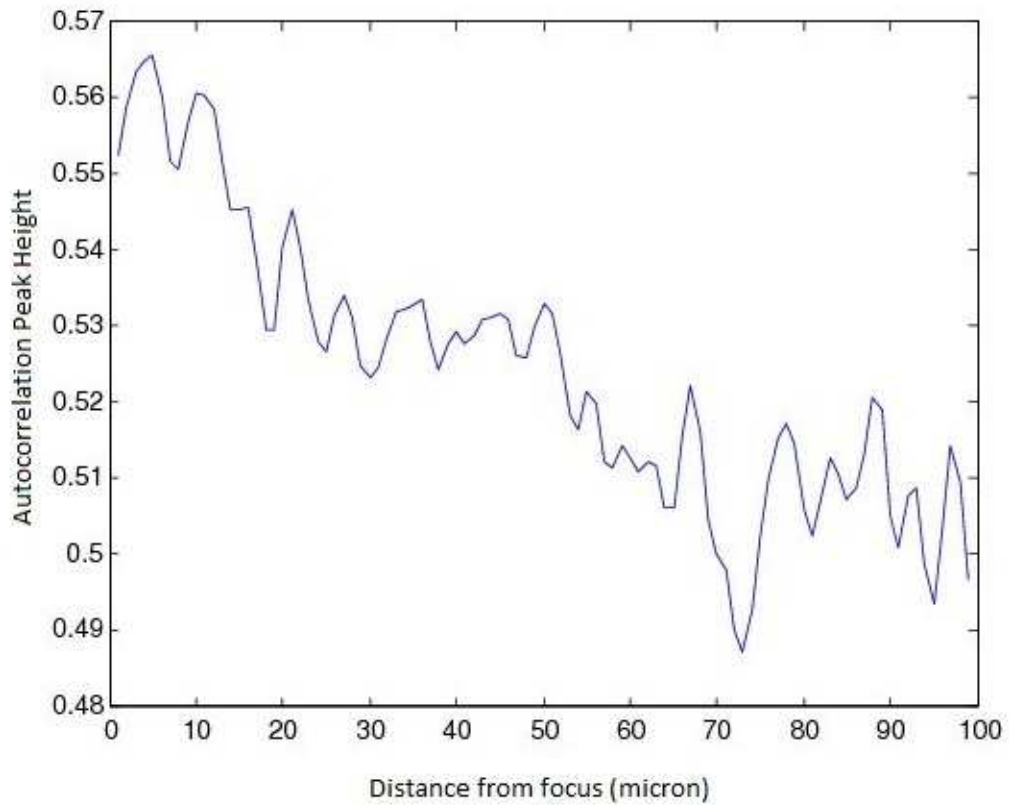


Figure 4.7: Unnormalized correlation peak height of consecutive images as a function of distance from the focus of the disordered beam, corrected for camera jitter.

this increase in momentum width by pulsing the speckle beam on the atoms and then immediately allowing them to expand and measuring their average momentum width before and after pulses of different strengths.

In order to translate this information into an average strength, we must be able to compare the resulting increase in momentum width with some theory. The process can be simulated by first modeling a speckle intensity pattern, using an algorithm from [70]. We can then model the atoms because we know the initial momentum distribution, and because the trap is harmonic, we also know the initial spatial distribution. We use the size of the initial spatial distribution to determine the size of the speckle distribution that the atoms sample, assuming that we know the correlation length of the speckle from the offline measurements. Then we can use a Monte-Carlo simulation to randomly choose an atom from the appropriate momentum distribution. This atom receives an impulse proportional to the derivative of the intensity at a point randomly chosen from the part of the speckle being sampled. If we do this for a large number of atoms, it should simulate the effect of a speckle pulse on a thermal ensemble of atoms.

This process is then repeated for different speckle patterns, since the process of simulating speckle changes the pattern from realization to realization. In fact, in order to make sure that we are using correctly-sized speckle, we take the autocorrelation of the generated pattern and use that for calibration on every new run. Then, we have to scale the speckle by an overall “strength” which most closely matches the effect of the pulse in the experiment. This strength is the average potential value that we are looking for. Because of the nature of the process, each step must

be averaged - we use different speckle distributions, strengths, and many atoms for each run. The result allows us to calibrate the strength of the speckle to within 10%.

With the information about both the speckle grain size and overall average strength of the speckle potential, we know all the parameters necessary to use it in the experiment. Sample images of the effect of speckle disorder on a 3D BEC are shown in Fig. 4.8. After creating a 3D BEC, the disorder potential is linearly ramped on in 500 ms, and then the atoms are held for 200 ms before 26.95 ms of free expansion. The axis of the speckle beam is horizontal in these images, leading to striations and increased width in the vertical direction. This is due to the fact that the speckle correlation length is anisotropic, and thus smooth along the horizontal axis of the image.

4.3 2D System Creation

If we want to investigate the effects of disorder on 2-dimensional systems, then we must tightly confine our 3-dimensional condensate in one dimension. In order to be in the 2D regime, the oscillation energy $\hbar\omega$ in the tight direction must be much greater than both the thermal energy $k_B T$ and the chemical potential μ of the BEC. For typical BEC parameters, this works out to be $\frac{\omega}{2\pi} \gg 3$ kHz.

There have been many methods used to create 2D ultracold gases [71, 38, 132, 67, 87]. One conceptually simple way to create a stack of 2D gases is with a deep optical lattice [113, 30, 93, 111, 141]. In this case, even for relatively shallow lattices,

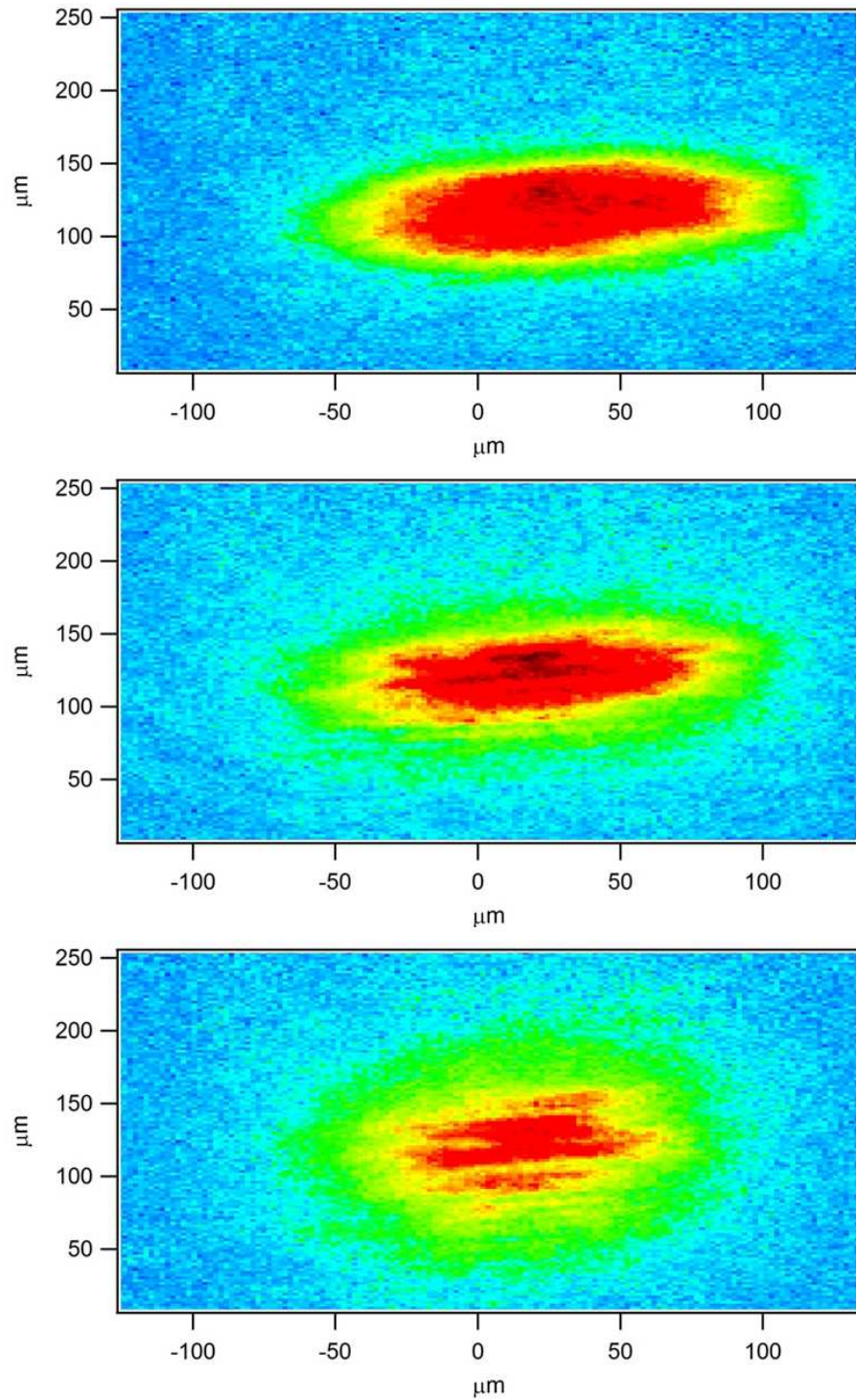


Figure 4.8: Effect of disorder on 3D BEC. The disordered potential was linearly ramped on in 500 ms to 0 (top), 750 Hz (middle), or 4 kHz (bottom), and the atoms were held for 200 ms in the potential before 26.95 ms of free expansion. The axis of the speckle beam is horizontal in these images.

the oscillation frequency in each plane can easily be large enough to place the gas strongly in the 2D regime. The disadvantage to the optical lattice is that the spacing of the planes is small, and a typical 3d BEC creates many 2D systems. With many 2D systems, only average quantities can easily be measured. The method that we use to overcome this problem is to bring in the lattice beams at a shallow angle, which greatly increases the lattice period (Fig. 4.2) [78, 144, 76]. This will allow us to create a small number of 2D systems at the expense of a lower oscillation frequency in the tight direction. However, there is an experimentally accessible 2D parameter regime which creates only 1 or 2 2D systems.

Since many of the quantities that we are interested in are related to the phase coherence of our sample, it is actually advantageous to have 2 planes instead of 1, so that one of the planes can be used as a phase reference in quantum interference experiments. For our wavelength near 780 nm, an angle between the beams of $\sim 15^\circ$ generates a lattice spacing of about $6 \mu\text{m}$, which should divide our 3D BEC into two planes along its shortest axis.

Since the shallow angle weakens the lattice, we must use a large intensity or tune our lattice beams relatively close to atomic resonance in order to get the required oscillation frequencies to reach the 2D regime. However, we must also minimize the absorption and rescattering of photons, which causes heating. We do not observe significant heating in our lattice, observed by ramping the lattice on and then back off. The issue of heating in an optical lattice is still an interesting one [66].

Physically, because space is tight around the science chamber with the cross-

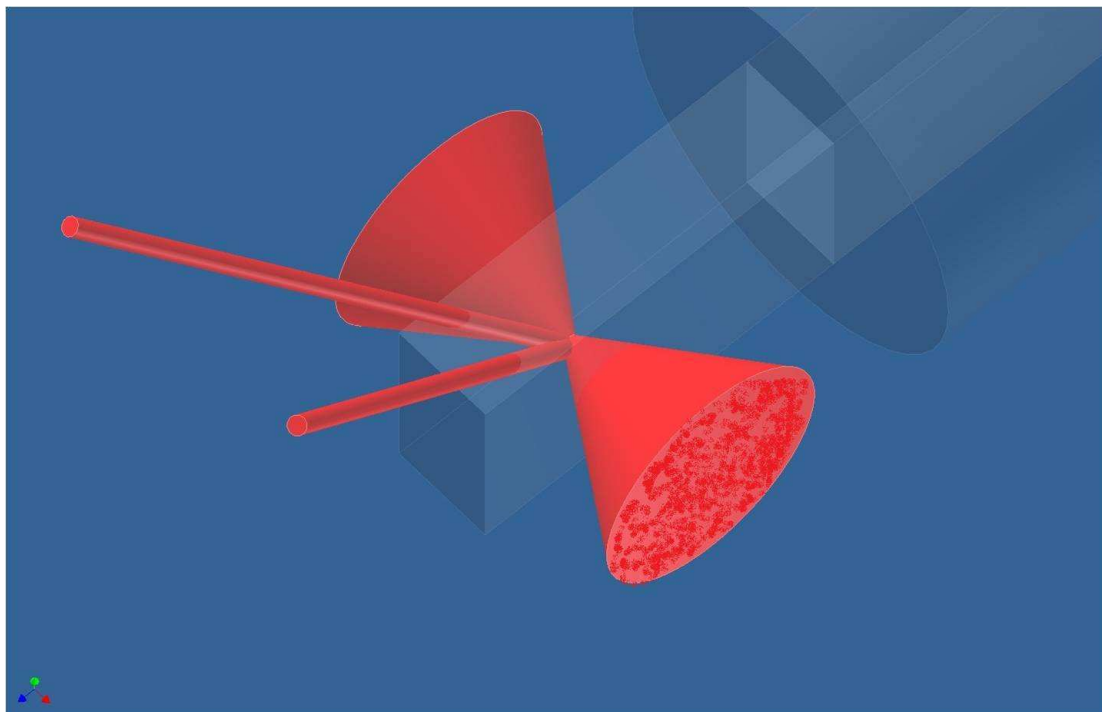


Figure 4.9: Orientation of shallow angle lattice for creating 2D systems and speckle beam for producing a disordered potential. The thinner beams are the lattice, while the sharply converging beam is the speckle beam.

beam optical trap, speckle beam and probe beam optics, the lattice enters the science chamber from above at 45° from vertical. A schematic showing the orientation of the lattice and speckle beams is shown in Fig. 4.9. This geometry gives us planes oriented vertically, so that the speckle beam's axis is normal to the planes. This gives us the smallest speckle size in the planes, and since the planes are so close together, the disordered pattern should not be appreciably different between the two planes. With 100 mW in each beam at a wavelength of 776.5 nm we can predominantly load two planes with oscillation frequencies greater than 8 kHz in the tight direction. However, one thing which we did not fully appreciate about this geometry is that the lattice is not along a symmetry axis of the original trap. Since

the cross beam comes in at an angle of 16.7° in the horizontal plane, the symmetry axis of the condensate is at $\sim 8^\circ$ from the lattice axis, which causes a position offset in the two planes that load (Chap. 5).

In order to create the two beams, a second platform is installed above the science cell, with a slot cut in the middle above the science cell. An output fiber coupler generates a beam which goes through a polarizing beam cube to clean up the polarization, followed by a pick-off for intensity stabilization. This beam hits a 50/50 beam splitter, and the reflected and transmitted beams are focused by an $f = 150$ mm lens onto the atoms. The camera used for vertical imaging is also mounted on this platform.

Typically, one can calibrate the depth of an optical lattice by observing the population in higher momentum modes. Atoms in an optical lattice populate only discrete states in momentum at the reciprocal lattice vectors [9, 52], and the deeper the lattice, the more atoms populate the higher modes. For a BEC in a typical optical lattice, these higher order momentum peaks can easily be distinguished from the atoms with no momentum transferred from the lattice. The population in these other peaks is a simple function of the depth of the lattice. It can be measured after either pulsing the lattice [114] or adiabatically loading the lattice [44], and then observing the resulting momentum distribution after a period of free expansion (Sec. 3.9). In either case, we are interested in the population in the first-order diffraction peaks - those atoms that have made the first discrete jump in possible momentum transfer.

However, with a large-period lattice, the higher order momentum states are not

significantly separated from the rest of the cloud after free expansion, since a larger period lattice has a smaller reciprocal lattice. If the first order peaks aren't separated significantly from the rest of the cloud, it is difficult to measure the population in these peaks. If we are indeed loading just two wells in the lattice, then after free expansion, the two planes will overlap and exhibit a sinusoidal interference pattern. After an expansion time t , the period d of that interference pattern is [8]

$$d = \frac{ht}{md}, \quad (4.3)$$

where h is Planck's constant and m is the mass of the atoms. For reasonable parameters, this gives an interference pattern with $d \sim 10 \mu\text{m}$, which is much smaller than the normal mean-field-produced $\sim 100 \mu\text{m}$ width of the cloud after expansion. Without the first-order peaks being separated from the rest of the atoms, the typical lattice calibration tools are not available. Also, because we do not control the phase of the lattice, and there is only really one or two nodes of the lattice hitting the cloud, a pulse will significantly kick all of the atoms one way or another depending on where the nodes hit the cloud, which varies randomly from shot to shot.

The method we use to calibrate the depth of the lattice is taken from Ref. [143]. If the atoms are tightly confined in the planes, then we can assume that the atoms are in the Gaussian ground state of each of the wells which are occupied. The size Z of the cloud after expansion from each of the wells (ignoring the initial size of the cloud) is

$$Z = \sqrt{Z_0^2 + (vt)^2}, \quad (4.4)$$

where v is the average particle velocity in the cloud, Z_0 is the size of the cloud after

expansion in the limit of no lattice, and t is the expansion time. To find the average velocity, we assume that because the atoms are in the ground state of the potential, the total energy $E = \frac{1}{2}\hbar\omega^2$, with ω the oscillation frequency in each well. At any given time, this is evenly split between kinetic and potential energy, so that the average velocity $v = \sqrt{\left(\frac{2}{m}\right)^{\frac{1}{4}}\hbar\omega^2}$. This is where the depth of the lattice comes in. There is a relationship between the depth of the lattice and the oscillation frequency in each well. We can write the lattice potential as

$$U(x) = U_0 \cos^2\left(\frac{\pi x}{d}\right), \quad (4.5)$$

where U_0 is the depth of the lattice we are interested in and $d = \frac{\lambda}{2\sin(\frac{\theta}{2})}$ the lattice spacing, since θ is the angle between the lattice beams. By taking the second derivative of Eq. 4.5 and setting it equal to $m\omega^2$, we can find ω in terms of U_0 , to finally end up with

$$Z = \sqrt{Z_0^2 + \left(\sqrt{\frac{\hbar\pi}{m}} \left(\frac{U_0}{2m}\right)^{\frac{1}{4}} t\right)^2}. \quad (4.6)$$

This equation can be used to fit the size of the cloud as a function of lattice depth, as shown in Fig. 4.10.

This calibration technique suffers from two assumptions which may not be true. The first assumption is that the atoms are not interacting during the expansion from the lattice, which is almost certainly violated. The second assumption is that the atoms are tightly confined only in the ground state of the lattice, which is true only if the temperature is very low or the confinement is very tight. However, since it was used in Ref. [78], we expect that it should be close to the correct calibration.

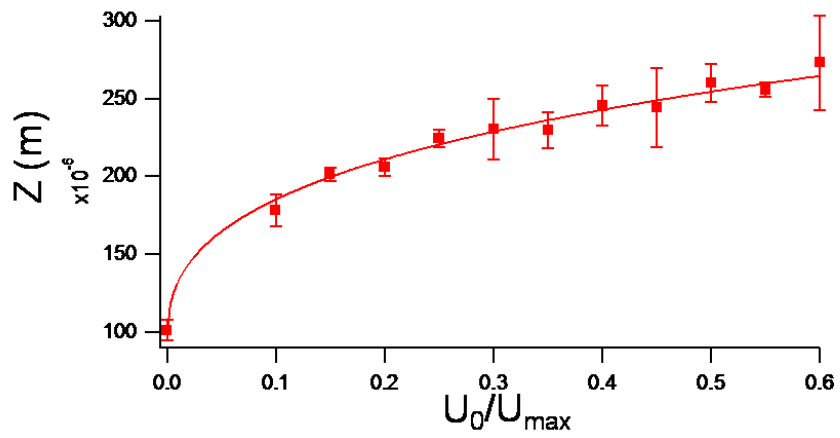


Figure 4.10: Cloud width as a function of lattice depth, with U_{\max} and Z_0 as fit parameters, in units of $U_{\max} = 4.4 \pm 0.2 \times 10^{-27}$ J, with $Z_0 = 98 \pm 5 \mu\text{m}$. Error bars are standard deviations of three scans.

Chapter 5

Experimental Methods and Results

5.1 2D Systems and Observation of BKT Transition

After setting up the lattice we would like to observe the BKT phase transition. Once we are sure that the oscillation frequency in the lattice is high enough to put us in the 2D regime, there are two main experimental indicators of the BKT phase transition to a superfluid [76]. As the system starts to develop long-range phase coherence and turn superfluid, two independent systems will interfere with one another if they overlap during free expansion (Fig. 5.1). Because each of the systems expands most rapidly in the tightly confined direction after release, there will be total overlap if the two systems are within a few microns of each other. The phase of this interference pattern will be random from realization to realization, set by the overall uncontrolled phase of each system, and the average fringe visibility over many shots is related to the coherence length of the two systems [121, 127]. In addition, the freely expanding distribution will become bimodal, with a narrow distribution on top of a broader thermal background. The appearance of an interference pattern coincides with the appearance of the bimodal distribution.

Another indicator of the BKT phase transition is the occasional appearance of “fringe dislocations” in the interference pattern, which indicate vortices. At temperatures near the phase transition, the appearance of free vortices becomes

more and more likely. Vortex pairs are also more likely, but they annihilate early in the expansion of the cloud, and so we cannot observe them [76]. The phase of the order parameter of a single 2D system containing a single vortex wraps by 2π around that vortex. If we interfere this system with another system with a smooth phase, then the 3D interference pattern will take on a corkscrew shape along the axis of the interference. The spot of zero density in the center of the vortex will be filled by the uniform phase reference cloud, and thus turn into a spot of zero visibility. Since absorption imaging integrates over one dimension of this pattern (Sec. 3.9), the signature of a single vortex in one of the planes is a phase dislocation (or “fork”) in the observed interference pattern. The appearance of these phase dislocations in a bimodal interference pattern as we increase the phase space density tells us that we are observing the BKT phase transition.

Experimentally, in order to observe these signatures, we evaporate in the optical trap to obtain a 3D BEC at different temperatures (Sec. 3.8), and then ramp up the intensity of the lattice beams to their final value in 500 ms, splitting the 3D BEC into two 2D systems. After a 200 ms hold, all of the potentials are shut off, and the atoms are allowed to fall for a variable amount of time before they are imaged (Sec. 3.9). The ramp and hold times are chosen to mimic those used by group of Jean Dalibard [76], which has determined these times to be adiabatic and in equilibrium in a very similar system. The imaging is in the vertical direction (from above in Fig. 4.9), so that we can observe the two systems after they overlap during expansion.

Our first attempts to observe this phase transition yielded strong suggestive

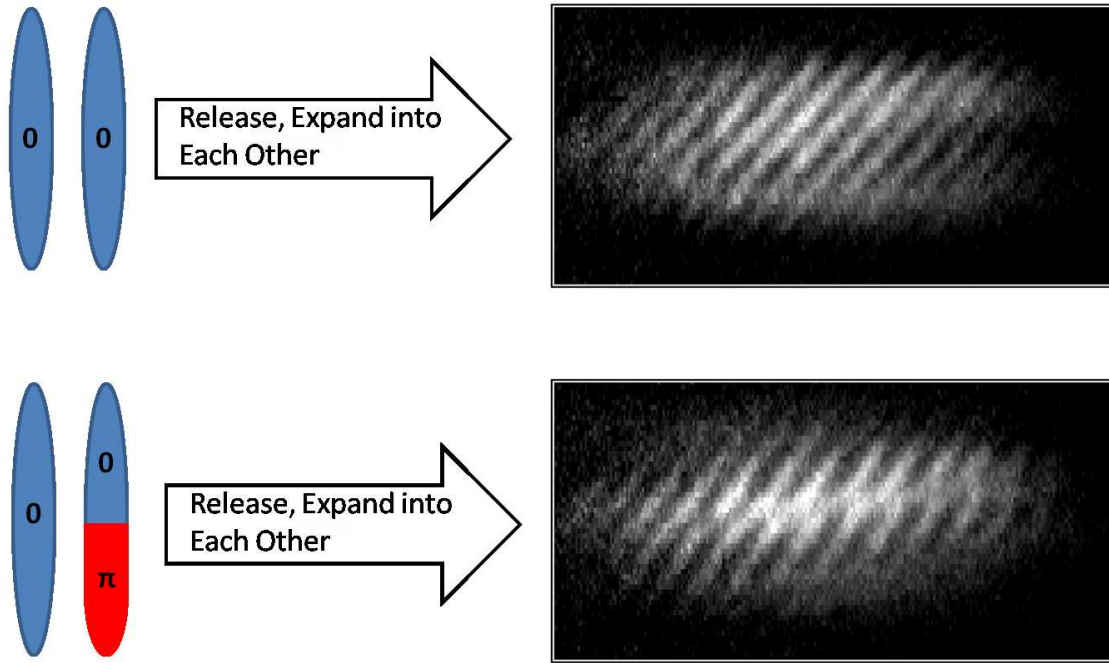


Figure 5.1: Sample absorption images of the interference of 2 2D systems after 37 ms of free expansion. Images are from the side of the initially flat systems, as shown schematically. After expansion, the two systems are completely overlapped due to the fast expansion in the initially tightly confined direction. The image on the top shows no phase dislocations, indicating that each system has a smooth phase. The image on the bottom shows a fringe dislocation caused by a vortex being present in one of the systems just before release. The phase and geometry of each of the systems before expansion is schematically illustrated on the left.

evidence of the transition. We saw a bimodal distribution with an interference pattern after expansion (Fig. 5.1), and some of the images yielded vortices, as we expected. With increasing temperature, the fringe visibility and bimodal distribution disappeared (Fig. 5.2). The spacing of the fringes after 35.95 ms TOF indicated that the original lattice spacing separating the two 2D systems was $\sim 5.6 \mu\text{m}$, as we expected.

However, the fringes of the interference pattern were tilted at an angle with

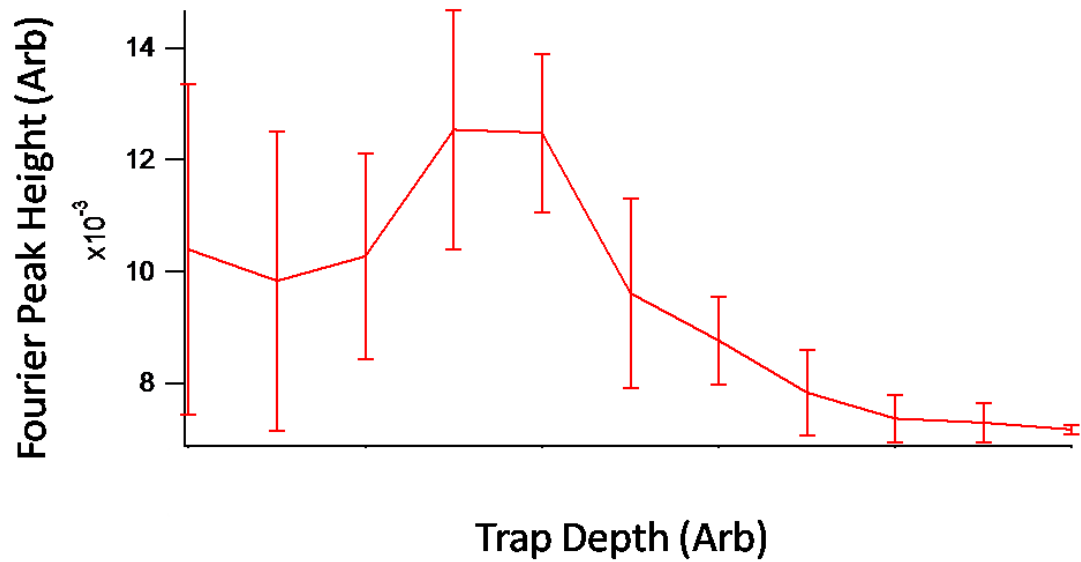


Figure 5.2: Scan of fringe visibility as a function of final trap depth in the $5.6 \mu\text{m}$ lattice. The X-axis is roughly 30 nK per data point, increasing in temperature to the right, starting at the lowest temperature that we see atoms. The Y-axis is the maximum value of the peak in Fourier space in the small region corresponding to observed frequencies of the interference pattern. Error bars are 1 standard deviation of the average of five images at each point.

respect to the angle of the lattice. This angle changed somewhat from shot to shot, with an average of $\sim 60^\circ$. In addition, the frequency of the fringes depended on the angle, with the projection of the frequency along the direction of the lattice being constant. The widest direction of the cloud is perpendicular to the lattice, so the angle is easy to see. In the 2D limit, we expect that the kinetic energy of the atoms dominates their expansion, causing them to expand as free particles. Calculations of the free expansion of two Gaussian wavepackets with our initial conditions indicate that this tilt and frequency change could be caused by an initial relative velocity between the two planes as small as 0.2 mm/s. However, we tried every conceivable experimental method for changing or eliminating a velocity during the loading and turn off of the lattice, and the angle did not change. Its non-zero average indicated a systematically induced velocity on every shot, although we had no mechanism for such a velocity.

A second problem that we were experiencing was instability in the visibility of the fringes. Under the same conditions, the shot to shot visibility of the interference pattern was erratic. In addition, there seemed to be a long term drift that would occasionally yield virtually no visibility for a series of shots despite the fact that the bimodal distribution still existed.

An explanation for both of these phenomena can be found by examining how the BEC loads into the lattice. The lattice planes are in the direction of the tweezer beam for the optical trap. The long axis of the BEC without a lattice will be approximately midway in between the angle between the tweezer beam and the crossing beam. Thus, the planes should be offset from one another, as the minimum

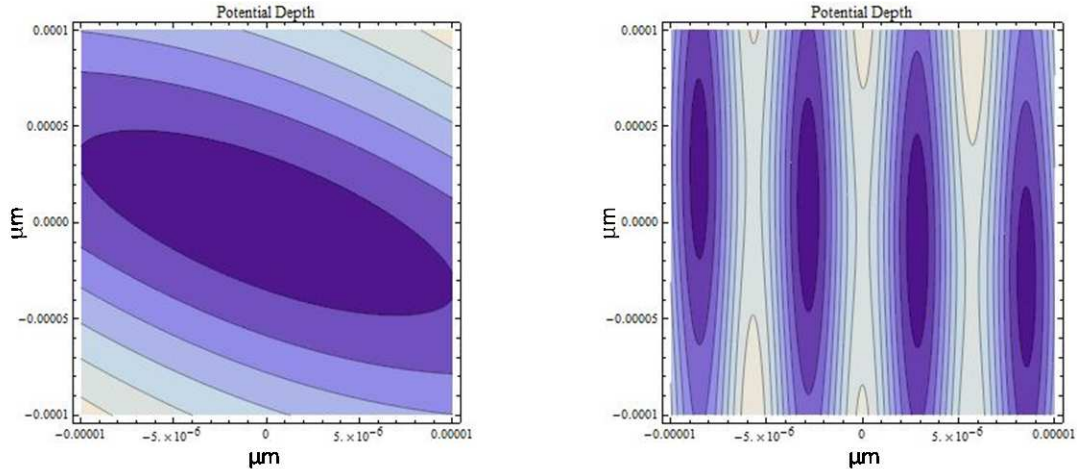


Figure 5.3: Optical lattice potential with and without the lattice on showing the position offset of the lattice planes. Note the unequal scales on the axes. The offset of the planes is $\sim 70^\circ$.

potential at each plane will be separated along the axis of the tweezer beam (Fig. 5.3). Looking at Fig. 5.3, we can measure the angle of offset between the planes, and it comes out to $\sim 70^\circ$, which is very close to the angle of the fringes that we observe. Since the lattice spacing is so large, we can also experimentally image the atoms after only $10 \mu\text{s}$ of free expansion and see the atoms loaded into each plane of the lattice (Fig. 5.4). We do indeed see this position offset.

In addition, in Fig. 5.4 we see that most of the atoms seem to be loaded into one site in the lattice. The amplitude and size of the absorption at that one site is much greater than any other site, although an exact analysis of atom number is difficult. The relative number of atoms in this site fluctuates from shot to shot, as we do not control the phase of the lattice, and there are some shots where barely any atoms appear at any other site. We believe this to be the cause of the fringe visibility fluctuations. In order to get consistent fringes, we must be loading a

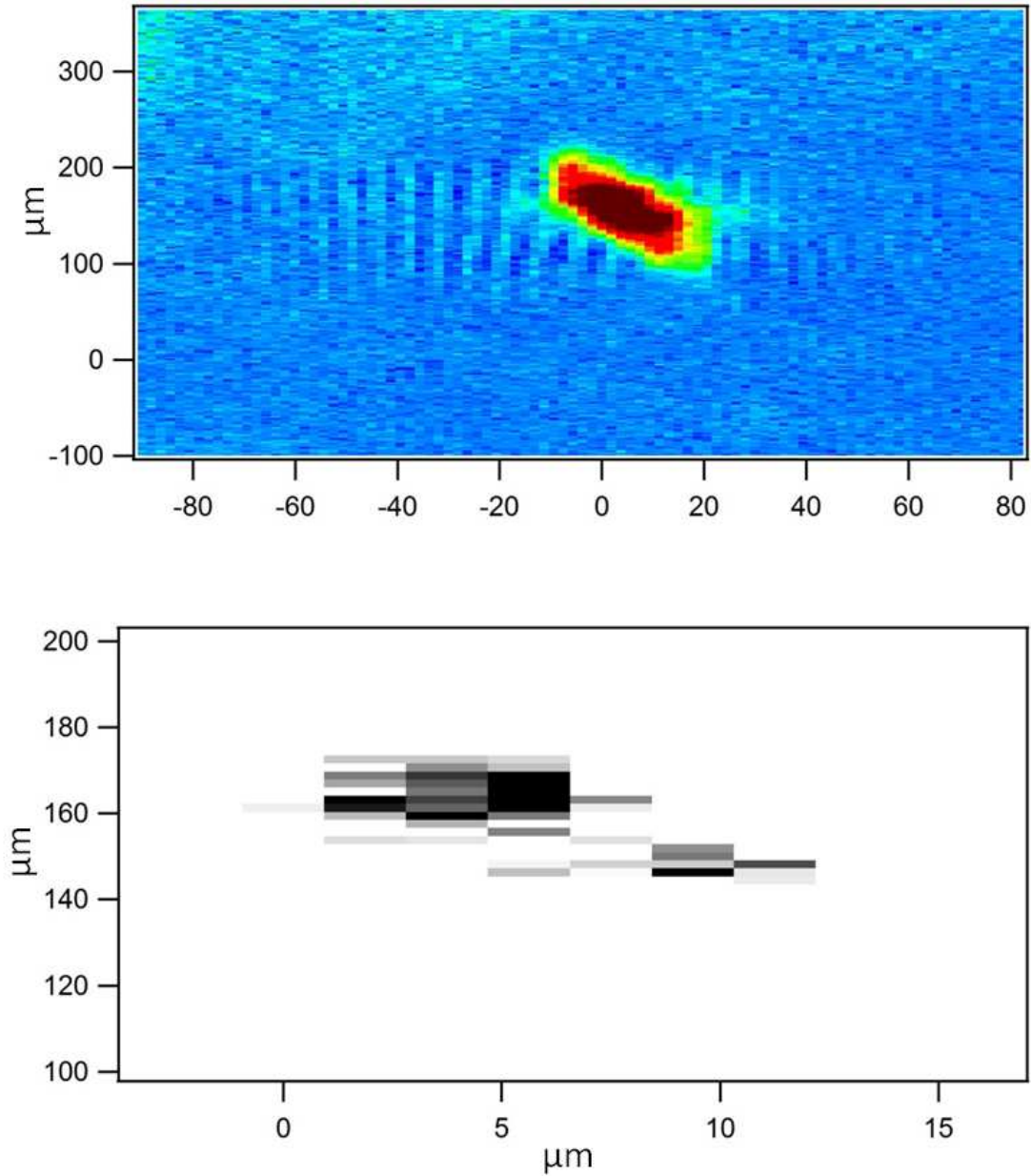


Figure 5.4: Absorption images after $10 \mu\text{s}$ expansion from $5.6 \mu\text{m}$ lattice. The top picture shows that the lattice (along with some diffraction) is visible on the camera over the extent of the cloud. The bottom image is zoomed in just on the center of the cloud, with darker colors indicating higher density. Two planes are visible in the zoomed image, with the majority of the density in just one. The centers of the planes are offset by $\sim 6 \mu\text{m}$ horizontally and $\sim 20 \mu\text{m}$ vertically. Vertical Gaussian fits on each plane have a $29 \mu\text{m}$ width.

nearly equal number of atoms into the two interfering planes. This also explains weird fringe patterns like in Fig. 5.5, as with few atoms in the second plane, we only get significant interference where the two clouds overlap, which changes from shot to shot. This problem is exacerbated by the long expansion times that we use so that the fringe period is above our imaging resolution. In addition, fewer atoms in the second plane might mean that we do not reach the densities required for the BKT phase transition in that plane on every shot.

One thing which must be addressed in this explanation of the tilted fringes is that the observed position offset of the clouds does not give tilted fringes in simulations of freely expanding Gaussian wavepackets. The fringe angle is set by the difference in the overall direction of the momentum vector between the two planes. Because the momentum is so high transverse to the planes, this simulation always yields fringes along the lattice direction. However, we cannot ignore the effect of interactions, which produce momentum along the planes. It is straightforward to do a calculation of our system in the opposite limit, ignoring the kinetic energy and considering only the interaction energy in the mean-field approximation [32]. In this case, the interactions do indeed produce tilted fringes (Fig. 5.6). However, we are not really in this limit. In the mean-field approximation, we can simulate our system including both interactions and kinetic energy using the Gross-Pitaevskii equation [116]. We are currently working on this simulation in order to verify the tilt in our system is not due to a systematic non-zero velocity, but rather due to interactions and the initial position offset.

In order to try to resolve the problems with fringe visibility, we decreased

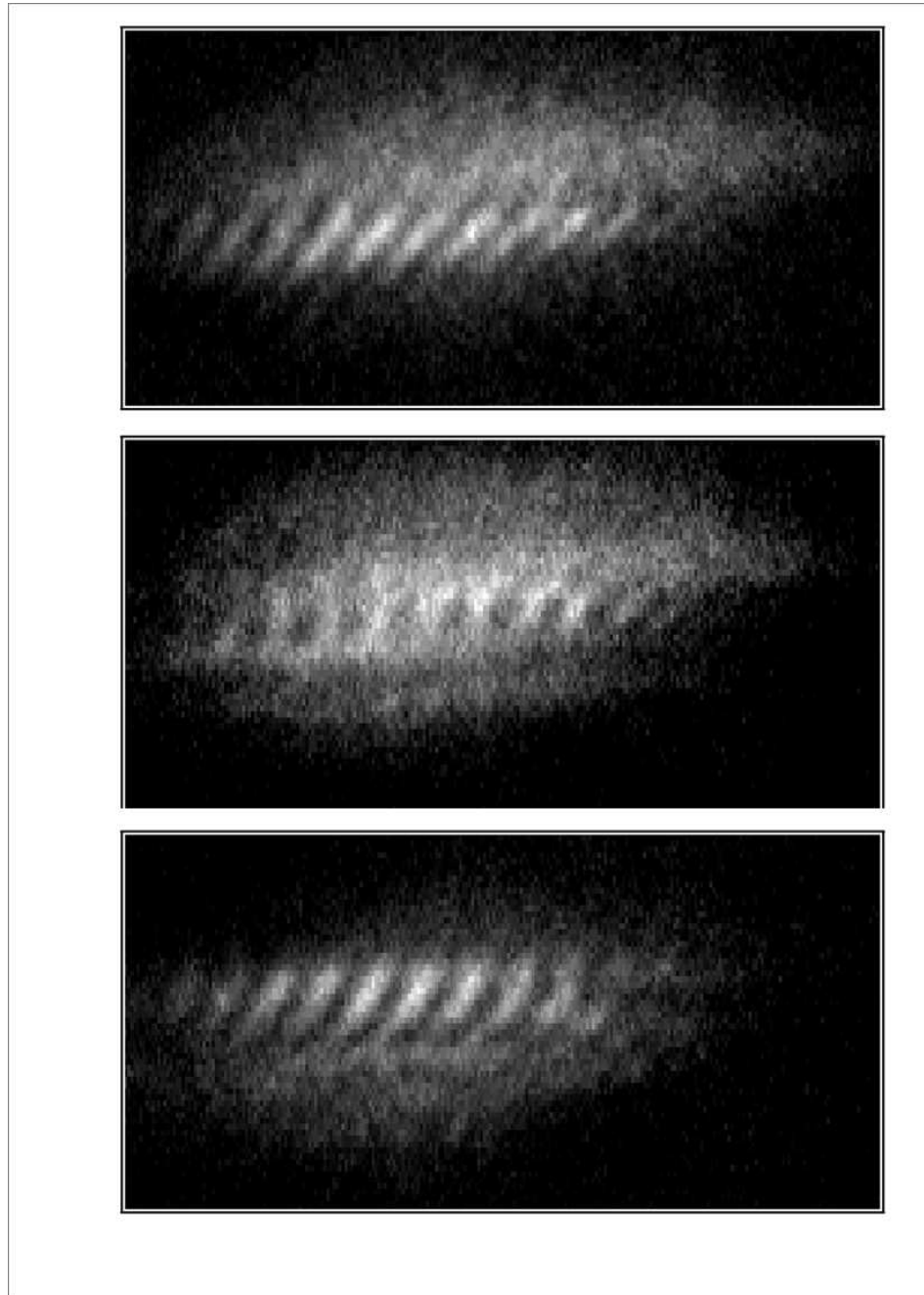


Figure 5.5: Absorption images of interference patterns after 37 ms expansion which do not extend over the whole cloud due to the lack of complete overlap between the two planes or lower density in the second plane.

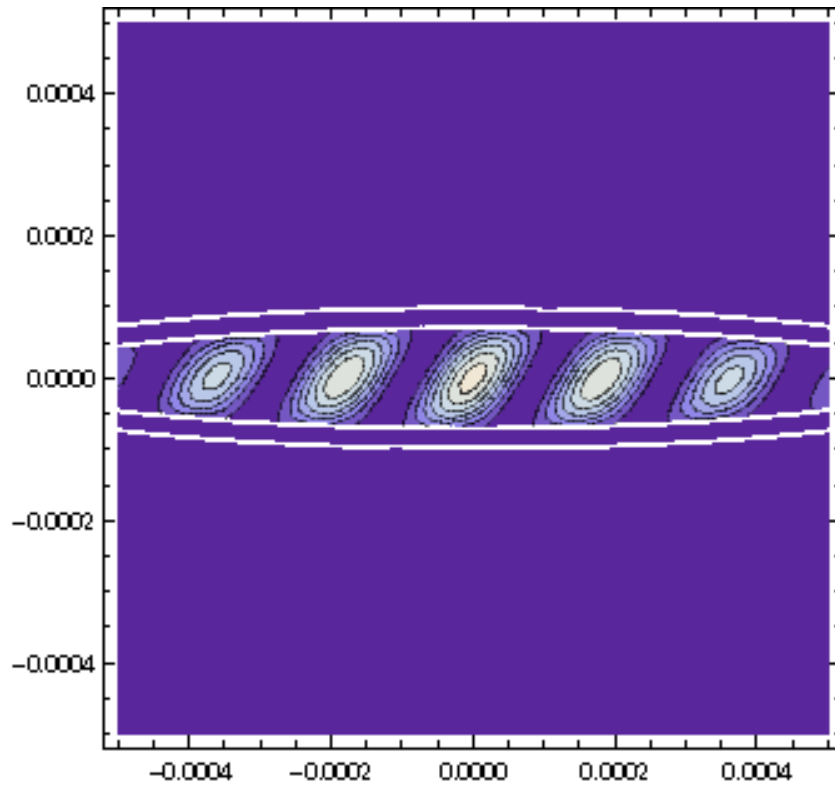


Figure 5.6: Calculated interference pattern of two 2D systems using system parameters similar to ours. Pattern is calculated after expansion using the Castin-Dum scaling [32]. In this simulation, the fringes tilt due to an initial position offset of the two planes.

the spacing of our lattice in order to more equally load two planes. Physically, we changed the focusing lens for the lattice beams and moved it closer to the atoms. With the same separation at the lens, this produces a larger angle between the beams, which gives a smaller spacing. This also means that the lattice frequency is higher at a lower value of the potential depth, so a neutral density filter was installed and the lattice was recalibrated. In addition, we moved the lattice frequency farther from resonance to 773 nm. With this configuration, the fringe pattern is much more stable, although it still sits at an average angle of $\sim 20^\circ$. The lattice spacing in this new configuration is approximately $2.6 \mu\text{m}$, which is smaller than the resolution of our imaging system, so we cannot directly image the lattice. We assume that the new spacing has decreased the offset along the planes. Example absorption images of this new setup after free expansion are shown in Fig. 5.7.

5.1.1 Analysis of Interference Patterns

The main quantities that we would like to extract from images such as those in Fig. 5.7 are fringe visibility and phase. In addition, we are often interested in temperature, atom number, and the ratio of atoms in each part of a bimodal distribution. These latter quantities can be determined from the methods described in Sec 3.9, with some small modifications described later.

If we label the axes of the images as shown in Fig. 5.7, with Z along the fringes and X along the cloud, then we can fit the profile $F(x, z)$ of the image with

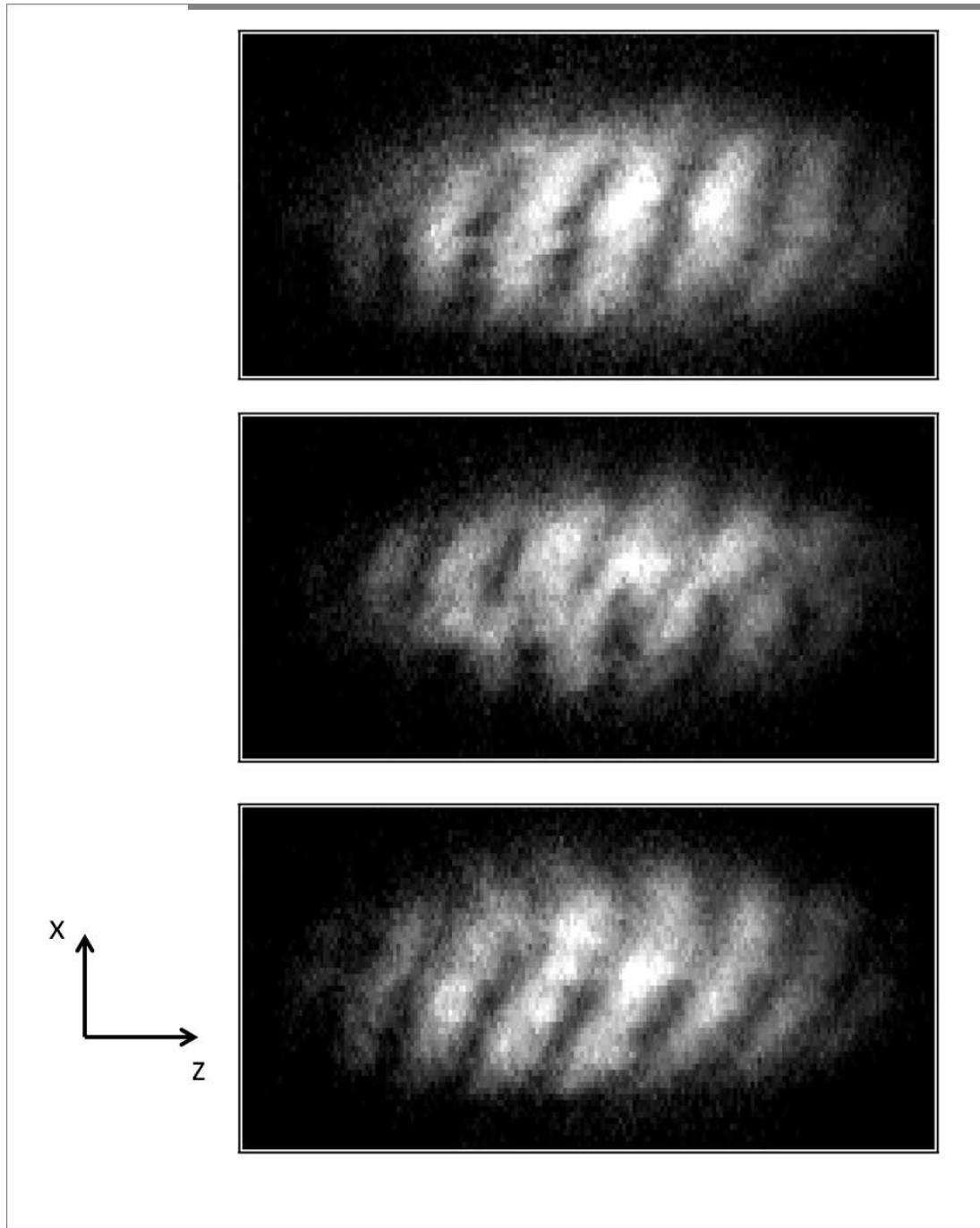


Figure 5.7: Absorption images after 26 ms of free expansion of two 2D systems from a $2.6 \mu\text{m}$ period lattice. Two planes are predominantly loaded in this configuration, with a small occupation of exterior planes. The image in the middle has a fringe dislocation, indicating a vortex, while the curves in the fringes indicate long-wavelength phonon-like excitations.

a function of the form

$$F(x, z) = A(x)e^{-\frac{z^2}{\sigma^2}} \left(1 + C(x)\text{Sin} \left(\frac{2\pi z}{D} + \phi(x) \right) \right), \quad (5.1)$$

with $D = \frac{ht}{md}$, as in Eq. 4.3. We are interested in the values of $C(x)$ and $\phi(x)$, which represent the fringe visibility and the phase of the interference pattern. The visibility is related to the coherence of the the two planes, and we are interested in the phase because the fringes are straighter at temperatures below the transition, producing a constant $\phi(x)$. In order to extract these, we do not directly fit the image. Rather, we perform two Fourier transforms, one a 2D transform and the other a series of 1D transforms of Z as a function of X (Fig. 5.8).

The 2D Fourier transform gives us the dominant angle of the fringes with respect to the axis of the lattice, which is still typically non-zero in all of our current images, and changes slightly from shot to shot. The peak in 2D Fourier space appears at an angle with respect to the axes of the image which is the same as the angle of the fringes. As mentioned previously, although the angle of the fringes changes from shot to shot, the projection of the frequency onto the Z-axis does not change, as it is set by the lattice spacing. If the angle changes, the fringe frequency changes in order to keep this projection the same. Therefore, the overall frequency of the fringes changes along with the angle, and the peak in the 2D transform in Fig. 5.8 moves up and down along the p_x axis of the image. We perform a 1D Gaussian fit of the peak in Fourier space along p_x in order to determine the angle of the fringes in every image. This will be used to find $\phi(x)$ accurately.

The 1D Fourier transform of a function of the form of Eq. 5.1 in the Z direction

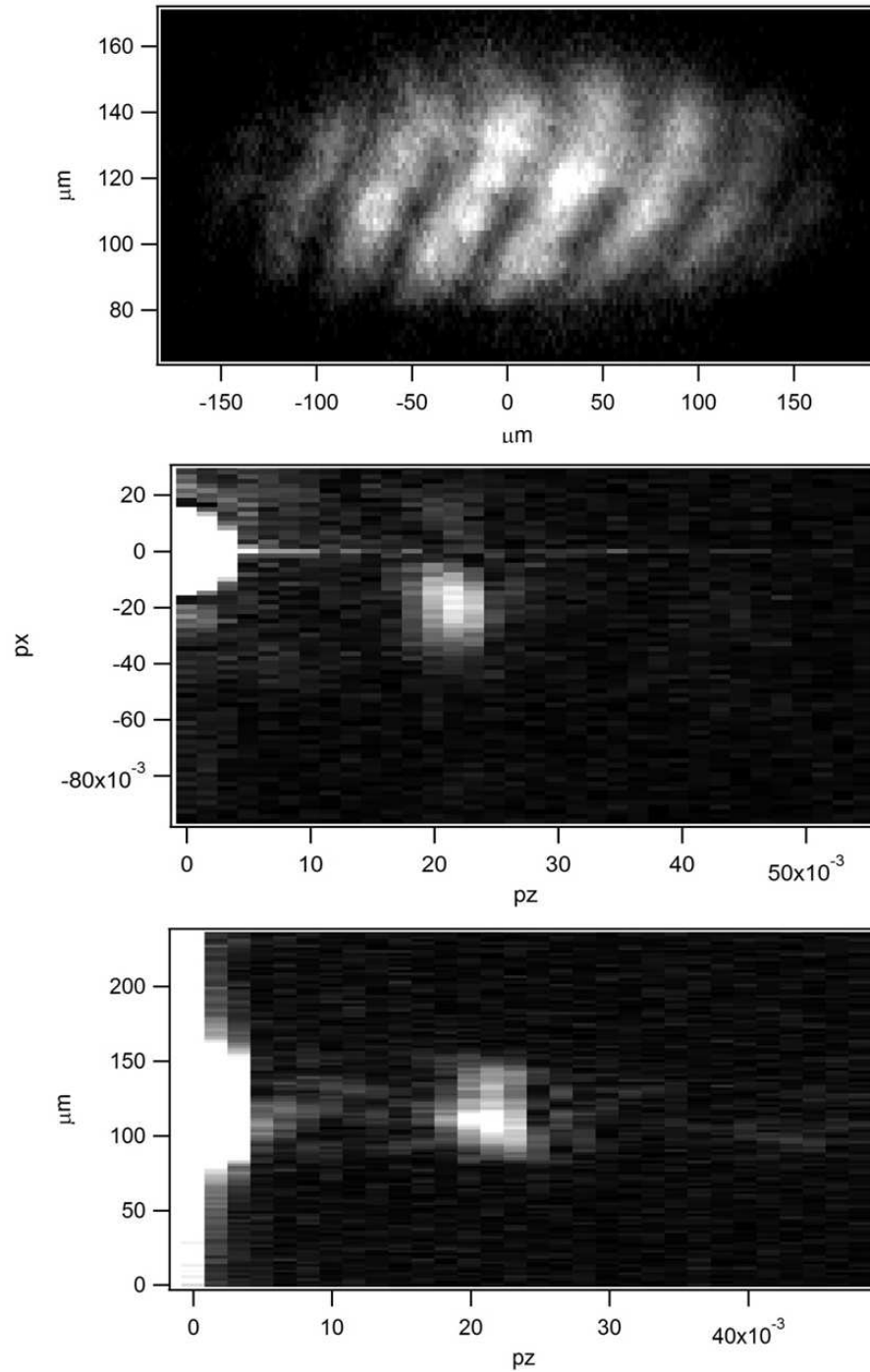


Figure 5.8: Absorption image after 26 ms of free expansion of two 2D systems from a $2.6 \mu\text{m}$ period lattice with both 2D (middle) and 1D (bottom) positive-spectrum Fourier transforms. The position of the peak in the 2D Fourier transform can be used to find the dominant fringe angle, while the peak in the 1D Fourier transform gives the visibility and phase of the interference pattern.

is

$$A(x) \frac{\sigma}{2\sqrt{2}} \left(2e^{-\frac{p_z^2 \sigma^2}{4}} + iC(x) \left(-e^{-\frac{(2\pi/D+p_z)^2 \sigma^2}{4} - i\phi(x)} + e^{-\frac{(2\pi/D-p_z)^2 \sigma^2}{4} + i\phi(x)} \right) \right). \quad (5.2)$$

Since we are interested in values of $C(x)$ and $\phi(x)$, we first observe that at $p_z=0$, Eq. 5.2 simplifies to

$$\frac{A(x)\sigma}{\sqrt{2}} \left(1 - C(x)e^{-\frac{(2\pi/D)^2 \sigma^2}{4}} \text{Sin}(\phi(x)) \right). \quad (5.3)$$

However, the exponential is negligible, and so the amplitude of the Fourier peak at $p_z=0$ is related only to the value of $A(x)$. Similarly, if we look at the peak at $p_z = \pm 2\pi/D$, we see that Eq. 5.2 simplifies to

$$\frac{\sigma}{2\sqrt{2}} \left(A(x)e^{-\frac{(2\pi/D)^2 \sigma^2}{4}} + iA(x)C(x)e^{-i\phi(x)} \left(e^{2i\phi(x)} - e^{-(2\pi/D)^2 \sigma^2} \right) \right). \quad (5.4)$$

Again the exponentials eliminate two of the three terms, leaving us with the peak value at $p_z = \pm 2\pi/D$ of

$$\frac{\sigma}{2\sqrt{2}} iA(x)C(x)e^{i\phi(x)}. \quad (5.5)$$

We can see then that dividing the value of the Fourier transform at $p_z = 2\pi/D$ by the value at $p_z = 0$ and multiplying by 2 gives us the value of $C(x)$. In addition, we see that Eq. 5.5 also allows us to calculate the value of the phase $\phi(x)$ by finding the phase angle of the peak.

The other way to find $C(x)$ and $\phi(x)$ is to do a fit to the cloud, which turns out to be very sensitive to the initial fitting parameters and guesses for the functional form of the observables. The analysis above is a simple fast Fourier transform plus some simple algebra, so it is much easier, with a few caveats. First, the peak at

$p_z = 2\pi/D$ is not a delta-function in Fourier space, so we have to know where that frequency sits exactly. Also, there is a finite step size in Fourier space, and if the true frequency lies in between two of these steps, which is almost inevitable, then the amplitude is split between two pixels. We do not know the actual position of this peak by any other method than observing it, so we actually sum two pixels to get the effective visibility. This probably overestimates the actual value of $C(x)$, but as a relative measure it should be consistent, and we are almost always interested in relative changes. The second subtlety of this analysis method is that our fringes are at an angle with respect to the axis of the 1D Fourier transform. This means that $\phi(x)$ has a linear part to it with the slope being the angle of the fringes. We account for this by finding the angle of the fringes in each image and then subtracting off this linear tilt from the phase. This produces the actual untilted $\phi(x)$.

The total analysis proceeds as follows: Each image is initially fitted with a Gaussian to represent the thermal fraction of the cloud. However, the expansion of the cloud in the tightly confined direction overlaps the thermal cloud in this direction, so the thermal fit is only done in the X-direction. Then, a bimodal fit is performed in the X-direction using the initially fit thermal parameters as guesses for the thermal cloud fit coefficients. Once this fit converges, the thermal coefficient values are used in the Z-direction, and a dual fit is done in this direction while not changing the thermal coefficients. This relies on the isotropic expansion of the thermal part of the sample, and allows us to fit the overall envelope of the thinner part of the bimodal distribution in both directions. Once this is performed, the analysis in Sec. 3.9 is used to extract the atom number in each part of the

distribution, as well as widths of each part, and the temperature of the ensemble. The analysis of visibility and phase can then be performed on just the thinner “condensed” part of the distribution, as described above.

Many of the images do not have a significant thermal fraction, and thus cannot be used in this type of analysis. When we report atom number and temperature, we have used only those images where the dual fit could be performed. In addition, correct calibration of atom number and temperature are difficult, especially in a lattice. There can be large systematic uncertainties, leading many experimental groups to just assume 10% error bars on these measurements. Our temperature measurement is even more inaccurate owing to its 1D nature. However, if we are interested in relative changes, then we expect that applying consistent methods should yield consistent relative results. If we are truly interested in an accurate measurement of the temperature and atom number, we must do a more careful job of calibrating our imaging system. $C(x)$ also suffers from absolute calibration error owing to our analysis method, while $\phi(x)$ may be slightly modified by the subtraction of the linear tilt. However, if we are only interested in visibility, we can make some gains against statistical error by performing a more-stable Gaussian fit on just the thinner portion of the cloud, ignoring the thermal component. We then find $C(x)$ and $\phi(x)$ on just this part, which allows us to increase the number of images that can be used for averaging these quantities.

5.1.2 BKT Transition in 2.65 μm Lattice

To verify that we can observe the BKT phase transition in a 2D Bose gas, we calibrated the lattice to have a depth $U_0/h = 1$ MHz, which gives an oscillation frequency in each well of $f_z = 18$ kHz. We create a 3D BEC at a variable temperature and then ramp the lattice on in 500 ms and hold for 200 ms to attempt to ensure equilibrium. We then turn off all of the potentials and image the interference pattern after 26.95 ms of free expansion, collecting images such as those in Fig. 5.7. These images are analyzed and quantities are extracted using the techniques given above in Sec. 5.1.1. Table 5.1 summarizes the parameters of the system for the data in the following sections.

The results are shown in Fig. 5.9. There are two different ways the data is analyzed. In either case, the integral of the visibility over the “condensed” part of the sample of length L is calculated:

$$V = \frac{1}{L} \int_0^L C(x) e^{i\phi(x)} dx. \quad (5.6)$$

For the top two plots, this is shown on the Y-axis. For the bottom two plots, $\phi(x)$ is assumed constant. The reason for this is that it is predicted and observed that as the BKT transition region is approached from below, the phase of the interference pattern exhibits more and more curvature [76]. This is indicated by the phase varying over the cloud. We see a small difference in the slopes of the two types of analysis, indicating that the phase curvature does reduce the growth of fringe visibility and coherence in Eq. 5.6. Each pair of plots shows both raw data and average binned data in 20 nK bins.

Table 5.1: 2D System Parameters

f_z	18 kHz
f_x	28 Hz
f_y	117 Hz
Number of Atoms Per Plane	50000
Temperature	35 nK
Chemical Potential in Each Plane μ_{BEC}	7 kHz
Thomas-Fermi Radius R_{TF_z}	70 nm
R_{TF_x}	45 μm
R_{TF_y}	11 μm
Angle between lattice beams	16.7°
Lattice spacing	2.65 μm
Lattice depth U_0/h	1 MHz
Harmonic Oscillator Length $l_z = \sqrt{\frac{\hbar}{m\omega_z}}$	80 nm
\tilde{g}	0.34
Critical Phase Space Density $D_c = \ln\left(\frac{380}{\tilde{g}}\right)$	7.0

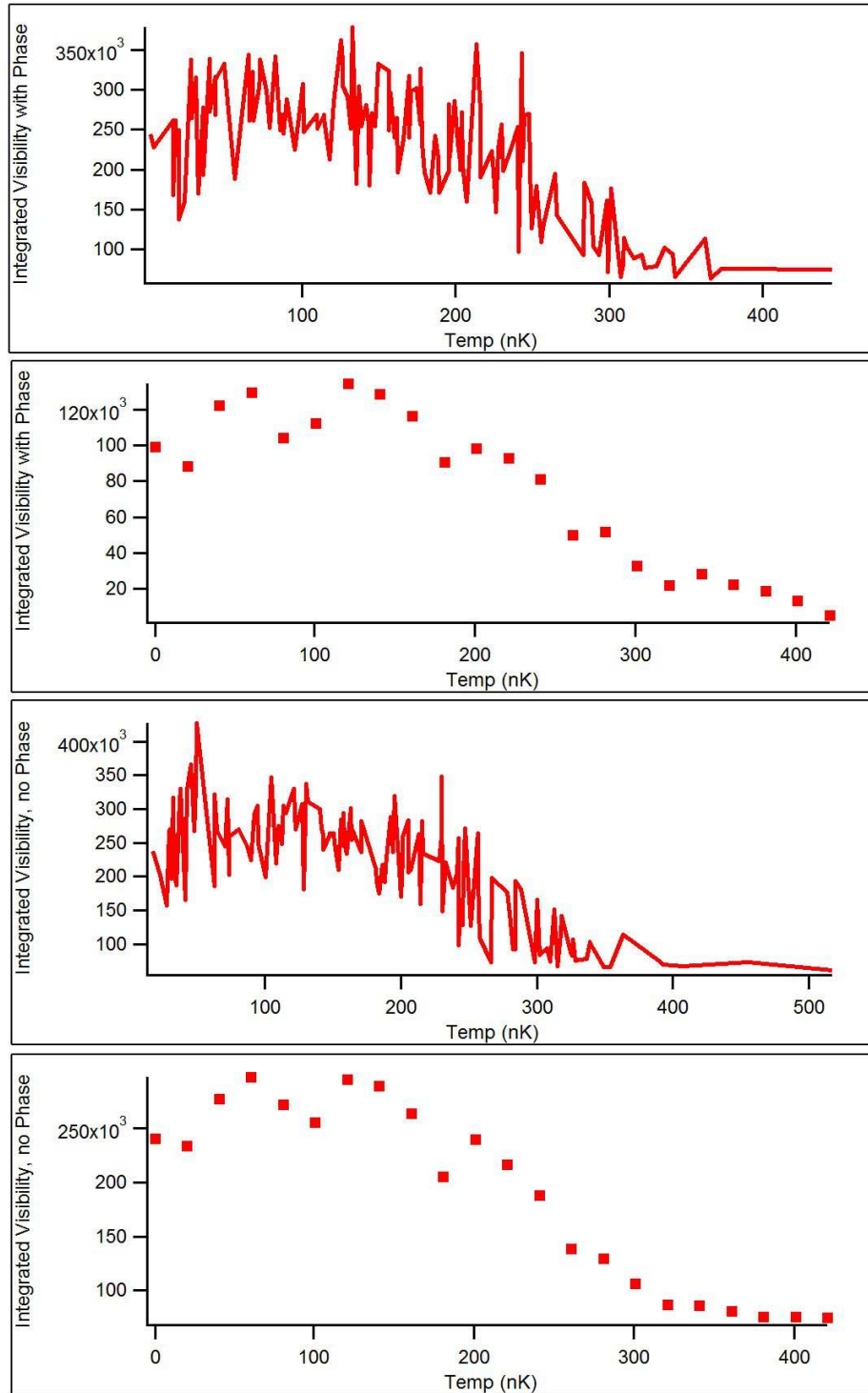


Figure 5.9: The visibility at different temperatures in the $2.65 \mu\text{m}$ lattice. In the top 2 plots, representing raw (top) and 20 nK binned average data, the visibility is calculated using Eq. 5.6, while the bottom two plots assume a constant $\phi(x)$ in the integral calculation.

The data indicates that as the temperature decreases lower than ~ 300 nK, the visibility of the fringes slowly grows, leveling at ~ 175 nK. This is similar to the results seen in Ref. [76], and is a strong indication that we are observing the BKT phase transition.

5.2 2D Systems with Disorder

We see from Fig. 5.9 that there is a range of temperatures over which the visibility is fairly insensitive to temperature changes. In order to observe the effects of disorder in our system, we evaporated to this temperature range and then followed a similar procedure as above. This time, both the speckle disorder potential and the lattice are ramped on at the same time. Typical images are shown in Fig. 5.10. As the disorder gets stronger, the visibility decreases and the sample starts to look more disordered overall. Similar to Fig. 4.8, the axis of the speckle beam is horizontal, so the predominant effect of the speckle is in the vertical direction. A systematic study of the changes in the atomic cloud is shown in Figs. 5.11 and 5.12.

Fig. 5.11 shows that as the speckle depth is increased, the number of atoms in the thermal part of the distribution increases while the number of atoms in the “condensed” part of the distribution decreases. The temperature seems to stay constant. There is a significant effect on these quantities even when the disorder strength is much lower than the chemical potential in each plane, indicating that we are not just “fracturing” the BEC. It should be noted that there were many images in this data set with no significant thermal fraction, especially at low speckle

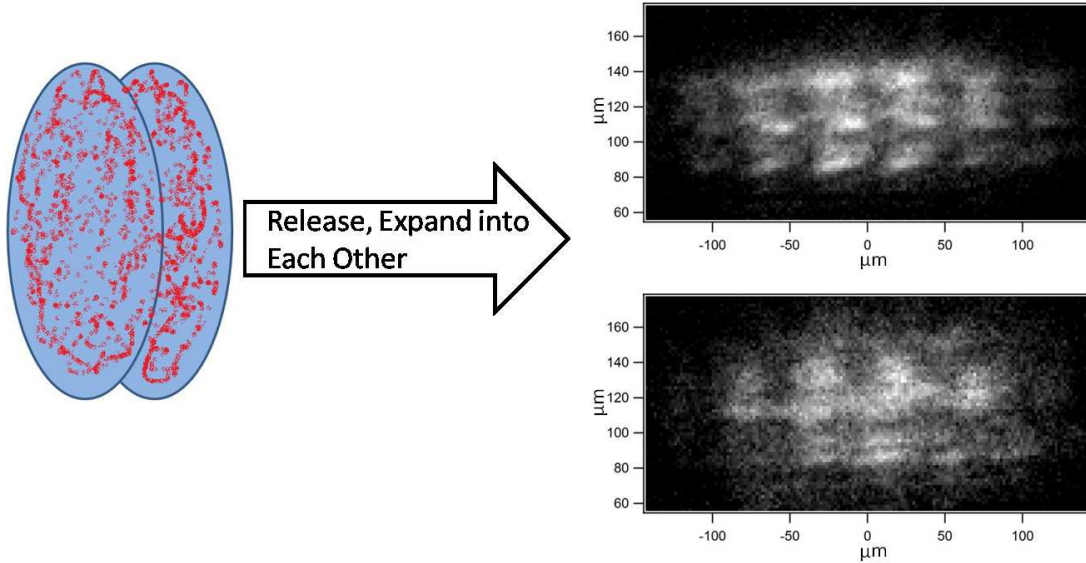


Figure 5.10: Typical absorption images of 2D systems in the presence of speckle disorder after 27 ms of expansion. The top image is at a speckle depth of $U_0/h = 750$ Hz, while the bottom image has $U_0/h = 4$ kHz.

depths. For the purposes of measuring temperature and number, these images were not used, as we do not have a good method to measure the number of thermal atoms or the temperature in these pictures. Thus, the number of points used in averaging at each speckle depth in Fig. 5.11 is as low as 10, but as high as 30 at the higher speckle depths.

Fig. 5.12 shows that as the disorder depth increases, the integrated visibility, with or without assuming a constant $\phi(x)$, decreases. These fits were not bimodal fits, and thus the error bars are standard deviations of at least 35 images in each case. We assume from the constant temperature data shown in Fig. 5.11 that even in images where the temperature could not be measured due to little or no thermal fraction, the temperature was still not significantly different from the images with measurable temperatures. Again, we note a significant effect of the disorder on the

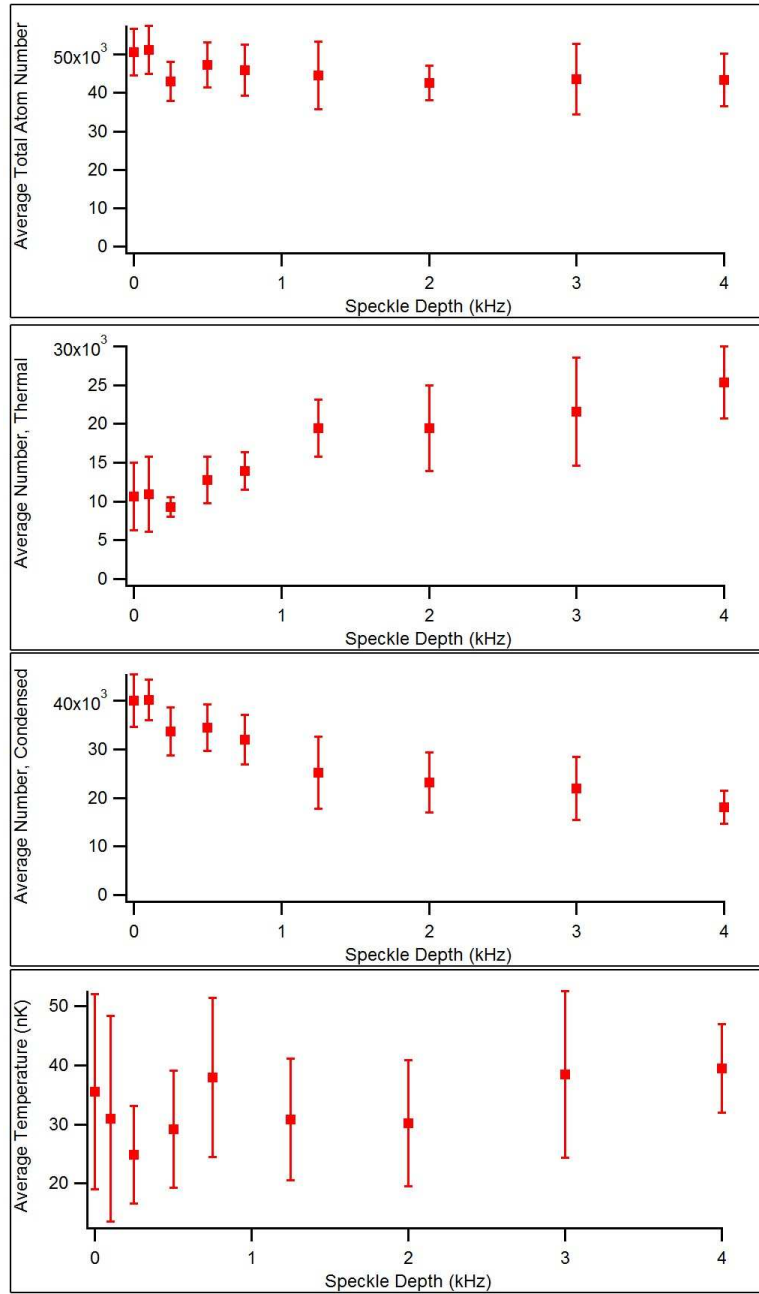


Figure 5.11: Number of thermal atoms, condensed atoms, total atom number, and temperature as a function of disorder strength in the $2.65 \mu\text{m}$ lattice. Error bars are one standard deviation of the measurements at each disorder strength.

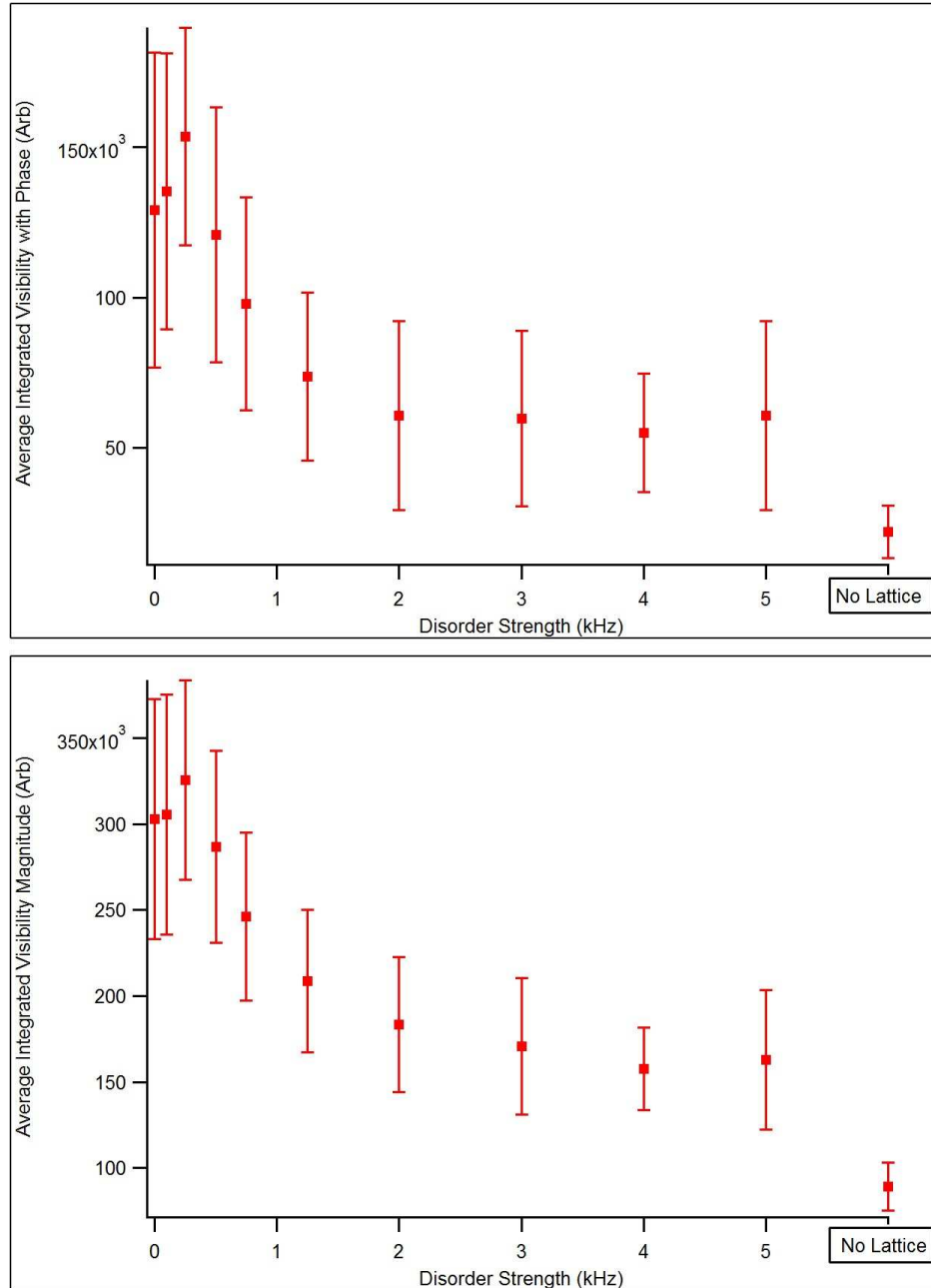


Figure 5.12: The visibility at different disorder strengths in the $2.65 \mu\text{m}$ lattice. The visibility is calculated using Eq. 5.6 in the top plot, while the bottom plot assumes a constant $\phi(x)$ in the integral calculation. Error bars are the standard deviations of at least 35 images at each disorder strength. “No lattice” indicates the visibility calculated this way with zero visibility in the interference pattern, using images with 0 lattice depth.

visibility at strengths of 500 Hz - $1/14$ of the chemical potential in each plane. Only a small amount of disorder produces a significant effect.

One other thing that must be addressed is the role of vortices in this system. As we have seen, vortices do appear in our interference patterns, and we would like to know how the disorder affects them. As seen in the middle column of Fig. 5.13, the phase of the fringes does not seem to change across disorder-induced valleys in the visibility along the X-axis. However, vortices still appear in some images, as the right column in Fig. 5.13 shows. Vortices can be counted by looking at the phase of the interference pattern across the cloud and looking for jumps in the phase. This was done for two cases; 8 out 37 images with zero disorder and 10 out of 36 images with 750 Hz disorder strength contained a vortex. If we assume that vortex appearance follows a binomial distribution, then the probability of observing either number of vortices is consistent with a true vortex probability of 25.2%. Thus, it seems that the disorder has little effect on the probability of observing a vortex. However, a more systematic way of counting vortices must be developed, and more images must be taken to get better statistics on the number of vortices observed.

The decrease of both the number of atoms in the condensed part of the bimodal distribution and the visibility of interference fringes are consistent with a decrease in the coherence in the system, but theoretical support will be necessary to work out the subtleties of exactly what is happening microscopically. It is unclear from the data taken so far whether the disorder has any effect on the vortices appearing near the BKT phase transition. We need to take more data at different temperatures to discern if the suppression of visibility occurs at the same disorder strength, and

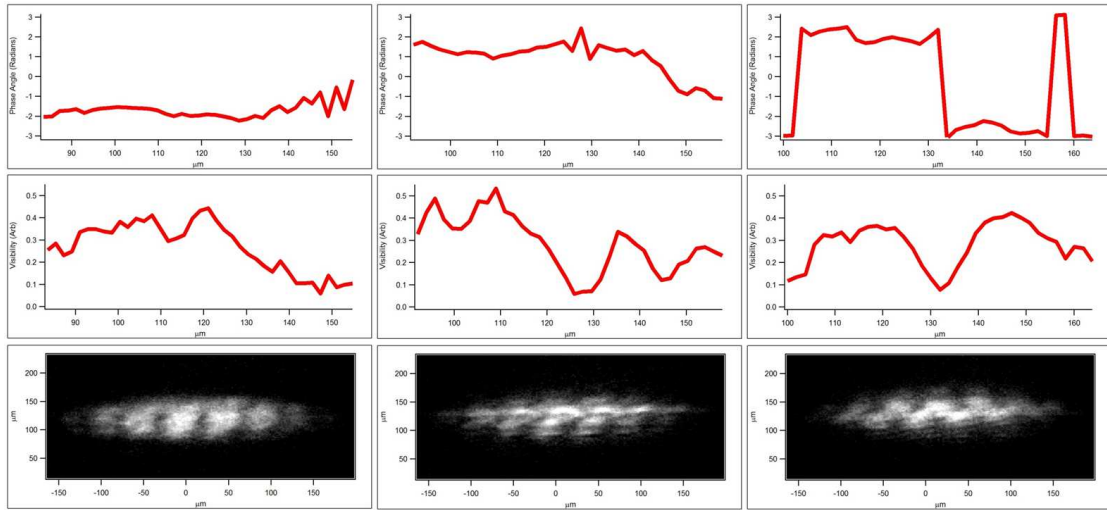


Figure 5.13: Each column shows an absorption image after 26.95 ms expansion from the $2.65 \mu\text{m}$ lattice, as well as a vertical cut of the visibility (middle) and phase (top) of the interference pattern across the sample. The image on the left has no disorder, with a nearly constant phase where the visibility is high. The image in the middle has 750 Hz disorder strength, and the phase still seems nearly constant across the cloud. The image on the right is also at 750 Hz disorder strength, but this time a vortex is indicated by the π phase shift and loss of visibility near the center of the cloud.

try to determine a critical temperature as a function of disorder strength. We should explore higher disorder strengths to see where the fringe visibility completely vanishes, perhaps at strengths near the chemical potential in each plane. In addition, we need to take more images and develop a more systematic way of counting vortices to see if the disorder affects the vortex statistics.

5.3 Conclusions

We have designed and built a system to study the effect of disorder in ultracold 2D bose gases. According to many models, this system should mimic the behavior of high- T_c superconductors under the Cooper pairing temperature. 2D superfluid systems exhibit a phase transition to a normal fluid at a critical temperature which is expected to be analogous to the superconductor to insulator transition in high- T_c superconductors, where the fluid is formed of Cooper pairs. The BKT mechanism of the unbinding of vortex pairs is expected to drive this phase transition, and because disorder strongly effects vortex transport in high- T_c superconductors, we expect disorder to strongly affect this phase transition.

Experimentally, we create two 2D bose gas systems with a controllable temperature and atom number. We observe the experimental signature of the BKT phase transition in this system as the appearance of an interference pattern and bimodal distribution in the overlap region of the two systems during free expansion. In addition, the microscopic mechanism of the BKT phase transition is revealed by phase jumps in the interference pattern which indicate vortices in the system.

The addition of disorder while deforming the system from 3D to 2D smoothly reduces both the visibility of the interference pattern and the proportion of atoms in the “condensed” part of the bimodal distribution. Disorder strengths much smaller than the chemical potential of the systems still have a noticeable effect on these quantities. The number of vortices observed in repeated measurements does not seem to be effected by the disorder. More work, including a theoretical treatment of our system, will be necessary to fully characterize what these observations mean. The apparatus is now in a good position to carry on further work in the area of disordered 2D ultracold gases.

Appendix A

Digital and Analog Outputs

Table A.1: Digital Outputs

Digital Channel Number	Equipment Controlled
0	Zeeman slower shutter
1	IGBT for x bias Coils
2	RF scan trigger
3	IGBT for y bias coils
4	MOT shutter
5	AOM for Optical Pumping
6	Repumper shutter
7	UMOT IGBT/Dipole trap shutter
8	Z-wire IGBT
9	Ti-Saph shutter
10	Probe AOM
11	Optical pumping shutter
12	Second probe shutter
13	z-coil (Bottom) IGBT
14	Ti-Saph AOM #1

15	Hardware Reset for RF
16	Slower repumper shutter
17	60 Hz filters for magnetic trap
18	Dipole trap AOM
19	Ti-Saph AOM #2 and #3
20	Stage movement trigger
21	1st Probe shutter
22	Camera trigger
23	Analog cards trigger

Table A.2: Analog Outputs

Analog Channel Number	Rack Breakout #	Equipment Controlled
Device 1 (PCI)		
0	16	U-Wire
1	4	Rydberg E-field
2	15	AOM #1 (Ti-Saph)
3	3	Z Bias Coil (Bottom of Chamber)
4	14	Not in Use
5	2	Trim Coils
6	13	MOT AOM Frequency
7	1	Probe AOM Frequency

Device 2 (PCI)

0	24	Optical Pumping Frequency
1	12	IPG AOM Amplitude
2	23	Not in Use
3	11	RF Power
4	22	Ball Valve Motor
5	10	Slower Detuning
6	21	AOM #3 (Ti-Saph)
7	9	AOM #2 (Ti-Saph)

Device 3 (USB)

0	X-Bias Coils
1	Z-Wire
2	Y-Bias Coils
3	IPG EOM

Appendix B

1D Gross-Pitaevskii Equation Solution

In our previous publication [54], we did some calculations which solved the Gross-Pitaevskii equation (GPE) [46, 116]. This appendix details how these calculations were done.

The GPE equation has been extremely successful at describing the behavior and dynamics of near zero-temperature condensates commonly produced in experiments. It is similar to the linear Schrödinger equation, with the addition of a nonlinear term which takes into account the interactions between the atoms in a mean-field approximation. Thus, it is single particle solution that includes a term accounting for how all of the other particles affect the particle being simulated. Since all of the particles in a BEC are in the same state, simulating the dynamics of one particle in this way describes the behavior of all of the particles.

The GP equation takes the form

$$i\hbar\frac{\partial\psi(\mathbf{r},t)}{\partial t} = -\frac{\hbar^2}{2m}\nabla^2\psi(\mathbf{r},t) + V(\mathbf{r})\psi(\mathbf{r},t) + NU_0|\psi(\mathbf{r},t)|^2\psi(\mathbf{r},t), \quad (\text{B.1})$$

where $\mathbf{r} = (x, y, z)$ is the three-dimensional position vector, t is time, $\psi(\mathbf{r}, t)$ is the order parameter describing the particle, $V(\mathbf{r})$ is the potential the particles experience, m is the mass of one of the atoms, and N is the number of atoms. U_0 describes the strength of the interactions between the atoms as

$$U_0 = \frac{4\pi\hbar^2 a}{m}, \quad (\text{B.2})$$

with a the s-wave scattering length between the atoms. The wave function in this case is normalized to 1:

$$\int_{\mathbb{R}^3} |\psi(\mathbf{r}, t)|^2 d\mathbf{r} = 1. \quad (\text{B.3})$$

Our solution to the GP equation follows the recipe given in Ref. [13]. The equation is solved using the time-spectral splitting algorithm that works by breaking the Hamiltonian into two parts, the part that commutes with the momentum operator and the part that commutes with the position operator. Typical quantum mechanical propagators for each part are assigned separately. A small time step Δt is taken with the position propagator operating on an initial guess for the order parameter $\psi(\mathbf{r}, 0)$. Then, a Fast Fourier Transform (FFT) is performed on $\psi(\mathbf{r}, \Delta t)$, followed by operating the momentum part of the propagator for Δt on the transformed ψ . The inverse FFT is performed, and then the position operator is applied for another step of Δt , and then these three steps are repeated. Because ψ commutes with the Hamiltonian in both position and momentum due to the FFT, propagation is simply multiplication by a number in each case. If Δt is kept small, the error in time propagation using this method can be made small.

We use this method to both find the ground state of atoms in a lattice and simulate the process of turning on a lattice potential on the BEC. We can use an imaginary time propagation algorithm to easily find the ground state of the system [37]. The idea behind this is that the energy of the ground state is the smallest energy in the problem. If we change the time t in Eq. B.1 to it , the propagator will cause all of the eigenstates in the problem to decay in imaginary time, with the

decay constant set by the energy of each eigenstate. Because the ground state is the lowest energy, it will be the only one to have any amplitude after a long imaginary time, and thus propagation in imaginary time converges to the ground state and ground energy of the system.

Although our system does not fulfill the criterion for being one-dimensional, for the problems we are considering, all of the dynamics are happening in the direction of the applied 1D incommensurate lattices. Therefore, in order to make the problem more tractable, we reduced the 3D GP equation to its 1D counterpart. In addition to the assumption of separability, this reduction also requires assuming density distributions in the two directions not being simulated, and then using those to calculate a new 1D coefficient for the nonlinear term in Eq. B.1. In addition, to make the calculation easier, all of the variables are scaled in order to make the computation easier. Our particular scaling uses the lattice wavevector as the length scale, but the basic method for determining the scaling comes from [13].

Our potential energy $V(\mathbf{r})$ is

$$V(\mathbf{r}) = \frac{m}{2}(\omega_x^2 x^2 + \omega_y^2 y^2 + \omega_z^2 z^2) + V_0 \text{Sin}^2(kx), \quad (\text{B.4})$$

with the ω_i 's the harmonic trapping frequencies and the Sine function representing the lattice. Let us assign new scaled variables in Eq. B.1 as follows:

$$\tilde{\mathbf{r}} = \mathbf{r}k, \quad \tilde{t} = \omega_R t, \quad \tilde{\psi}(\tilde{\mathbf{r}}, \tilde{t}) = k^{-3/2} \psi(\mathbf{r}, t), \quad (\text{B.5})$$

with $\omega_R = \frac{\hbar k^2}{2m}$. With these substitutions, Eq. B.1 becomes

$$i \frac{\partial \tilde{\psi}(\tilde{\mathbf{r}}, \tilde{t})}{\partial \tilde{t}} = \left(-\nabla^2 + \frac{1}{4\omega_R^2} (\omega_x^2 \tilde{x}^2 + \omega_y^2 \tilde{y}^2 + \omega_z^2 \tilde{z}^2) + \frac{V_0}{E_R} \text{Sin}^2(\tilde{x}) + \kappa |\tilde{\psi}(\tilde{\mathbf{r}}, \tilde{t})|^2 \right) \tilde{\psi}(\tilde{\mathbf{r}}, \tilde{t}), \quad (\text{B.6})$$

where $E_R = \frac{\hbar^2 k^2}{2m}$ and $\kappa = \frac{NU_0 k^3}{E_R}$. From this point on, I will drop the “tilde” on the scaled variables to make the notation cleaner.

We assume that the dynamics in the y and z directions can be ignored, and we separate the order parameter, kinetic energy, and potential energy parts of Eq. B.6 into three parts, one for each direction, and we ignore the y and z equations. However, we need to scale the nonlinear interaction term for use in the 1D equation for the x variable, since it cannot be separated out. We do this by defining a 1D interaction coefficient

$$\kappa_{1D} = \kappa \int_{\mathbb{R}^2} \psi_{23}^4(y, z) dy dz, \quad (\text{B.7})$$

where

$$\psi_{23}(y, z) = \left(\int_{\mathbb{R}} |\phi_g(x, y, z)|^2 dx \right)^{1/2} \quad (\text{B.8})$$

is the x-trace of the ground state position density $|\phi_g(x, y, z)|^2$. For $|\phi_g(x, y, z)|^2$, we use the ground state Thomas-Fermi approximation for the atoms in a harmonic trap (Eq. B.6 minus the Sine term):

$$\psi_g(x, y, z, t) = \phi_g(x, y, z) e^{-i\mu t} = \sqrt{\frac{1}{\kappa} \left(\mu - \frac{1}{4\omega_R^2} (\omega_x^2 x^2 + \omega_y^2 y^2 + \omega_z^2 z^2) \right)} e^{-i\mu t}, \quad (\text{B.9})$$

with μ the chemical potential of the atoms. Before the lattice is turned on, this is expected to be the state of our system. Normalization of ψ_g gives

$$\mu = \left(\frac{15\kappa\omega_x\omega_y\omega_z}{64\pi\omega_R^3} \right)^{2/5}, \quad (\text{B.10})$$

so that we plug Eq. B.10 into Eq. B.9, then plug that solution into Eq. B.8, and finally use Eq. B.7 to find

$$\kappa_{1D} = \frac{5\kappa \left(\frac{5}{2\pi}\right)^{3/5} \omega_y \omega_z}{8\omega_R^2 \left(\frac{3\kappa\omega_x\omega_y\omega_z}{\omega_R^3}\right)^{2/5}}. \quad (\text{B.11})$$

With the value of κ_{1D} , we can now simulate our system by applying the time splitting spectral method to the 1D GP equation

$$i \frac{\partial \psi(x, t)}{\partial t} = -\nabla^2 \psi(x, t) + \left(\frac{1}{4\omega_R^2} \omega_x^2 x^2 + \frac{V_0}{E_R} \text{Sin}^2(kx) \right) \psi(x, t) + \kappa_{1D} |\psi(x, t)|^2 \psi(x, t). \quad (\text{B.12})$$

An algorithm to do this, written in Matlab, is included in Appendix C, and was used to do the calculations in Ref. [54].

Appendix C

1D Gross-Pitaevskii Equation Solver in MATLAB

```
function [Psi3, Energy] =
```

```
evolvestrang(Ntau, N, tau, Lx, Psi0, Ux, Uxtime, U0, J)
```

```
%{
```

This function does time evolution or ground state wave function calculations in 1D using a split step operator method, using a fast fourier transform to switch between momentum space and position space. This makes the operators very easy to deal with.

It includes a ψ^2 term for modeling the Gross-Pitaevskii equation, and allows a linear ramp of part of the x-dependent potential (Uxtime). The momentum operator is defined in this function, and may need to be changed depending on the units scaling that is done. The variable J determines whether the function does time propagation (J=i) or imaginary time evolution to find the ground state wave function (J=1). The nonlinear term is calculated using a predictor-corrector loop, taking a time step, calculating the wave function, and using the average of the new ψ^2 and the old ψ^2 to actually take the time step.

```

%}

deltax=Lx./(2.*N-1); %x step size

deltak=2*pi/(Lx); %momentum step size

x=(-N:1:(N-1)).*deltax; %x array

k=(-N:1:(N-1)).*deltak; %momentum array

ks=fftshift(k);

%move zero order momentum component to beginning of array

%Normalize Psi0

Psi0=Psi0./sqrt(sum(abs(Psi0).^2).*deltax);

tic %timing

Jtau=J.*tau; %time step (real or imaginary, depending on J)

Up=ks.^2; %Kinetic energy operator

%Build time evolution functions

Uxtau=Ux.*Jtau;

Uxtautime=Uxtime*Jtau;

Uptau=Up.*Jtau;

U0tau=U0*Jtau;

%Initialize energy array

```

```

Energy = zeros(1, Ntau);

PotEnergy=zeros(1,Ntau);

KinEnergy=zeros(1, Ntau);

%Plot initial wave function

figure(1);

plot(x, abs(Psi0).^2);

axis([-100 100 0 1]);

axis 'auto y';

%If statement to avoid unnecessary normalization if doing

%time evolution

if J==1

    %Ground state evolution Loop

    for II=0:1:(Ntau-1)

        Psistar=exp(-(Uxtau+Uxtaume*II...
+U0tau*abs(Psi0).^2)/2).*Psi0;

        Psistarstar =ifft(exp(-Uptau).*fft(Psistar));

        %Kinetic Energy (momentum space)

        Psi3=exp(-(Uxtau+Uxtaume*II...
+U0tau*abs(Psistarstar).^2)/2).*Psistarstar;

        %position space

        Psi3=Psi3./sqrt(sum(abs(Psi3).^2).*deltax);

        %Normalize

```

```

KinEnergy(II+1)=sum(abs(fft(Psi3)).^2.*Up)...
./sum(abs(fft(Psi3).^2));

PotEnergy(II+1)=sum(abs(Psi3).^2.*(Ux+Uxtime*II)...
+U0.*abs(Psi3).^4).*deltax;

Energy(II+1)=KinEnergy(II+1)+PotEnergy(II+1);

%Calculate some sort of energy,
although this is not true energy

Psi0=Psi3;

end

```

```
elseif J==i
```

```

for II=0:1:(Ntau-1)

    Psistar=exp(-(Uxtau+Uxtautime*II...
+U0tau*abs(Psi0).^2)/2).*Psi0;

    Psistarstar =ifft(exp(-Uptau).*fft(Psistar));

    %Kinetic Energy (momentum space)

    Psi3=exp(-(Uxtau+Uxtautime*II+U0tau...
*abs(Psistarstar).^2)/2).*Psistarstar;

    %position space

    Energy(II+1)=sum(abs(fft(Psi3)).^2.*Up)...
./sum(abs(fft(Psi3).^2))+sum(abs(Psi3).^2...
.*(Ux+Uxtime*II)+U0.*abs(Psi3).^4).*deltax;

```

```

    %Calculate some sort of energy, although this is not true energy

    KinEnergy(II+1)=sum(abs(fft(Psi3)).^2.*Up)...

    ./sum(abs(fft(Psi3).^2));

    PotEnergy(II+1)=sum(abs(Psi3).^2.*(Ux+Uxtime*II)...

    +U0.*abs(Psi3).^4).*deltax;

    Energy(II+1)=KinEnergy(II+1)+PotEnergy(II+1);

    Psi0=Psi3;

end

else

    'Incorrect J value'

end

toc

%plot final wavw function

figure(2);

plot(x, abs(Psi3).^2);

axis([-100 100 0 1]);

axis 'auto y';

%plot energy array

figure(3);

plot(Energy)

figure(4)

```

```
plot(KinEnergy)
figure(5)
plot(PotEnergy)
%plot momentum distribution
figure(6);
plot(k,abs(fftshift(fft(Psi3)).^2...
./(sum(abs(fft(Psi3).^2)*deltak)));
axis([-6 6 0 1]);
axis 'auto y';
```

Bibliography

- [1] D. W. Snoke A. Griffin and A. Stringari, editors. *Bose Einstein Condensation*. Cambridge University Press, 1995. 1.2
- [2] A.A. Abrikosov. On the magnetic properties of superconductors of the second group. *Soviet Physics JETP*, 5(6):1174–1182, 1957. 1.2
- [3] Sadhan K. Adhikari. Quantum scattering in two dimensions. *American Journal of Physics*, 54(4):362–367, 1986. 1.3.2
- [4] Alberto Amo, Jerome Lefrere, Simon Pigeon, Claire Adrados, Cristiano Ciuti, Iacopo Carusotto, Romuald Houdre, Elisabeth Giacobino, and Alberto Bramati. Superfluidity of polaritons in semiconductor microcavities. *Nature Physics*, 5(11):805–810, NOV 2009. 1.2
- [5] P. W. Anderson. Absence of diffusion in certain random lattices. *Phys. Rev.*, 109(5):1492–1505, Mar 1958. 1.4
- [6] Philip W Anderson. Superconductivity in high t/c cuprates: The cause is no longer a mystery. *Physica Scripta*, 2002(T102):10, 2002. 1.2
- [7] M. R. Andrews, M.-O. Mewes, N. J. van Druten, D. S. Durfee, D. M. Kurn, and W. Ketterle. Direct, nondestructive observation of a Bose Condensate. *Science*, 273(5271):84–87, 1996. 3.9
- [8] M. R. Andrews, C. G. Townsend, H.-J. Miesner, D. S. Durfee, D. M. Kurn, and W. Ketterle. Observation of interference between two Bose Condensates. *Science*, 275(5300):637–641, 1997. 4.3
- [9] Neil W. Ashcroft and N. David Mermin. *Solid State Physics*. Brooks Cole, first edition, 1976. 4.3
- [10] S. Aubry and G André. Analyticity breaking and Anderson localization in incommensurate lattices. *Ann. Israel Phys. Soc.*, 3:133, 1980. 1.4
- [11] Vanderlei Bagnato and Daniel Kleppner. Bose-Einstein condensation in low-dimensional traps. *Phys. Rev. A*, 44(11):7439–7441, Dec 1991. 1.3, 1.3.1
- [12] Karén G. Balabanyan. Effect of disorder on the superfluid transition in two-dimensional systems. *Phys. Rev. B*, 75(14):144512, Apr 2007. 1.5
- [13] Weizhu Bao, Dieter Jaksch, and Peter A. Markowich. Numerical solution of the Gross-Pitaevskii equation for Bose-Einstein condensation. *Journal of Computational Physics*, 187(1):318 – 342, 2003. B

- [14] Thomas E. Barrett, Samuel W. Dapore-Schwartz, Mark D. Ray, and Gregory P. Lafyatis. Slowing atoms with σ^- polarized light. *Phys. Rev. Lett.*, 67(25):3483–3486, Dec 1991. 2.2, 2.2
- [15] S. C. Bell, M. Junker, M. Jasperse, L. D. Turner, Y.-J. Lin, I. B. Spielman, and R. E. Scholten. A slow atom source using a collimated effusive oven and a single-layer variable pitch coil zeeman slower. *Review of Scientific Instruments*, 81(1):013105, 2010. 2.2
- [16] V.L. Berezinskii. *Sov. Phys. JETP*, 32:493–500, 1970. 1.2
- [17] V.L. Berezinskii. *Sov. Phys. JETP*, 34:610–616, 1971. 1.2
- [18] T. Bergeman, Gidon Erez, and Harold J. Metcalf. Magnetostatic trapping fields for neutral atoms. *Phys. Rev. A*, 35(4):1535–1546, Feb 1987. 2.1, 2.4
- [19] J. Billy, V. Josse, Z. Zuo, A. Bernard, B. Hambrecht, P. Lugan, D. Clément, L. Sanchez-Palencia, P. Bouyer, and A. Aspect. Direct observation of Anderson localization of matter waves in a controlled disorder. *Nature*, 453(7197):891–894, 2008. 1.4
- [20] D. J. Bishop and J. D. Reppy. Study of the superfluid transition in two-dimensional ^4He films. *Phys. Rev. Lett.*, 40(26):1727–1730, Jun 1978. 1.2
- [21] D. J. Bishop and J. D. Reppy. Study of the superfluid transition in two-dimensional ^4He films. *Phys. Rev. B*, 22(11):5171–5185, Dec 1980. 1.2
- [22] R. N. Bisset, M. J. Davis, T. P. Simula, and P. B. Blakie. Quasicondensation and coherence in the quasi-two-dimensional trapped bose gas. *Phys. Rev. A*, 79(3):033626, Mar 2009. 1.3.3
- [23] Eric D. Black. An introduction to pound–drever–hall laser frequency stabilization. *American Journal of Physics*, 69(1):79–87, 2001. 3.3.1
- [24] G. Blatter, M. V. Feigel’man, V. B. Geshkenbein, A. I. Larkin, and V. M. Vinokur. Vortices in high-temperature superconductors. *Rev. Mod. Phys.*, 66(4):1125–1388, Oct 1994. 1.2, 1.2
- [25] Immanuel Bloch, Jean Dalibard, and Wilhelm Zwerger. Many-body physics with ultracold gases. *Reviews of Modern Physics*, 80(3):885, 2008. 1.1, 1.3, 1.3.3
- [26] S. N. Bose. *Z. Phys.*, 26:178, 1924. 1.2
- [27] C. C. Bradley, C. A. Sackett, and R. G. Hulet. Bose-Einstein condensation of lithium: Observation of limited condensate number. *Phys. Rev. Lett.*, 78(6):985–989, Feb 1997. 3.9
- [28] D. M. Brink and C. V. Sukumar. Majorana spin-flip transitions in a magnetic trap. *Phys. Rev. A*, 74(3):035401, Sep 2006. 2.4

- [29] R Bücke, A Perrin, S Manz, T Betz, Ch Koller, T Plisson, J Rottmann, T Schumm, and J Schmiedmayer. Single-particle-sensitive imaging of freely propagating ultracold atoms. *New Journal of Physics*, 11(10):103039, 2009. 3.9
- [30] S. Burger, F. S. Cataliotti, C. Fort, P. Maddaloni, F. Minardi, and M. Inguscio. Quasi-2D Bose-Einstein condensation in an optical lattice. *EPL (Europhysics Letters)*, 57(1):1, 2002. 1.3.4, 4.3
- [31] L V Butov. Condensation and pattern formation in cold exciton gases in coupled quantum wells. *Journal of Physics: Condensed Matter*, 16(50):R1577, 2004. 1.2
- [32] Y. Castin and R. Dum. Bose-Einstein condensates in time dependent traps. *Phys. Rev. Lett.*, 77(27):5315–5319, Dec 1996. 3.10.2, 5.1, 5.6
- [33] Min-Chul Cha, Matthew P. A. Fisher, S. M. Girvin, Mats Wallin, and A. Peter Young. Universal conductivity of two-dimensional films at the superconductor-insulator transition. *Phys. Rev. B*, 44(13):6883–6902, Oct 1991. 1.2
- [34] Min-Chul Cha and S. M. Girvin. Universal conductivity in the boson hubbard model in a magnetic field. *Phys. Rev. B*, 49(14):9794–9801, Apr 1994. 1.2
- [35] Yong P. Chen, J. Hitchcock, D. Dries, M. Junker, C. Welford, and R. G. Hulet. Phase coherence and superfluid-insulator transition in a disordered Bose-Einstein condensate. *Phys. Rev. A*, 77(3):033632, Mar 2008. 1.4, 4.2
- [36] Ananth P. Chikkatur. *Colliding and Moving Bose-Einstein Condensates: Studies of Superfluidity and Optical Tweezers for Condensate Transport*. PhD thesis, Massachusetts Institute of Technology, 2002. 3.10.2
- [37] M. L. Chiofalo, S. Succi, and M. P. Tosi. Ground state of trapped interacting Bose-Einstein condensates by an explicit imaginary-time algorithm. *Phys. Rev. E*, 62(5):7438–7444, Nov 2000. B
- [38] P. Cladé, C. Ryu, A. Ramanathan, K. Helmerson, and W. D. Phillips. Observation of a 2D bose gas: From thermal to quasicondensate to superfluid. *Physical Review Letters*, 102(17):170401, 2009. 1.3, 1.4, 1.3.4, 4.3
- [39] D. Clément, P. Bouyer, A. Aspect, and L. Sanchez-Palencia. Density modulations in an elongated Bose-Einstein condensate released from a disordered potential. *Phys. Rev. A*, 77(3):033631, Mar 2008. 1.4
- [40] D. Clément, A. F. Varón, M. Hugbart, J. A. Retter, P. Bouyer, L. Sanchez-Palencia, D. M. Gangardt, G. V. Shlyapnikov, and A. Aspect. Suppression of transport of an interacting elongated Bose-Einstein condensate in a random potential. *Phys. Rev. Lett.*, 95(17):170409, Oct 2005. 4.2

- [41] D. Clément, A. F. Varón, J. A. Retter, L. Sanchez-Palencia, A. Aspect, and P. Bouyer. Experimental study of the transport of coherent interacting matter-waves in a 1D random potential induced by laser speckle. *New Journal of Physics*, 8(8):165, 2006. 1.4, 4.2, 4.2, 4.2
- [42] Kristan L. Corwin, Zheng-Tian Lu, Carter F. Hand, Ryan J. Epstein, and Carl E. Wieman. Frequency-stabilized diode laser with the zeeman shift in an atomic vapor. *Appl. Opt.*, 37(15):3295–3298, 1998. 3.3.1
- [43] M. Crisan, D. Bodea, I. Grosu, and I. Tifrea. Metallic glass in two dimensional disordered bose systems; a renormalization group approach. *Journal of Superconductivity and Novel Magnetism*, 21:51–55, 2008. 10.1007/s10948-007-0296-6. 1.2
- [44] M. Cristiani, O. Morsch, J. H. Müller, D. Ciampini, and E. Arimondo. Experimental properties of Bose-Einstein condensates in one-dimensional optical lattices: Bloch oscillations, Landau-Zener tunneling, and mean-field effects. *Phys. Rev. A*, 65(6):063612, Jun 2002. 4.3
- [45] D. Boiron, C. Mennerat-Robilliard, J.-M. Fournier, L. Guidoni, C. Salomon, and G. Grynberg. Trapping and cooling cesium atoms in a speckle field. *Eur. Phys. J. D*, 7(3):373–377, 1999. 1.4, 4.2
- [46] Franco Dalfovo, Stefano Giorgini, Lev P. Pitaevskii, and Sandro Stringari. Theory of Bose-Einstein condensation in trapped gases. *Rev. Mod. Phys.*, 71(3):463–512, Apr 1999. 3.8, 3.10.2, B
- [47] Denis Dalidovich and Philip Phillips. Phase glass is a bose metal: A new conducting state in two dimensions. *Phys. Rev. Lett.*, 89(2):027001, Jun 2002. 1.2
- [48] D. Das and S. Doniach. Existence of a bose metal at $T = 0$. *Phys. Rev. B*, 60(2):1261–1275, Jul 1999. 1.2
- [49] C. J. Dedman, J. Nes, T. M. Hanna, R. G. Dall, K. G. H. Baldwin, and A. G. Truscott. Optimum design and construction of a zeeman slower for use with a magneto-optic trap. *Review of Scientific Instruments*, 75(12):5136–5142, 2004. 2.2
- [50] Wolfgang Demtröder. *Laser Spectroscopy: Vol. 1: Basic Principles*. Springer-Verlag Berlin Heidelberg, 2008. 3.3.1
- [51] Wolfgang Demtröder. *Laser Spectroscopy: Vol. 2: Experimental Techniques*. Springer-Verlag Berlin Heidelberg, 2008. 3.3.1
- [52] J Hecker Denschlag, J E Simsarian, H Häffner, C McKenzie, A Browaeys, D Cho, K Helmerson, S L Rolston, and W D Phillips. A Bose-Einstein condensate in an optical lattice. *Journal of Physics B: Atomic, Molecular and Optical Physics*, 35(14):3095, 2002. 4.3

- [53] D.S. Petrov, D.M. Gangardt, and G.V. Shlyapnikov. Low-dimensional trapped gases. *Journal de Physique IV (Proceedings)*, 116:5–44, oct 2004. 1.3.2
- [54] E. E. Edwards, M. Beeler, Tao Hong, and S. L. Rolston. Adiabaticity and localization in one-dimensional incommensurate lattices. *Phys. Rev. Lett.*, 101(26):260402, Dec 2008. 4.1, 4.1, B, B
- [55] Emily Edwards. *Construction of Apparatus and First Experiments Investigating Dynamics of Bose-Einstein Condensates in Disordered Optical Lattices*. PhD thesis, University of Maryland, 2009. 2.2, 3.1, 3.2.1, 3.2.1, 3.2.2, 3.3, 3.4, 3.9, 3.4, 3.5, 3.7, 4.1
- [56] A. Einstein. *Kgl. Preuss. Akad. Wiss*, 1924:261, 1924. 1.2
- [57] A. Einstein. *Kgl. Preuss. Akad. Wiss*, 1925:3, 1925. 1.2
- [58] L. Fallani, J. E. Lye, V. Guarrera, C. Fort, and M. Inguscio. Ultracold atoms in a disordered crystal of light: Towards a bose glass. *Phys. Rev. Lett.*, 98(13):130404, Mar 2007. 1.4
- [59] Leonardo Fallani, Chiara Fort, and Massimo Inguscio. Bose-Einstein condensates in disordered potentials. In E. Arimondo, editor, *Advances In Atomic, Molecular, and Optical Physics*, volume 56, pages 119 – 160. Academic Press, 2008. 1.4, 4.2
- [60] R.P. FEYNMAN. Simulating physics with computers. *International Journal of Theoretical Physics*, 21(6-7):467–488, 1982. 1.1
- [61] Daniel S. Fisher and P. C. Hohenberg. Dilute bose gas in two dimensions. *Phys. Rev. B*, 37(10):4936–4943, Apr 1988. 1.3.2
- [62] Matthew P. A. Fisher. Quantum phase transitions in disordered two-dimensional superconductors. *Phys. Rev. Lett.*, 65(7):923–926, Aug 1990. 1.2, 1.2
- [63] Matthew P. A. Fisher, G. Grinstein, and S. M. Girvin. Presence of quantum diffusion in two dimensions: Universal resistance at the superconductor-insulator transition. *Phys. Rev. Lett.*, 64(5):587–590, Jan 1990. 1.2
- [64] Matthew P. A. Fisher, Peter B. Weichman, G. Grinstein, and Daniel S. Fisher. Boson localization and the superfluid-insulator transition. *Phys. Rev. B*, 40(1):546–570, Jul 1989. 1.4
- [65] Christopher J. Foot. *Atomic Physics (Oxford Master Series in Atomic, Optical and Laser Physics)*. Oxford University Press, USA, first edition, 2005. 3.9
- [66] Fabrice Gerbier and Yvan Castin. Heating rates for an atom in a far-detuned optical lattice. *Phys. Rev. A*, 82(1):013615, Jul 2010. 4.3

- [67] J. I. Gillen, W. S. Bakr, A. Peng, P. Unterwaditzer, S. Fölling, and M. Greiner. Two-dimensional quantum gas in a hybrid surface trap. *Phys. Rev. A*, 80(2):021602, Aug 2009. 4.3
- [68] S M Girvin, M Wallin, E S Sørensen, and A P Young. Universal conductivity of dirty bosons in two dimensions. *Physica Scripta*, 1992(T42):96, 1992. 1.2
- [69] Allen M. Goldman and Nina Markovic. Superconductor-insulator transitions in the two-dimensional limit. *Physics Today*, 51(11):39–44, 1998. 1.2, 1.2
- [70] Joseph W. Goodman. *Speckle Phenomena in Optics (Theory and Applications)*. Roberts and Company Publishers, first edition, 2006. 4.2, 4.2
- [71] A. Görlitz, J. M. Vogels, A. E. Leanhardt, C. Raman, T. L. Gustavson, J. R. Abo-Shaeer, A. P. Chikkatur, S. Gupta, S. Inouye, T. Rosenband, and W. Ketterle. Realization of Bose-Einstein condensates in lower dimensions. *Phys. Rev. Lett.*, 87(13):130402, Sep 2001. 1.3.4, 4.3
- [72] Rudolf Grimm, Matthias Weidemüller, and Yurii B. Ovchinnikov. Optical dipole traps for neutral atoms. *Advances in Atomic, Molecular, and Optical Physics*, 42:95, 2000. 2.1, 2.6, 2.6, 3.8
- [73] T. L. Gustavson, A. P. Chikkatur, A. E. Leanhardt, A. Görlitz, S. Gupta, D. E. Pritchard, and W. Ketterle. Transport of Bose-Einstein condensates with optical tweezers. *Phys. Rev. Lett.*, 88(2):020401, Dec 2001. 2.1, 2.6
- [74] Albrecht Haase, Donatella Cassettari, Björn Hessmo, and Jörg Schmiedmayer. Trapping neutral atoms with a wire. *Phys. Rev. A*, 64(4):043405, Sep 2001. 2.3, 3.4, 3.6
- [75] Z. Hadzibabic and J. Dalibard. Two-dimensional Bose fluids: An atomic physics perspective. *ArXiv e-prints*, (0912.1490), December 2009. 1.2, 1.3.1, 1.3.3, 1.3.3, 1.3.3
- [76] Z Hadzibabic, P Kruger, M Cheneau, B Battelier, and J Dalibard. Berezinskii-Kosterlitz-Thouless crossover in a trapped atomic gas. *Nature*, 441(7097):1118–1121, JUN 28 2006. 1.3.4, 4.3, 5.1, 5.1.2, 5.1.2
- [77] Z Hadzibabic, P Krüger, M Cheneau, S P Rath, and J Dalibard. The trapped two-dimensional Bose gas: from Bose-Einstein condensation to Berezinskii-Kosterlitz-Thouless physics. *New Journal of Physics*, 10(4):045006, 2008. 1.3.3, 1.3.4
- [78] Zoran Hadzibabic, Sabine Stock, Baptiste Battelier, Vincent Bretin, and Jean Dalibard. Interference of an array of independent Bose-Einstein condensates. *Phys. Rev. Lett.*, 93(18):180403, Oct 2004. 1.3.4, 4.3, 4.3

- [79] Lene Vestergaard Hau, J. A. Golovchenko, and Michael M. Burns. A new atomic beam source: The “candlestick”. *Review of Scientific Instruments*, 65(12):3746–3750, 1994. 3.2.2
- [80] A. F. Hebard and M. A. Paalanen. Magnetic-field-tuned superconductor-insulator transition in two-dimensional films. *Phys. Rev. Lett.*, 65(7):927–930, Aug 1990. 1.2
- [81] Eugene Hecht. *Optics*. Addison-Wesley, fourth edition, 2002. 3.8
- [82] Harald F. Hess. Evaporative cooling of magnetically trapped and compressed spin-polarized hydrogen. *Phys. Rev. B*, 34(5):3476–3479, Sep 1986. 2.5
- [83] P. C. Hohenberg. Existence of long-range order in one and two dimensions. *Phys. Rev.*, 158(2):383–386, Jun 1967. 1.2
- [84] Markus Holzmann, Gordon Baym, Jean-Paul Blaizot, and Franck Laloë. Superfluid transition of homogeneous and trapped two-dimensional Bose gases. *Proceedings of the National Academy of Sciences*, 104(5):1476–1481, 2007. 1.3.3
- [85] Markus Holzmann and Werner Krauth. Kosterlitz-thouless transition of the quasi-two-dimensional trapped bose gas. *Phys. Rev. Lett.*, 100(19):190402, May 2008. 1.3.3, 1.3.3
- [86] Holzmann, Markus, Chevallier, Maguelonne, and Krauth, Werner. Semiclassical theory of the quasi-two-dimensional trapped bose gas. *EPL*, 82(3):30001, 2008. 1.3.3
- [87] C.-L. Hung, X. Zhang, N. Gemelke, and C. Chin. Observation of scale invariance and universality in two-dimensional bose gases. *ArXiv e-prints*, (1009.0016), aug 2010. 1.3.4, 4.3
- [88] H. M. Jaeger, D. B. Haviland, B. G. Orr, and A. M. Goldman. Onset of superconductivity in ultrathin granular metal films. *Phys. Rev. B*, 40(1):182–196, Jul 1989. 1.2
- [89] D. S. Jin, M. R. Matthews, J. R. Ensher, C. E. Wieman, and E. A. Cornell. Temperature-dependent damping and frequency shifts in collective excitations of a dilute Bose-Einstein condensate. *Phys. Rev. Lett.*, 78(5):764–767, Feb 1997. 3.8
- [90] Yu. Kagan, E. L. Surkov, and G. V. Shlyapnikov. Evolution of a bose-condensed gas under variations of the confining potential. *Phys. Rev. A*, 54(3):R1753–R1756, Sep 1996. 1.3.3
- [91] J. Kasprzak, M. Richard, S. Kundermann, A. Baas, P. Jeambrun, J. M. J. Keeling, F. M. Marchetti, M. H. Szymanska, R. Andre, J. L. Staehli, V. Savona, P. B. Littlewood, B. Deveaud, and Le Si Dang. Bose-Einstein

- condensation of exciton polaritons. *NATURE*, 443(7110):409–414, SEP 28 2006. 1.2
- [92] Wolfgang Ketterle and N.J. Van Druten. Evaporative cooling of trapped atoms. volume 37 of *Advances In Atomic, Molecular, and Optical Physics*, pages 181 – 236. Academic Press, 1996. 2.1, 2.5
- [93] M. Khl, H. Moritz, T. Stferle, C. Schori, and T. Esslinger. Superfluid to mott insulator transition in one, two, and three dimensions. *Journal of Low Temperature Physics*, 138:635–644, 2005. 10.1007/s10909-005-2273-4. 4.3
- [94] J M Kosterlitz. The critical properties of the two-dimensional xy model. *Journal of Physics C: Solid State Physics*, 7(6):1046–1060, 1974. 1.2
- [95] J M Kosterlitz and D J Thouless. Ordering, metastability and phase transitions in two-dimensional systems. *Journal of Physics C: Solid State Physics*, 6(7):1181–1203, 1973. 1.2
- [96] Peter Krüger, Zoran Hadzibabic, and Jean Dalibard. Critical point of an interacting two-dimensional atomic bose gas. *Physical Review Letters*, 99(4):040402, 2007. 1.3.3, 1.3.4
- [97] K. I. Lee, J. A. Kim, H. R. Noh, and W. Jhe. Single-beam atom trap in a pyramidal and conical hollow mirror. *Opt. Lett.*, 21(15):1177–1179, 1996. 3.4
- [98] Y. Liu and A.M. Goldman. Superconductor-insulator transitions in two dimensions. *Mod. Phys. Lett. B*, 8(5):277–300, 1994. 1.2
- [99] D. R. Luhman and R. B. Hallock. Kosterlitz-Thouless transition for ^4He films adsorbed to rough surfaces. *Phys. Rev. Lett.*, 93(8):086106, Aug 2004. 1.5
- [100] D. R. Luhman and R. B. Hallock. Third sound on CaF_2 films of varying roughness. *Phys. Rev. B*, 74(1):014510, Jul 2006. 1.5
- [101] J. E. Lye, L. Fallani, M. Modugno, D. S. Wiersma, C. Fort, and M. Inguscio. Bose-Einstein condensate in a random potential. *Phys. Rev. Lett.*, 95(7):070401, Aug 2005. 1.4, 4.2
- [102] Z-Y Ma, A M Thomas, C J Foot, and S L Cornish. The evaporative cooling of a gas of caesium atoms in the hydrodynamic regime. *Journal of Physics B: Atomic, Molecular and Optical Physics*, 36(16):3533, 2003. 2.5
- [103] K. B. MacAdam, A. Steinbach, and C. Wieman. A narrow-band tunable diode laser system with grating feedback, and a saturated absorption spectrometer for cs and rb. *American Journal of Physics*, 60(12):1098–1111, 1992. 3.3.1
- [104] L. P. Maguire, S. Szilagyi, and R. E. Scholten. High performance laser shutter using a hard disk drive voice-coil actuator. *Review of Scientific Instruments*, 75(9):3077–3079, 2004. 3.8

- [105] Edmund R. Malinowski. *Factor Analysis in Chemistry*. Wiley, third edition, 2002. 3.9
- [106] D. McKay, M. White, M. Pasienski, and B. DeMarco. Phase-slip-induced dissipation in an atomic Bose-Hubbard system. *Nature*, 453(7191):76–79, 2008. 1.4
- [107] N. D. Mermin. Crystalline order in two dimensions. *Phys. Rev.*, 176(1):250–254, Dec 1968. 1.2
- [108] N. D. Mermin and H. Wagner. Absence of ferromagnetism or antiferromagnetism in one- or two-dimensional isotropic heisenberg models. *Phys. Rev. Lett.*, 17(22):1133–1136, Nov 1966. 1.2
- [109] Harold J. Metcalf and Peter van der Straten. *Laser Cooling and Trapping*. Springer-Verlag New York, Inc., 1999. 2.2, 2.3, 2.4
- [110] Petter Minnhagen. The two-dimensional coulomb gas, vortex unbinding, and superfluid-superconducting films. *Rev. Mod. Phys.*, 59(4):1001–1066, Oct 1987. 1.2
- [111] Oliver Morsch and Markus Oberthaler. Dynamics of Bose-Einstein condensates in optical lattices. *Rev. Mod. Phys.*, 78(1):179–215, Feb 2006. 4.3
- [112] K. M. O’Hara, M. E. Gehm, S. R. Granade, and J. E. Thomas. Scaling laws for evaporative cooling in time-dependent optical traps. *Phys. Rev. A*, 64(5):051403, Oct 2001. 2.6
- [113] C. Orzel, A. K. Tuchman, M. L. Fenselau, M. Yasuda, and M. A. Kasevich. Squeezed states in a Bose-Einstein condensate. *Science*, 291(5512):2386–2389, 2001. 4.3
- [114] Yu. B. Ovchinnikov, J. H. Müller, M. R. Doery, E. J. D. Vredenbregt, K. Helmerson, S. L. Rolston, and W. D. Phillips. Diffraction of a released Bose-Einstein condensate by a pulsed standing light wave. *Phys. Rev. Lett.*, 83(2):284–287, Jul 1999. 4.3
- [115] R. E. Peierls. *Ann. Inst. Henri Poincare*, 5:177, 1935. 1.2
- [116] C.J. Pethick and H. Smith, editors. *Bose-Einstein Condensation in Dilute Gases*. Cambridge University Press, 2008. 1.3.3, 2.1, 5.1, B
- [117] D. S. Petrov, M. Holzmann, and G. V. Shlyapnikov. Bose-Einstein condensation in quasi-2D trapped gases. *Phys. Rev. Lett.*, 84(12):2551–2555, Mar 2000. 1.3.2
- [118] D. S. Petrov and G. V. Shlyapnikov. Interatomic collisions in a tightly confined bose gas. *Phys. Rev. A*, 64(1):012706, Jun 2001. 1.3.2

- [119] Philip Phillips and Denis Dalidovich. The Elusive Bose Metal. *Science*, 302(5643):243–247, 2003. 1.2, 1.2, 1.2, 1.3
- [120] William D. Phillips and Harold Metcalf. Laser deceleration of an atomic beam. *Phys. Rev. Lett.*, 48(9):596–599, Mar 1982. 2.2
- [121] Anatoli Polkovnikov, Ehud Altman, and Eugene Demler. Interference between independent fluctuating condensates. *Proceedings of the National Academy of Sciences*, 103(16):6125–6129, 2006. 5.1
- [122] Anna Posazhennikova. [bold colloquium]: Weakly interacting, dilute bose gases in 2d. *Reviews of Modern Physics*, 78(4):1111, 2006. 1.3.3
- [123] Nikolay Prokof’ev, Oliver Ruebenacker, and Boris Svistunov. Critical point of a weakly interacting two-dimensional bose gas. *Phys. Rev. Lett.*, 87(27):270402, Dec 2001. 1.3.2, 1.3.2
- [124] Nikolay Prokof’ev and Boris Svistunov. Two-dimensional weakly interacting bose gas in the fluctuation region. *Phys. Rev. A*, 66(4):043608, Oct 2002. 1.3.2
- [125] E. L. Raab, M. Prentiss, Alex Cable, Steven Chu, and D. E. Pritchard. Trapping of neutral sodium atoms with radiation pressure. *Phys. Rev. Lett.*, 59(23):2631–2634, Dec 1987. 2.3
- [126] Steffen P. Rath, Tarik Yefsah, Kenneth J. Günter, Marc Cheneau, Rémi Desbuquois, Markus Holzmann, Werner Krauth, and Jean Dalibard. Equilibrium state of a trapped two-dimensional bose gas. *Phys. Rev. A*, 82(1):013609, Jul 2010. 1.3.4
- [127] Steffen Patrick Rath and Wilhelm Zwerger. Full counting statistics of the interference contrast from independent Bose-Einstein condensates. *Phys. Rev. A*, 82(5):053622, Nov 2010. 5.1
- [128] J. Reichel, W. Hänsel, and T. W. Hänsch. Atomic micromanipulation with magnetic surface traps. *Phys. Rev. Lett.*, 83(17):3398–3401, Oct 1999. 3.4
- [129] Giacomo Roati, Chiara D’Errico, Leonardo Fallani, Marco Fattori, Chiara Fort, Matteo Zaccanti, Giovanni Modugno, Michele Modugno, and Massimo Inguscio. Anderson localization of a non-interacting Bose-Einstein condensate. *Nature*, 453(7197):895–U36, JUN 12 2008. 1.4
- [130] M. Robert-de Saint-Vincent, J.-P. Brantut, B. Allard, T. Plisson, L. Pezzé, L. Sanchez-Palencia, A. Aspect, T. Bourdel, and P. Bouyer. Anisotropic 2d diffusive expansion of ultracold atoms in a disordered potential. *Phys. Rev. Lett.*, 104(22):220602, Jun 2010. 1.5
- [131] Baruch Rosenstein and Dingping Li. Ginzburg-Landau theory of type II superconductors in magnetic field. *Rev. Mod. Phys.*, 82(1):109–168, Jan 2010. 1.2

- [132] D. Rychtarik, B. Engeser, H.-C. Nägerl, and R. Grimm. Two-dimensional Bose-Einstein condensate in an optical surface trap. *Phys. Rev. Lett.*, 92(17):173003, Apr 2004. 4.3
- [133] A. I. Safonov, S. A. Vasilyev, I. S. Yasnikov, I. I. Lukashevich, and S. Jaakkola. Observation of quasicondensate in two-dimensional atomic hydrogen. *Phys. Rev. Lett.*, 81(21):4545–4548, Nov 1998. 1.2
- [134] T. A. Savard, K. M. O’Hara, and J. E. Thomas. Laser-noise-induced heating in far-off resonance optical traps. *Phys. Rev. A*, 56(2):R1095–R1098, Aug 1997. 3.8
- [135] S. Schneider, A. Kasper, Ch. vom Hagen, M. Bartenstein, B. Engeser, T. Schumm, I. Bar-Joseph, R. Folman, L. Feenstra, and J. Schmiedmayer. Bose-Einstein condensation in a simple microtrap. *Phys. Rev. A*, 67(2):023612, Feb 2003. 2.3, 3.4, 3.6
- [136] R. E. Scholten. Enhanced laser shutter using a hard disk drive rotary voice-coil actuator. *Review of Scientific Instruments*, 78(2):026101, 2007. 3.8
- [137] Stephen R. Segal, Quentin Diot, Eric A. Cornell, Alex A. Zozulya, and Dana Z. Anderson. Revealing buried information: Statistical processing techniques for ultracold-gas image analysis. *Phys. Rev. A*, 81(5):053601, May 2010. 3.9, 3.10.2
- [138] T. P. Simula, M. D. Lee, and D. A. W. Hutchinson. Transition from the Bose-Einstein condensate to the Berezinskii-Kosterlitz-Thouless phase. *Philos. Mag. Lett.*, 85:395, 2005. 1.3
- [139] David Snoke. Spontaneous Bose Coherence of Excitons and Polaritons. *Science*, 298(5597):1368–1372, 2002. 1.2
- [140] Erik S. Sørensen, Mats Wallin, S. M. Girvin, and A. Peter Young. Universal conductivity of dirty bosons at the superconductor-insulator transition. *Phys. Rev. Lett.*, 69(5):828–831, Aug 1992. 1.2
- [141] I. B. Spielman, W. D. Phillips, and J. V. Porto. Mott-insulator transition in a two-dimensional atomic bose gas. *Phys. Rev. Lett.*, 98(8):080404, Feb 2007. 4.3
- [142] Danial Adam Steck. Rubidium 87 d line data. Available online at <http://steck.us/alkalidata/>. 3.3.1
- [143] Sabine Stock. *Quantized Vortices in a Bose-Einstein Condensate: Thermal Activation and Dynamic Nucleation*. PhD thesis, University of Paris, 2006. 1.4, 1.3.4, 4.3

- [144] Sabine Stock, Zoran Hadzibabic, Baptiste Battelier, Marc Cheneau, and Jean Dalibard. Observation of phase defects in quasi-two-dimensional Bose-Einstein condensates. *Phys. Rev. Lett.*, 95(19):190403, Nov 2005. 1.3.4, 4.3
- [145] C. V. Sukumar and D. M. Brink. Spin-flip transitions in a magnetic trap. *Phys. Rev. A*, 56(3):2451–2454, Sep 1997. 2.4
- [146] Lincoln Turner. *Holographic Imaging of Cold Atoms*. PhD thesis, The University of Melbourne, 2004. 3.9, 3.10.2
- [147] Lincoln D. Turner, Karl P. Weber, David Paganin, and Robert E. Scholten. Off-resonant defocus-contrast imaging of cold atoms. *Opt. Lett.*, 29(3):232–234, 2004. 3.9, 3.10.2
- [148] M. R. Walkiewicz, P. J. Fox, and R. E. Scholten. Candlestick rubidium beam source. *Review of Scientific Instruments*, 71(9):3342–3344, 2000. 3.2.2
- [149] Mats Wallin, Erik S. Sørensen, S. M. Girvin, and A. P. Young. Superconductor-insulator transition in two-dimensional dirty boson systems. *Phys. Rev. B*, 49(17):12115–12139, May 1994. 1.2, 1.1, 1.2
- [150] David S. Weiss, Erling Riis, Yaakov Shevy, P. Jeffrey Ungar, and Steven Chu. Optical molasses and multilevel atoms: experiment. *J. Opt. Soc. Am. B*, 6(11):2072–2083, 1989. 3.10.2
- [151] M. White, M. Pasienski, D. McKay, S. Q. Zhou, D. Ceperley, and B. DeMarco. Strongly interacting bosons in a disordered optical lattice. *Phys. Rev. Lett.*, 102(5):055301, Feb 2009. 1.4, 4.2
- [152] Matthew White. *Ultracold Atoms in a Disordered Optical Lattice*. PhD thesis, University of Illinois at Urbana-Champaign, 2009. 4.2, 4.2, 4.2
- [153] S. Wildermuth, P. Krüger, C. Becker, M. Brajdic, S. Haupt, A. Kasper, R. Folman, and J. Schmiedmayer. Optimized magneto-optical trap for experiments with ultracold atoms near surfaces. *Phys. Rev. A*, 69(3):030901, Mar 2004. 2.3, 3.4, 3.6
- [154] A. Witte, Th. Kisters, F. Riehle, and J. Helmcke. Laser cooling and deflection of a calcium atomic beam. *J. Opt. Soc. Am. B*, 9(7):1030–1037, 1992. 2.2
- [155] Jiansheng Wu and Philip Phillips. Vortex glass is a metal: Unified theory of the magnetic-field and disorder-tuned bose metals. *Phys. Rev. B*, 73(21):214507, Jun 2006. 1.2, 1.2